FLOW VISUALIZATION OF SILICA NANOFLUID INJECTION FOR ENHANCED OIL RECOVERY IN A MICROMODEL BASED ON WELL-SORTED GRAIN-SIZE POROUS MEDIA

Felipe Adrião Cruz

Dissertação de Mestrado apresentada ao Programa de Pós-graduação em Engenharia da Nanotecnologia, COPPE, da Universidade Federal do Rio de Janeiro, como parte dos requisitos necessários à obtenção do título de Mestre em Engenharia da Nanotecnologia.

Orientador(es): Tiago Albertini Balbino
Carolina Palma Naveira Cotta

Rio de Janeiro
Julho de 2019

FLOW VISUALIZATION OF SILICA NANOFLUID INJECTION FOR ENHANCED OIL RECOVERY IN A MICROMODEL BASED ON WELL-SORTED GRAIN-SIZE POROUS MEDIA

Felipe Adrião Cruz

DISSERTAÇÃO SUBMETIDA AO CORPO DOCENTE DO INSTITUTO ALBERTO LUIZ COIMBRA DE PÓS-GRADUAÇÃO E PESQUISA DE ENGENHARIA (COPPE) DA UNIVERSIDADE FEDERAL DO RIO DE JANEIRO COMO PARTE DOS REQUISITOS NECESSÁRIOS PARA A OBTENÇÃO DO GRAU DE MESTRE EM CIÊNCIAS EM ENGENHARIA DA NANOTECNOLOGIA.

Examinada por:

_____

Prof. Tiago Albertini Balbino, D.Sc.

_____

Profª. Carolina Palma Naveira Cotta, D.Sc.

_____

Prof. Santiago Gabriel Drexler, D.Sc.

_____

Prof. João Victor Nicolini, D.Sc.

RIO DE JANEIRO, RJ - BRASIL
JULHO DE 2019

Cruz, Felipe Adrião

Flow visualization of silica nanofluid injection for Enhanced Oil Recovery in a micromodel based on well-sorted grain-size porous media/ Felipe Adrião Cruz. – Rio de Janeiro: UFRJ/COPPE, 2019.

XX, 132 p.: il.; 29,7 cm.

Orientador: Tiago Albertini Balbino

Carolina Palma Naveira Cotta

Dissertação (mestrado) – UFRJ/ COPPE/ Programa de Engenharia da Nanotecnologia, 2019.

Referências Bibliográficas: p. 94-107.

1. Recuperação Avançada de Petróleo. 2. Micromodelos. 3. Nanofluidos. 4. Microfluídica. I. Balbino, Tiago Albertini *et al*. II. Universidade Federal do Rio de Janeiro, COPPE, Programa de Engenharia da Nanotecnologia. III. Título.

ACKNOWLEDGEMENT

I would first like to thank my two advisors, D.Sc. Tiago Balbino and D.Sc. Carolina Cotta, from PENt/COPPE/UFRJ. Their guidance and constant seek for quality steered me in the right direction to elaborate a work which I believe is worth of proud.

Secondly, I would like to thank the members of the jury committee, D.Sc. Santiago Drexler and D.Sc. João Nicolini, for their participation in the dissertation presentation and for their collaboration to raise valuable questions regarding this work.

Then, I would like to express my very profound gratitude to the M.Sc. candidate Nathália Dias and D.Sc. candidate Raquel Fedrizzi, as the two key persons that assisted in the development of this work. Your help in several steps along the way allowed it to be completed within a very limited term. Moreover, the supports of the M.Sc. candidates Thiago Saraiva and Ingrid Curcino must also be remarked.

A special thank to the Ph.D candidate Enno de Vries, advised by Ph.D Amir Raoof from the Department of Earth Sciences in the University of Utrecht, the Netherlands. Your collaboration regarding the pore-network algorithm was essential to generate new pore-networks towards the application here desired.

I would also like to thank all my research colleagues that somehow helped to elaborate this work, by assisting in experiments or raising critical commentaries. In this context, the members of LabMEMS: Jordana, Douglas, Gabriel and Mylena; the members of LRAP: Thais, Marcelo, Alex and Leandro; D.Sc. Helen Ferraz from GRIFIT; Vanessa from LIAP; Marcelo from DOPOLAB; Nilton from LTTC; Agatha from FLUMAT; Luana from NIDF; and my friends from PetroBowl and PENt.

Finally, I must express my gratitude to my parents, brother and aunt for providing me unfailing support during my whole life. In fact, an eternal acknowledge has to be made to the person that continuously encouraged me throughout all my years of study: my mother Claudia. This accomplishment is for you.

Resumo da Dissertação apresentada à COPPE/UFRJ como parte dos requisitos necessários para a obtenção do grau de Mestre em Ciências (M.Sc.)

VISUALIZAÇÃO DO ESCOAMENTO DE NANOFLUIDOS DE SÍLICA PARA RECUPERAÇÃO AVANÇADA DE PETRÓLEO EM MICROMODELO BASEADO EM MEIOS POROSOS COM TAMANHOS DE GRÃO BEM-SELECIONADOS

Felipe Adrião Cruz

Julho/2019

Orientadores: Tiago Albertini Balbino
Carolina Palma Naveira Cotta

Programa: Engenharia da Nanotecnologia

Atualmente, testes de *coreflood* são considerados a base do método científico para melhor compreender o fluxo de fluidos em meios porosos. Entretanto, estes testes podem apresentar elevado tempo experimental e dificuldade na visualização do escoamento. Neste contexto, a microfluídica vem surgindo como uma tendência complementar na engenharia de reservatórios, oferecendo soluções rápidas para problemas tradicionais. Os dispositivos microfluídicos, ou micromodelos, podem fornecer a visualização direta dos mais diversos fenômenos na escala de poro, e também serem utilizados para realizar testes seqüenciais de recuperação avançada de petróleo (EOR). Neste trabalho, micromodelos de polidimetilsiloxano (PDMS) foram fabricados e aplicados em uma técnica de nano-EOR com nanofluidos de sílica. Diversas malhas porosas foram geradas computacionalmente com base em parâmetros estatísticos de rochas reais. Foi montado um aparato experimental para a visualização do escoamento e realizado um método de injeção de fluidos similar a aplicações em campo. A partir da captura e processamento de imagens, calcularam-se os fatores de recuperação de óleo (FR) ao longo dos testes. Por fim, a injeção de nanofluidos de sílica apresentou FRs adicionais em 12% na recuperação terciária e 23% na recuperação secundária.

Abstract of Dissertation presented to COPPE/UFRJ as a partial fulfillment of the requirements for the degree of Master of Science (M.Sc.)

FLOW VISUALIZATION OF SILICA NANOFLUID INJECTION FOR ENHANCED OIL RECOVERY IN A MICROMODEL BASED ON WELL-SORTED GRAIN-SIZE POROUS MEDIA

Felipe Adrião Cruz

July/2019

Advisors: Tiago Albertini Balbino
Carolina Palma Naveira Cotta

Graduate Program: Nanotechnology Engineering

Currently, coreflood analysis is considered as the conventional laboratory test to understand fluid flow through porous media. However, this technique possesses disadvantages regarding time-consuming experiments and fluid movement visualization. In this context, microfluidics is emerging as a trend in reservoir engineering, providing fast-paced solutions for old-fashioned problems. Microfluidic chips, or micromodels, are able to directly observe a wide range of transport phenomena in pore-scale and assist in fluid screening for enhanced oil recovery (EOR). In this study, polydimethylsiloxane (PDMS) micromodels were fabricated and applied in a nano-EOR technique with silica nanofluids. Several pore-networks were computationally generated based on statistical parameters of real rocks. An experimental setup was mounted to provide a platform for flow visualization and a fluid injection method was applied similarly to field applications. By digital processing of captured images, oil recovery factors (RF) were calculated during the experiments. Finally, silica nanofluid injection showed additional RFs of 12% as tertiary recovery and 23% as secondary recovery.

CONTENTS

LIST OF FIGURES

LIST OF TABLES

LIST OF ACRONYMS

ANP	Brazilian National Petroleum Agency
API	American Petroleum Institute
BT	Breakthrough
CA	Contact angle
CAD	Computer-aided drawing
CCD	Charged coupled device
CFD	Computational fluid dynamics
CMC	Critical micellar concentration
CNC	Computer numerical control
CSS	Cyclic steam stimulation
CT	Computed tomography
DLS	Dynamic light scattering
DLVO	Derjaguin, Landau, Verwey, Overbeek theory
DSA	Drop shape analyzer
EDL	Electrical double layer
EOR	Enhanced oil recovery
HPHT	High pressure, high temperature
IEP	Isoelectric point
IFT	Interfacial tension
IOR	Improved oil recovery
LSW	Low-salinity water
MEOR	Microbial enhanced oil recovery
NF	Nanofluid
NP	Nanoparticles
O&G	Oil and gas
PALS	Phase analysis light scattering
PDI	Polydispersity index
PDMS	Polydimethylsiloxane
pH	Hydrogen ion potential
PIV	Particle image velocimetry
PMMA	Polymethylmethacrylate
PNM	Pore network model

PV	Pore volume
PVI	Photoluminescent volumetric imaging
PVP	Polyvinylpyrrolidone
PVS	Polyvinylsiloxane
REM	Replica molding
RF	Recovery factor
ROC	Reservoir-on-a-chip
SAGD	Steam-assisted gravity drainage
SEM	Scanning electron microscope
SSW	Synthetic seawater
SW	Seawater
UV	Ultraviolet

LIST OF SYMBOLS

Kr	Relative permeability [-]
M	Mobility ratio [-]
Pc	Capillary pressure [MLT^{-2}]
P	Pressure [MLT^{-2}]
S	Saturation [-]

Greek Letters

γ	Interfacial tension [MT^{-2}]
μ	Dynamic viscosity [$ML^{-1}T^{-1}$]
σ	Standard deviation [-]
ϕ	Logarithm transformation of grain diameter [L]

1 INTRODUCTION

After the first commercial oil discovery in 1859 in Pennsylvania, United States, an entirely new industry that would shape the future of the global capitalism emerged [1]. Business associations arose, led by the formation of the first corporate trust in history by Standard Oil, the largest company in the world by that time. In the first half of the 20th century, the relationship between oil reserves and strategies of nations would tighten, with oil playing an important role in the occurrence of the two World Wars. Later that century, a sequence of six postwar oil crises dramatically changed the oil prices and then the global market, especially due to the 1973 Arab Oil Embargo and the 1979 Iranian Revolution. For those historical facts, Yergin [1] marked the twentieth century as the "hydrocarbon age". Fig. 1.1 shows shares percentages of global primary energy consumption by fuel, from 1965 to 2017 [2]. In this period, oil remained as the world´s dominant fuel source, making up just over a third of all energy consumed in 2017. Coal has been in the 2nd place all over this period, with a recent market share fall to 27.6%. Natural gas, which was initially considered a by-product of the oil industry, accounted a new record of 23% of global primary energy consumption. A recent increase of hydroelectricity and renewables share percentages has also been seen. Despite O&G importance in the world´s energy consumption, the fraction of those hydrocarbon sources that cannot be produced by current techniques is still large. This holds true especially in the exploration of more challenging reserves. In the case of ultra-deepwater Brazilian pre-salt basins, the oil recovery factor is around 21% [3]. According to its National Oil Agency (ANP), an increase of 1% in this oil recovery would represent additional US$11 billion in royalty payments, leading to new investments of around US$16 billion.

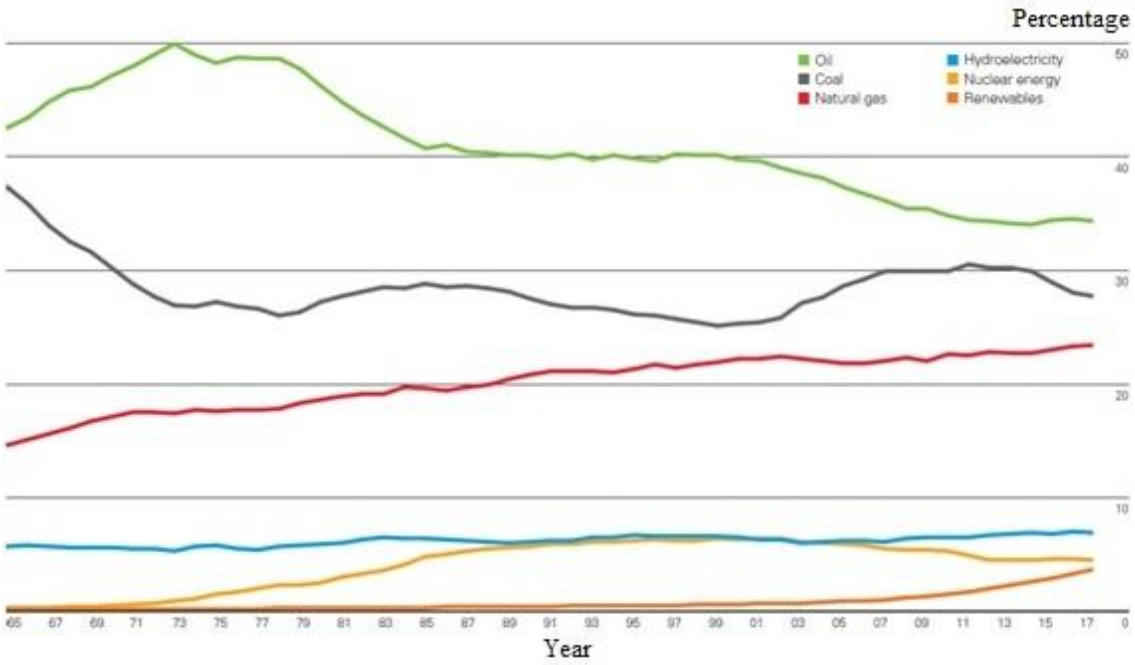

Fig. 1.1 – Shares percentages of global primary energy consumption by fuel, from 1965 to 2017. Oil remains the world´s dominant fuel, making up just over a third of all energy consumed [2].

For the crude oil and its desired fractions to be commercialized, they must be produced and treated on an offshore or onshore facility and then refined in a refiner unit. The production phase requires the drilling of a few-to-several wells and their further completion to enable an upward migration of fluids from a subsurface porous rock to the surface. The first stage of production, or primary recovery, is the one in which the natural forces of the reservoir, such as the existence of an upper gas-cap or the proximity to a water aquifer, displace hydrocarbons [4]. During primary recovery, only a small percentage of the initial hydrocarbons in place are produced, typically around 10% for oil reservoirs. In secondary recovery, an external fluid, such as water or gas, is injected into the reservoir through injection wells. The successive use of primary recovery and secondary recovery in an oil reservoir produces about 15% to 40% of the original oil in place. When the production rates associated with secondary recovery are not economical, sophisticated techniques that alter the original properties of the oil/rock system need to be implemented. This combination of techniques is called tertiary recovery or enhanced oil recovery (EOR), since they can actually be initiated at any time during the productive life of an oil reservoir. Table 1.1 shows the three classical major classes of EOR operations: thermal recovery, chemical flooding, and gas injection [5]. It also presents some specific methods related to each class and their associated EOR mechanisms. As more recent techniques, engineered nanoparticles can

also be injected to improve several properties related to oil displacement, being considered an innovative class with application methods and related EOR mechanisms still in discussion [6].

Table 1.1 – The three major classes of EOR technologies. Specific methods related to each class are being briefly detailed, with their associated EOR mechanisms [5].

EOR classes	Detailed methods	Major EOR mechanisms
Thermal methods	CSS	Viscosity reduction
	Steam flooding	IFT reduction
	In-situ combustion	Steam distillation
	SAGD	Oil expansion
Chemical methods	Alkaline flooding	IFT reduction
	Surfactant flooding Smart water flooding	Wettability alteration
	Polymer flooding	Mobility control
	ASP flooding	Emulsification
Gas methods	Hydrocarbon gas injection	Pressure maintenance
	CO_2 injection	Viscosity reduction
	N_2 injection	Oil expansion
	Air injection	Miscibility

Before applying in a field-scale, the effectiveness of an EOR technique must be evaluated in laboratory, in which the main test to address this matter is coreflood [7]. In this test (Fig. 1.2), one or more fluids are injected into a 1in to 2in rock-sample extracted from the desired formation to be analyzed [8]. Corefloods are used to measure relative permeabilities, changing of fluid-saturations, formation damages and other rock-fluid interactions [9]. As an example of a nano-EOR assay, Hendraningrat *et al.* [10] performed laboratory coreflood in a Berea sandstone plug saturated with North Sea crude oil. Despite obtaining several petrophysical information and being more realistic, coreflood experiments possesses some disadvantages. The acquisition of real-rock samples and fluids may require high operational costs. This can be solved by using analogous outcropped plugs and laboratory-model oils. Another drawback is the time-dependence of the test, which may last from one to several months due to sample aging and very low-velocity flow in porous media. At last, corefloods do not allow a direct visualization of fluid movement, which is of primal importance to understand inumerous transport and deposition phenomena in oil reservoirs. For that reason, some coreflood rigs are coupled with X-ray scanning or micro-CT, but the use of additional imaging devices involves more cost in the research projects. Moreover, most of these

additional devices have constraints regarding high-resolution imaging, thus not being able to observe flow in pore-scale and limiting its usage to fluid-saturation changes.

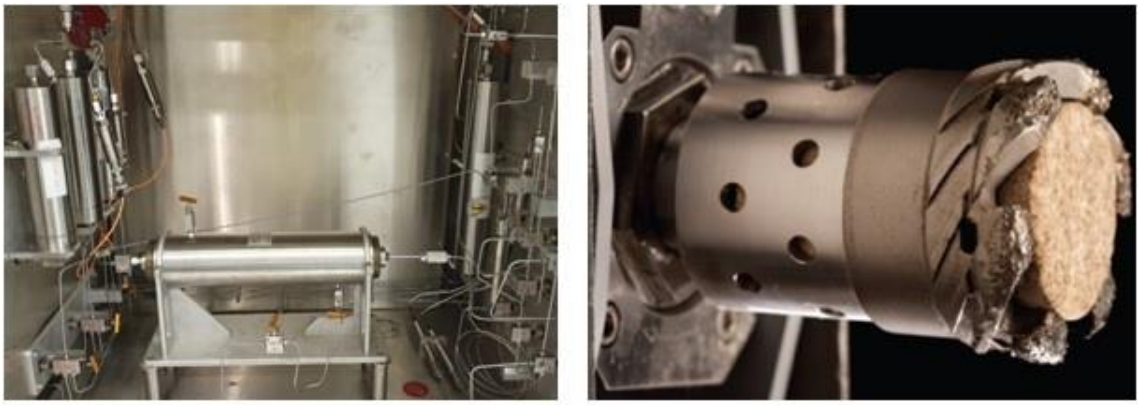

Fig. 1.2 – (a) laboratory coreflood rig designed by PETROC Technologies. The image shows a core holder in the center and piston cells in the lateral walls. It is intended to be operated with core samples up to 30cm longer and 1in to 2in diameter, in testing conditions as high as 10.000 psia and 150°C [8]. (b) a rotary coring bit with a core extracted from a borehole wall. Core samples are generally costly to be taken, however they can provide several petrophysical information when analyzed in corefloods [9].

To overcome conventional coreflood assays, microfluidic platforms can be used to investigate oil displacement and the mechanisms behind fluid injection with the oil/rock system [11]. Microfluidics is a scientific discipline that studies the movement, control and manipulation of fluids and particles in nano-to-macro scales. As the pore connections in reservoir-rocks are generally in the order of few angstrom (10^{-10} m) to several micrometers (10^{-6} m), microfluidic chips can be designed and fabricated to represent geometries in real-porous media. By using transparent 'reservoir-on-a-chip' devices, the O&G industry has a complementary solution to capture images and directly visualize the interaction between fluids and hydrocarbons (Fig. 1.3) [12]. Another advantage is that the low-cost micromodels enable fluid screening tests to be performed with much less price of more complex corefloods. Some authors stated that microfluidics is helping to validate traditional imaging technology, since it is difficult to image microdarcy or nanodarcy flow with even specialized X-rays or micro-CT. In fact, several different EOR researches in micromodels have been conducted in the recent years. As another O&G application, Doryani *et al.* [13] analyzed asphaltene precipitation and deposition in a uniformly patterned glass micromodel for flow

assurance studies. Finally, microfluidic chips are also applicable to validate digital rock petrophysical models, broadening the use of this technology in the O&G industry [14].

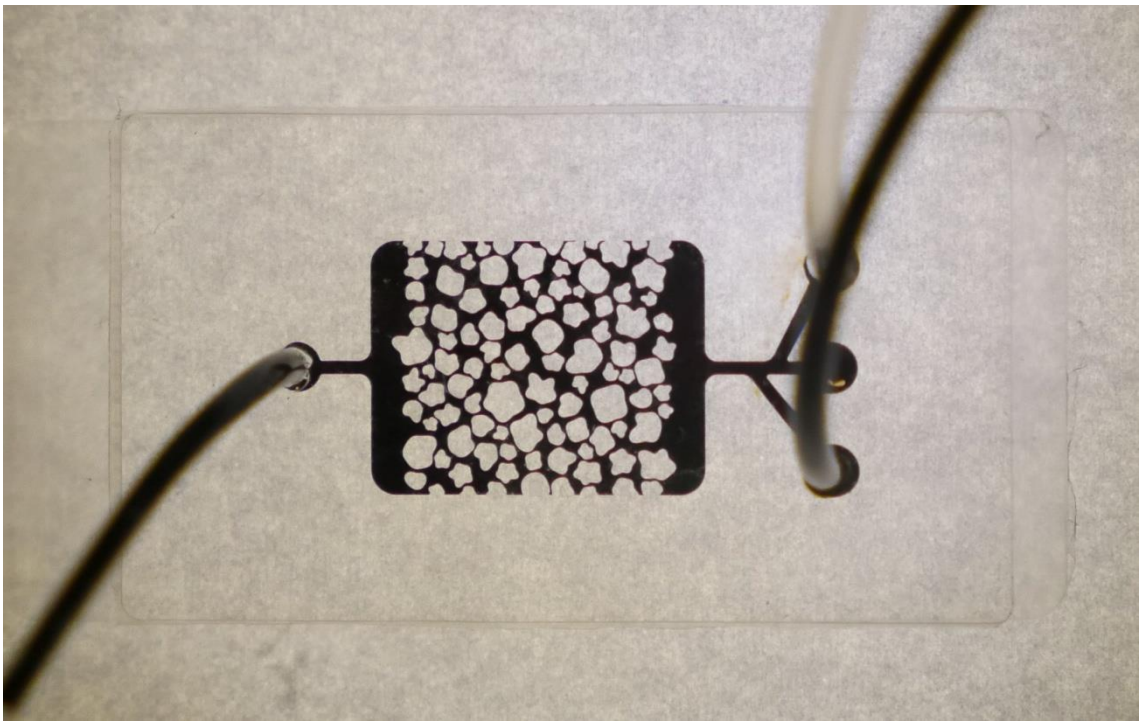

Fig. 1.3 – Overview of a PDMS transparent micromodel fully saturated with oil and connections to be used in an EOR experiment.

In this study, polydimethylsiloxane (PDMS) micromodels were designed and applied to evaluate the effectiveness of a nano-EOR technique with silica nanofluid injection. To obtain more representative porous media, the pore-networks were computationally generated based on statistical parameters of real rocks. At last, microfluidic visualization was used to observe fluid displacement in pore-scale, being an alternative approach to measure the recovery factors in general EOR applications.

1.1 Objectives

The main objective of this work is to develop a methodology to fabricate bidimensional PDMS micromodels and confirm their application in a laboratory nano-EOR technique. The results were be obtained by capturing and processing images of oil displacement in microfluidic experiments and further discussed by conducting interface and surface fluids/micromodel measurements.

In order to achieve the main objective, the following series of specific objectives were outlined:

- Generation of computational porous geometries based on field values of real-rock grain distribution statistical parameters to better represent a porous media.
- Fabrication of PDMS microfluidic chips containing the generated pore-network via micromilling and soft lithography processes on an acrylic mold followed by the application of a polymeric polydimethylsiloxane (PDMS) solution.
- Perform nano-EOR techniques with silica (SiO_2) nanofluid injection in the fabricated micromodels. Evaluate the effectiveness of SiO_2 nanoparticles for EOR by measuring recovery factors (RF) during oil displacement and conducting interfacial measurements between nanofluids, oil and micromodel.

2 Literature review

This chapter will introduce and discuss the concepts necessary to understand the methodology developed in this work. Here, it will be presented the ideas of micromodels and nanofluids, focusing their applications in EOR and discussing some results reported by research studies conducted in these areas.

2.1 Micromodels

A micromodel is an idealized, generally two-dimensional representation of a porous medium, *i.e.* a network of interconnected pores along with a solid matrix. Since most micromodels are fabricated with horizontal dimensions in millimeters and constant height of micrometers, their associated fluid flow is considered to be 2D or even 2½D depending on the height of the micromodel. Some micromodels are also conceived as 3D, however additional visualization challenges arise when observing flow through a greater depth. Regarding their composition, most of the micromodels are fabricated in transparent materials, such as glass, quartz or polymers, to allow the visual observation of fluid flow. Since capillary effects are essential for two-phase flow studies, a small pore size in the pore network (<1 mm) is required. Nowadays, the reservoir-on-a-chip (ROC) concept is designing more realistic micromodels by core sample imaging, therefore being a new paradigm in reservoir engineering (Fig. 2.1) [15]. On the other hand, the earliest micromodels had simple and regular geometric features. According to its history, the very first micromodel was conceived by Alfred Chatenever and John C. Calhoun in 1952 at the University of Oklahoma [16]. It consisted basically of a single layer of glass beads sandwiched by two flat transparent plates. Despite its simplicity, this earliest micromodel was the forerunner of a series of future two-phase flow studies with microfluidic devices for O&G applications. Another example of an early micromodel is the Hele-Shaw cell, in which is basically a glass-bead micromodel with any material placed between the two parallel transparent plates. Chuoke *et al.* [17] conducted one of the first two-phase flow experiments in a Hele-Shaw micromodel to investigate the occurrence of macroscopic instabilities in displacement of one viscous fluid by another immiscible fluid. Despite being easy to make, both glass-bead and Hele-Shaw micromodels possesses limited optical visualization due to the three-dimensional nature of these micromodels.

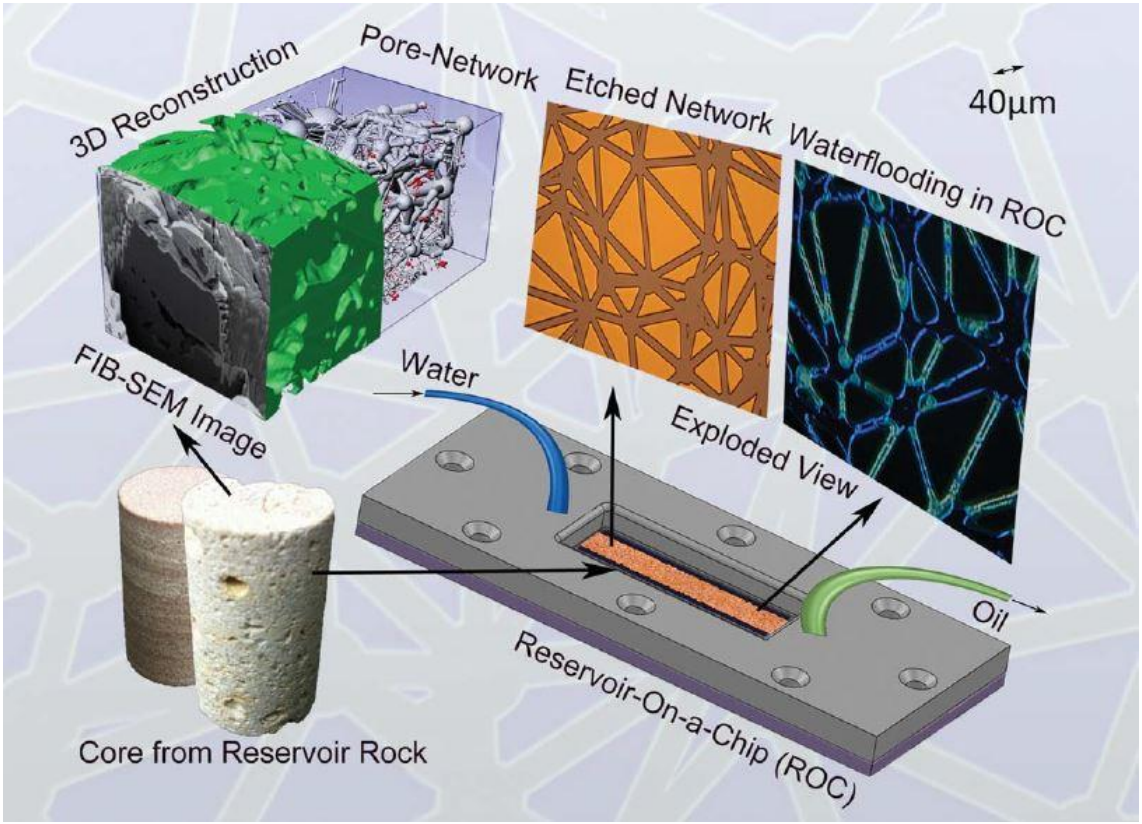

Fig. 2.1 – Reservoir-on-a-chip (ROC) novel miniaturization approach to conceive micromodels, enabling pore-scale assessment of fluids interactions relevant to reservoir engineering [15].

Several methods can be used to fabricate micromodels depending on the material of the devices. Karadimitriou and Hassanizadeh [18] provided an extensive literature review about these fabrication methods. The very first micromodel [16] required the combination of materials, in their case glass beads. A disadvantage of combined models is the inability to precisely control pore network parameters, such as pore size distribution, number and geometry of pores. One technique that overcomes this limitation is optical lithography, also called photo-lithography. Being developed and improved during the last few decades, photo-lithography is used to create models accurately in a wide range of pore networks. On the other hand, this method requires a clean room to manufacture, and involves medium to high costs in its implementation. Another widely used micromodel fabrication is the etching method, which subdivides into two other available methods: chemical or wet etching, and laser or plasma etching. In chemical or wet etching, acids are used to etch the glass or silicon surface. The first etched micromodel was conceived through chemical etching in 1961 by Mattax and Kyte [19]. They used their micromodel to perform waterflood experiments under various wettability conditions. Fig. 2.2 shows two of their visual results for strongly

water-wet and slightly water-wet micromodels, respectively. The glass micromodel wettability was altered from strongly water-wet to slightly water-wet by first saturating it with brine and then flushing to connate water with a selected crude oil, which was aged in the model for several hours. Examination of contact angle in individual areas showed this wettability behavior alteration.

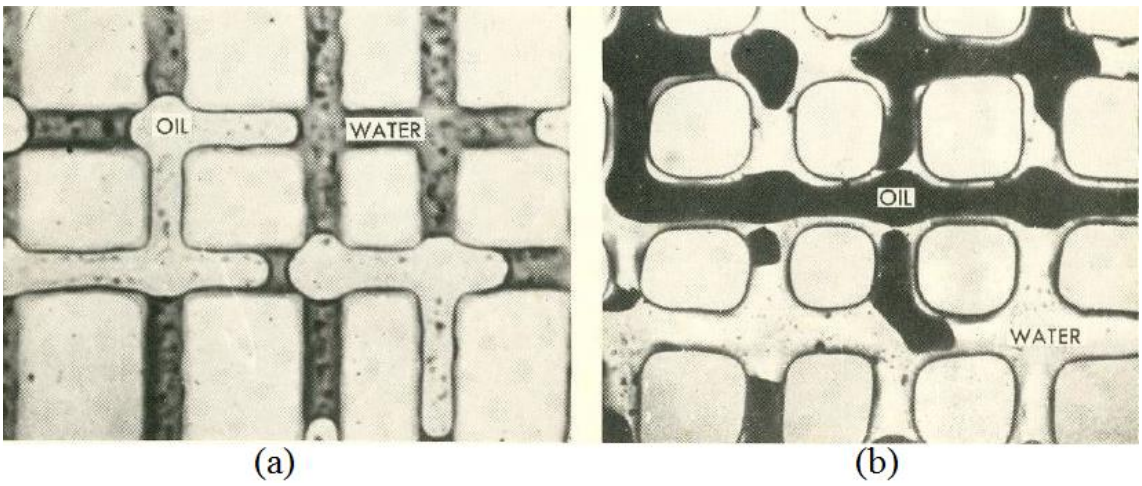

Fig. 2.2 – Visual results of waterflood experiments in etched micromodels performed by Mattax and Kyte (1961). (a) residual oil in a strongly water-wet micromodel.(b) fluid distribution in a slightly water-wet micromodel [19].

At last, a method to create very small, simple geometric structures on the micro- and nano-meter scales is soft lithography. It is called “soft” because it employs the use of elastomeric materials, such as polymers. One of the most widely used materials in soft lithography is polydimethylsiloxane (PDMS). PDMS is a liquid that, after contact with a curing agent and subjected to controlled heating or prolonged time, polymerizes. It is suitable for academic studies since it is easy to manipulate, inexpensive, and effective for microfluidics applications [20]. Despite these advantages, PDMS has some limiting issues. It may react and absorb fluids, resulting in a deformation of the flow network. Moreover, its surface characteristics are very different from real-rocks and may also change over time. This effect is due to the plasma technique used to bond the two PDMS slabs of the model. Therefore, PDMS micromodels are mostly applicable when observations of fluid/fluid interactions are desired instead of surface/fluid interactions. Regarding fabrication, several different variations of soft lithography with PDMS may be performed. An effective procedure is the use of a replica molding (REM), which can be manufactured by different means of microfabrication techniques [21]. The idea of fabricating a master mold to rapidly replicate micromodel structures is

interesting because it enables parallel use of these models in multiple flow experiments. Wilson *et al.* [22] presented a fabrication approach that combined mechanical micromilling to design REM and a two-step soft lithography micromolding to fabricate microfluidic channels with fully circular cross-sections. Fig. 2.3 shows a schematic outline of their experimental fabrication process. In their process, a mechanical micromachining technique, known as micromilling, uses miniature cutting tools with ball nose micro-end mills to enable semicircular cross-section channels in the master mold. After that, a two-step lithography process with positive PVS molding and negative PDMS molding is used to create circular channel microfluidic devices. In fact, most of the processes that combine mechanical micromilling and soft lithography employ a one-step positive PDMS molding directly onto the fabricated REM [23]. Moreover, the ability to precisely control the fabrication via a computer numerical control (CNC) machine offers a viable and industrially relevant alternative to create master molds in multiple scale sizes.

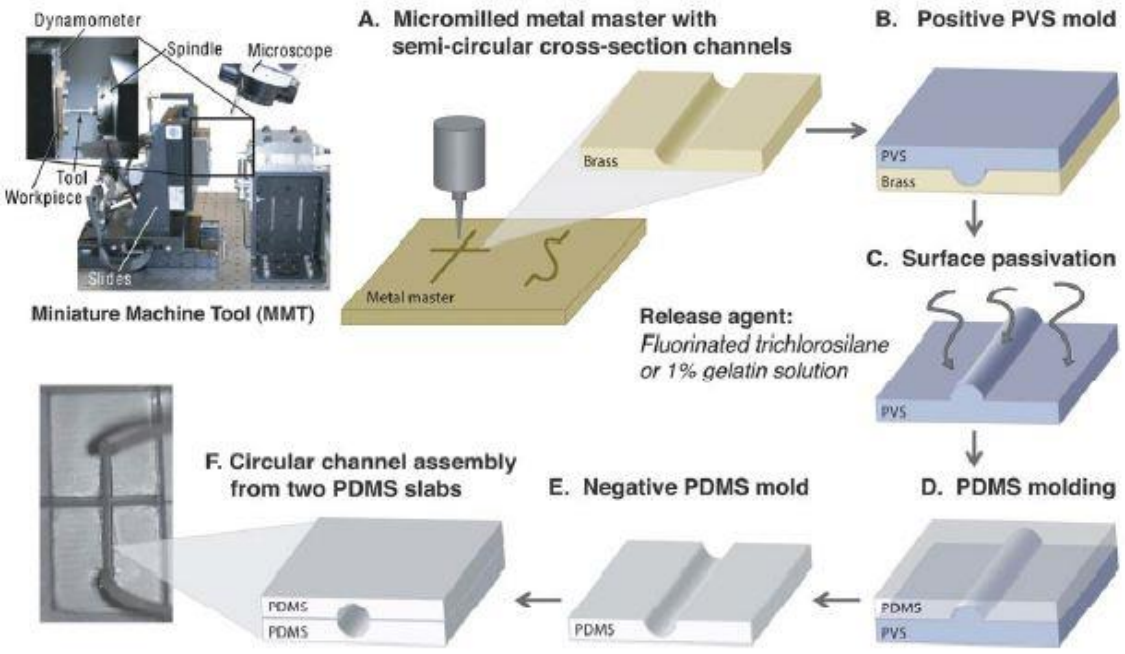

Fig. 2.3 – Schematic outline of the experimental process to fabricate circular cross-section microfluidic channels. The procedure combined the use of micromilling on a metal master mold and two-step soft lithography with polyvinylsiloxane (PVS) and PDMS [22].

The manufacturing of micromodels can be done by each of the previous procedures presented in this chapter. However, some additional challenges arise when modeling real porous media. One of the most important is related to the surface properties of rocks. In this context, the main characteristic to evaluate the interactions

between rocks and fluids is the wettability. Wettability is the preference of a solid to contact one liquid or gas, known as the wetting phase, rather than another [24]. Reservoir rocks typically are described as being water-wet, oil-wet, or intermediate-wet. This wetting tendency depends on a series of factors, especially the mineralogy of the rock surfaces and the composition and properties of the crude oil and connate brine [25]. Also, there may exist some microscopic wettability variations in rocks, represented by dalmatian wetting and mixed wetting conditions [26]. Regarding reservoir rocks types, approximately 59% of the world´s giant fields are sandstones, which are composed mainly by the mineral quartz (SiO_2) [27]. Due to material composition similarity, glass micromodels are generally used to simulate sandstone reservoirs. Moreover, glass micromodels have very well-defined wetting properties and can withstand pressures up to few hundred kilopascals. However, the fabrication of glass micromodels cannot be performed in regular laboratories, since it generally employs the manipulation of acids by chemical etching. At last, the other 40% of world's oil reserves are found in carbonate reservoirs, which are composed primarily of carbonate minerals. In this context, Song *et al*. [28] fabricated a micromodel by chemical etching directly on a calcite crystal ($CaCO_3$) in order to model a real carbonate-rock microfluidic system.

2.1.1 Micromodels for EOR

Micromodels have been extensively used in the past few decades for EOR laboratory applications. One of the earliest reviews regarding the use of micromodels for EOR was presented by Buckley (1990) [29]. After that, as the newest EOR techniques were emerging, several research studies have been conducted with micromodels [30,31,40–49,32,50–59,33,60–66,34–39]. As one example of a classical EOR micromodel application, Dong *et al*. [57] used a glass micromodel to investigate oil displacement by alkaline flooding as a chemical EOR technique (Table 1.1). The ability to directly observe in pore-scale made possible to determine the principal mechanisms governing this EOR process. One was partial wettability alteration; the other was the formation of in situ oil-in-water (O/W) emulsion. In their experiment, heavy oil was emulsified in brine by the use of an alkaline and a very dilute surfactant formula. Fig. 2.4 shows the images related to the alkaline flooding process. First, heavy oil was injected until reach irreducible water saturation (Fig 2.4(a)). Then, a pore-level imaging was captured (Fig 2.4(b)), showing the formation of water films surrounding

the water-wet glass boundaries, with the continuous oil phase remaining in the central areas of the pore network. Fig. 2.4(c) shows the oil and irreducible water saturations after alkaline slug injection. In this alkaline injection, the injected water phase penetrated through the continuous oil phase and formed some water ganglia inside the channels, as shown by pore-level imaging in Fig. 2.4(d). The presence of these discontinuous water ganglia formed water-in-oil (W/O) emulsions with reduced viscosity when compared to heavy oil, thus enhancing oil displacement and recovery.

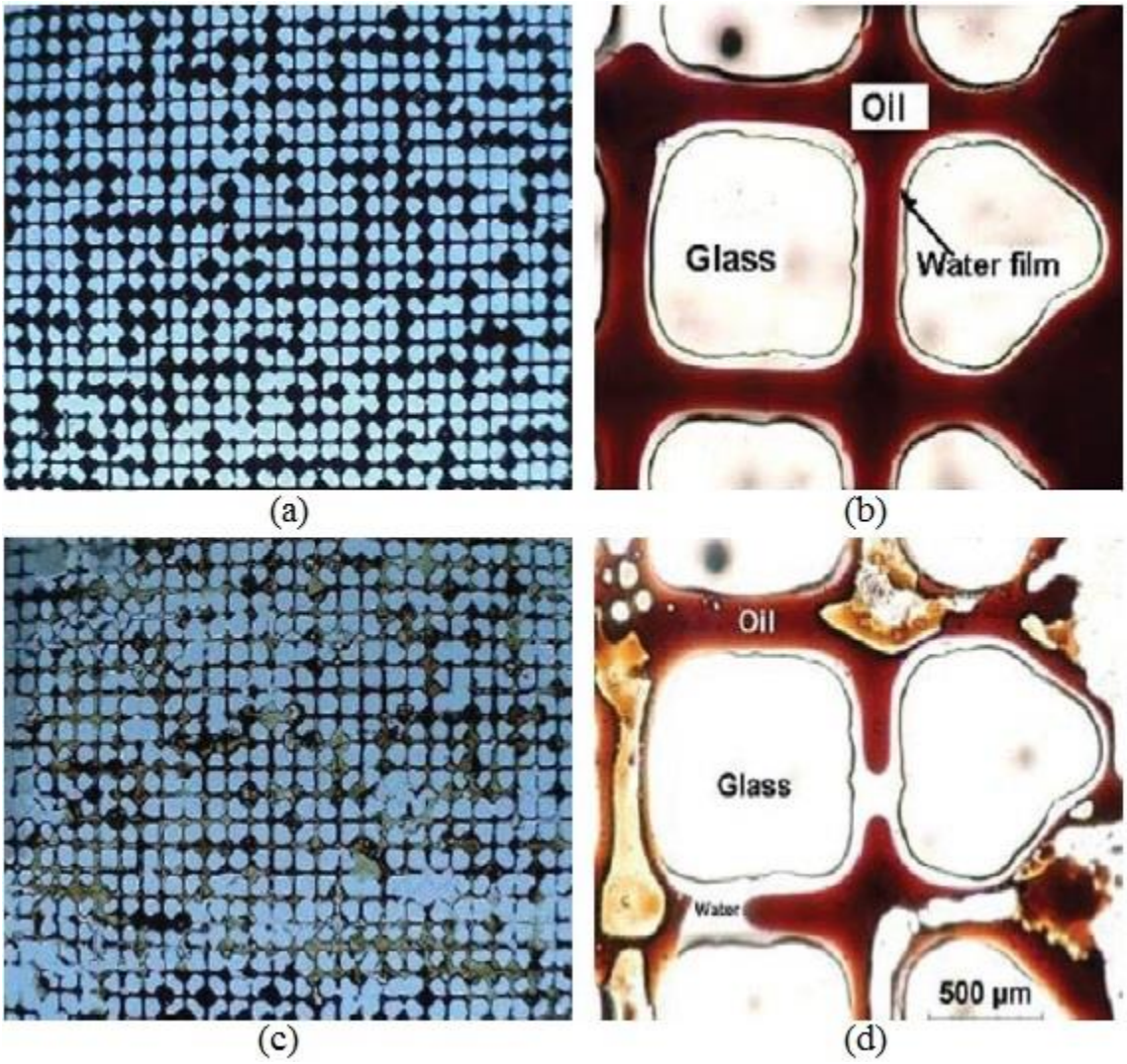

Fig. 2.4 – Micromodel images of an alkaline flooding process. (a) irreducible water saturation after heavy oil injection. (b) pore-level imaging showing the formation of water films surrounding the glass boundaries of the micromodel, therefore indicating a water-wet condition. (c) oil displacement after alkaline slug injection. (d) pore-level imaging after alkaline flooding, showing the formation of water-in-oil (W/O) emulsions that reduced the viscosity of heavy oil, thus enhancing its displacement and recovery [57].

As a nano-EOR application, Nguyen *et al.* [47] evaluated the stability and effectiveness of CO_2 foam stabilized by silica nanoparticles in EOR at the pore and micromodel scales. The stabilization of CO2 foam by nanoparticles is a classical approach known as Pickering emulsion. It is reported that nanoparticle foams are significantly more stable than surfactant foam due to the high adsorption energy of nanoparticles in the gas-liquid interfaces. Regarding their stability results, conventional surfactant foams showed a progressively increase in bubble diameter with time, while nanoparticle-stabilized foams continued to be stable after 10 days. They have also evaluated the pore dynamics in the micromodel for CO_2 gas flood and nanoparticle-stabilized CO_2 foam flood (Fig. 2.5). Fluorescent imaging was obtained by employing the natural fluorescence of the oil phase, excited at 450-500 nm and collected at 510-560 nm. Fig. 2.5(a) shows the formation of viscous fingering of CO_2 gas flooding, by the preferential path in which CO_2 gas flowed. In contrast, nanoparticle-stabilized CO_2 foams remained stable in the micromodel, trapping and transporting interstitial oil (Fig 2.5(b)). Moreover, the injection of nanoparticle-stabilized CO_2 foams provided an additional 15% of oil recovery for a medium heavy oil (API gravity of 24º) when compared to conventional CO_2 gas flooding.

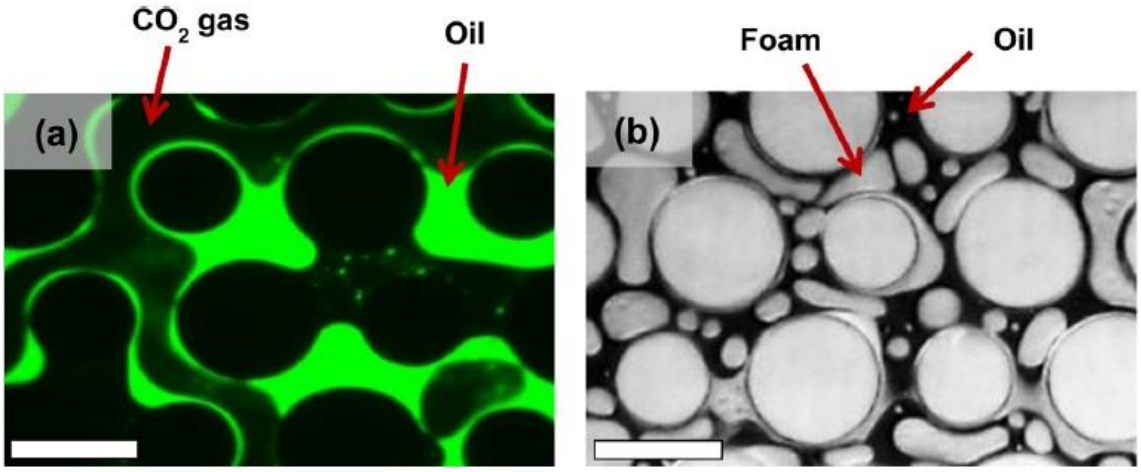

Fig. 2.5 – Pore-scale images of CO_2 gas flooding and SiO_2 nanoparticle-stabilized CO_2 foam flooding. (a) fluorescent imaging at the microscale for CO_2 gas flooding. It shows the connected sinuous nature of the oil phase, with the CO_2 gas (black) flowing through a preferential path through the network resulting in fingering. (b) brightfield imaging in microscale for nanoparticle-stabilized CO_2 foam. It shows the formation of stable nanoparticle-stabilized CO_2 bubbles through the network, trapping and transporting interstitial oil. Scale bars = 250 μm [47].

Microbial enhanced oil recovery (MEOR) is receiving a recent attention in the oil industry due to the undamaging action of microorganisms to the reservoir and fluids

and reasonable additional oil recovery. Several studies have been performed to evaluate the injection of microorganisms in micromodels. Nourani *et al*. [52] performed a MEOR technique in a glass micromodel containing a fractured network system. The injection of bacteria contributes to the oil displacement by reducing interfacial tension and changing the wettability of the rock towards a more water-wet condition. In their work, five species of bacteria from a crude oil originating from a Persian reservoir were injected in two series of visualizations experiments: static and dynamic. By imaging processing methodology, the behavior of bacterial microorganisms towards a favorable oil displacement was demonstrated. Another application of MEOR in micromodels was provided by Amani [59]. In this study, a homogeneous glass micromodel was used for investigation of oil recovery by rhamnolipid injection. A rhamnolipid mixture was produced by *P. aeruginosa* bacteria strain which can grow on sunflower as a sole carbon source. Interfacial tension (IFT) tests showed that the rhamnolipid mixture was able to reduce IFT of water to 26mN/m to 2mN/m. According to the study, produced rhamnolipid was also reported as an effective biosurfactant in a wide range of temperatures, pHs and salt concentrations. Micromodel visualization showed an additional 5% of oil recovery by rhamnolipid injection when compared to waterflood, thus being considered appropriate as a MEOR technique.

The oil industry has recently focused their attention to the injection of low-salinity water (LSW) as an EOR method. Several studies have been performed to evaluate fluid distribution and the micromechanism of displacement throughout LSW injection [58,63,67,68]. Despite experimental results showed that LSW is effective to change the wettability of the rock to displace trapped oil, the controlling mechanisms behind this method are not well understood. Thus, pore-scale imaging of the low-salinity effect in contact with crude oil is strongly required. In this context, Amirian *et al.* [62] provided an extensively study to investigate the dynamics of oil displacement by LSW in clean and clay-coated glass micromodels. The pore-networks were obtained from thin sections of real porous rock representing heterogeneous media. The resulting image was printed into a transparent film which was used in a photo-lithography process. For the clay coating procedure, a slurry made of clay particles in a high salinity water brine (30 000 ppm NaCl) was prepared and injected into the micromodel at a very high rate (20m/day) for several pore volumes. Then, the micromodel was left in an oven for 72 hours to evaporate water and enable dried clay to adhere irreversible to the pore walls. Regarding flow experiments, they have analyzed both water-wet and oil-wet

wettability status in clean and clay-coated micromodels. In water-wet systems, both in the presence and absence of clays, LSW hindered the removal of trapped oil, due to the development of a viscoelastic water-oil interface. In contrast, a wettability alteration towards more water-wet condition was observed for oil-wet systems coated with clay. Fig. 2.6 shows pore-scale images of both high-salinity water flooding (Fig. 2.6(a)) and low-salinity water flooding (Fig. 2.6(b)). It can be seen a significant oil recovery when the ion concentration of injected water is decreased. The authors explained the effect of LSW in clay-coated oil-wet system in terms of the expansion of the electric double layer (EDL) formed between the clay particle and injected water.

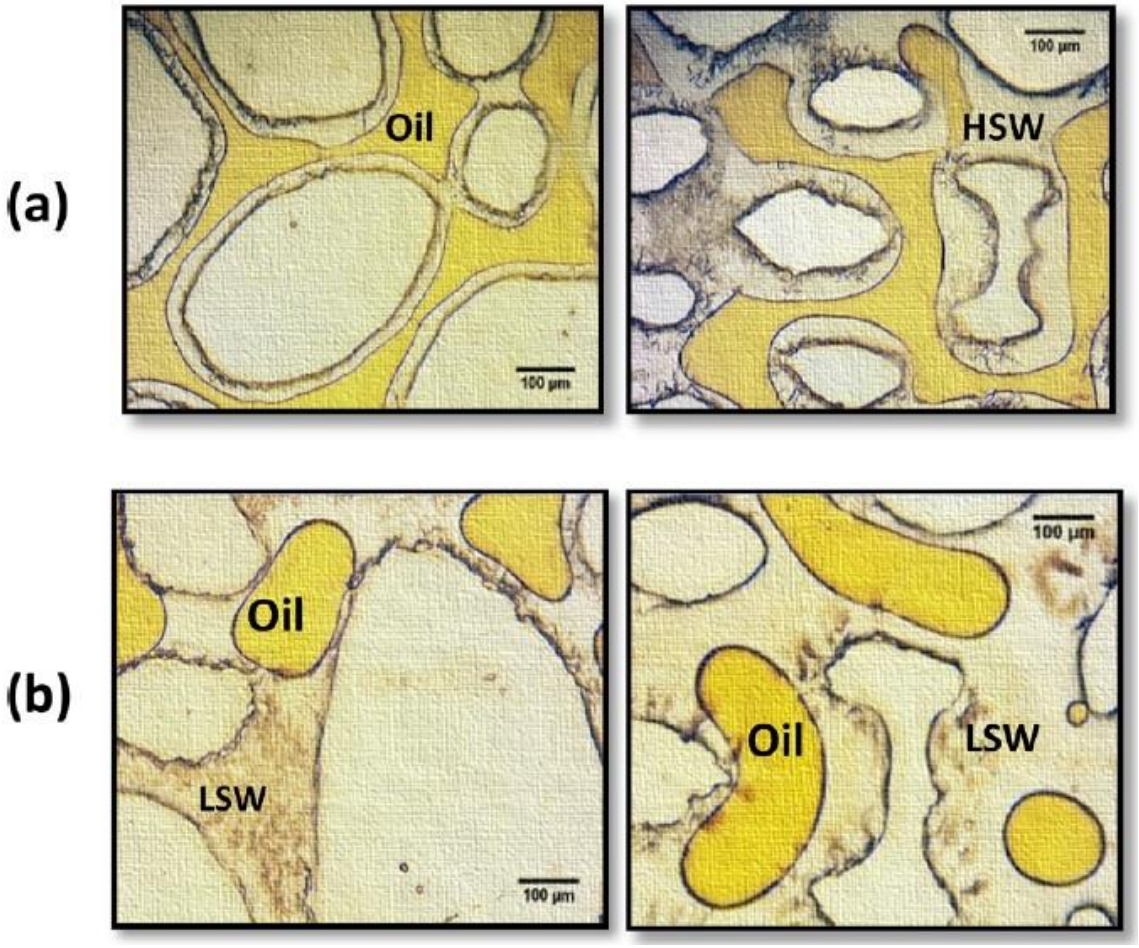

Fig. 2.6 – Microscopic images after the model was flushed with (a) high-salinity water and (b) low-salinity water. It can be seen a significant oil recovery when the ion concentration of injected water is decreased. The authors explained this low-salinity effect by the expansion of the electric double layer (EDL) formed between the clay particles and injected water [62].

The investigation of EOR mechanisms by pore-scale imaging is not restricted to two-dimensional micromodels. Recently, an EOR research has been conducted in a three-dimensional micromodel by injecting flexible microcapsules suspensions [39]. By

using confocal microscopy to observe different phenomena in pore-scale, the dynamics of oil ganglia and fluid saturations were determined. The study reported that injection of flexible microcapsules were effective as mobility control agents, therefore modifying fluid distributions throughout the pore-network and reducing residual oil saturation. Moreover, an innovative 3D-micromodel patent has also been configured by researchers from Saudi Arabian Oil Company to create a three-dimensional fabricator [69]. In this patent, an image processing module acquires an image of a rock sample. Then, a transformation module transforms the image into a binary matrix and determines a set of statistical properties. Then, a layer generation module generates different stochastic layers by varying the statistical properties. Finally, an arrangement module combines these generated layers into a 3D-micromodel to be fabricated by 3D printing. In fact, this 3D-micromodel patent is been considered effective to model real reservoir-rocks. To summarize, the main difference regarding 2D and 3D micromodels is related to the constraints of the visualization setup. In principle, optical measurements cannot be used to visualize flow through the depth of the model, thus requiring the usage of confocal microscopy for 3D applications [70]. In fact, the visualization of fluid flow through a micromodel is a major concern when performing EOR microfluidic experiments.

2.1.2 Micromodel pore-networks

Until the 1980s, most micromodels were designed with simple and regular geometries. Later, the flow pattern of micromodels began to become more complex, mainly due to the use of computer generation. According to their geometry and topology, micromodels can be classified in four categories: perfectly regular [16,30,40,71–74,31–37,39], partially regular [19,41–48,75], fractal [76–79], and irregular [49,50,59–66,80,81,51–58].

In perfectly regular models, the pore depth and width and the distance between pores are constant throughout the domain. Also, the cross-sections of pores are generally square or rectangular. As one of the earliest perfectly regular geometry applications, Chen and Wilkinson [71] investigated the viscous fingering phenomenon in porous media in a etched-glass micromodel. Their pore-networks were fabricated as a square lattice of connected tubes. Another example of perfectly regular network micromodel was provided by Corapcioglu *et al.* [72] In their study, they modeled a solute transport in a horizontally mounted micromodel with a regular geometry of orthogonal channels. Fig. 2.7 shows a schematic view of their micromodel and pore-

networks. In fact, it must be stated that the final flow-networks in perfectly regular models may present some small variations due to the manufacturing processes.

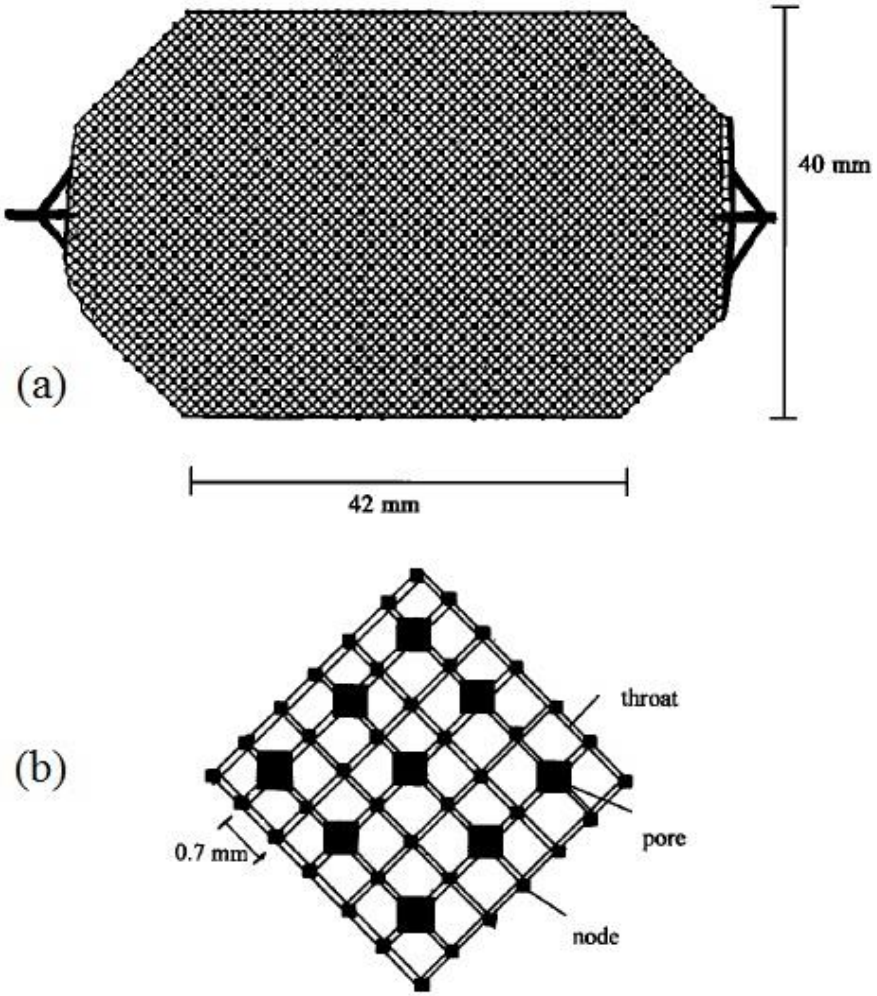

Fig. 2.7 – Schematic view of the micromodel pattern (a) and a magnified image of the pore-network and its elements (b) [72].

In partially regular micromodels, the pore bodies and pore throats form a regular pattern throughout the network. The cross-sectional shape of pores have the same format, however they may vary in size. The pore size distributions are generally based on statistical parameters and may be correlated or uncorrelated. Moreover, the permeability of the flow network is mainly dependent on the statistical parameters related to the generated pore size distribution. Tsakiroglou and Avraam [75] introduced a method to fabricate partially regular micromodels, and performed two-phase immiscible flow experiments to confirm their applicability. In their method, the microstructure was etched on a thin PMMA layer by using as input data the pore depth distribution and the pore aspect ratio (*i.e.* width-to-depth ratio) distribution. Fig. 2.8

shows an overview of their partially-regular micromodel with pore dimensions equal in shape and varying in size. By using their approach, pore geometric parameters of the network could be well-controlled and fabricated to their respective applications. The main disadvantage of perfectly regular or partially regular micromodels is the inability to model more complex scenarios, such as natural rocks or sophisticated flow networks.

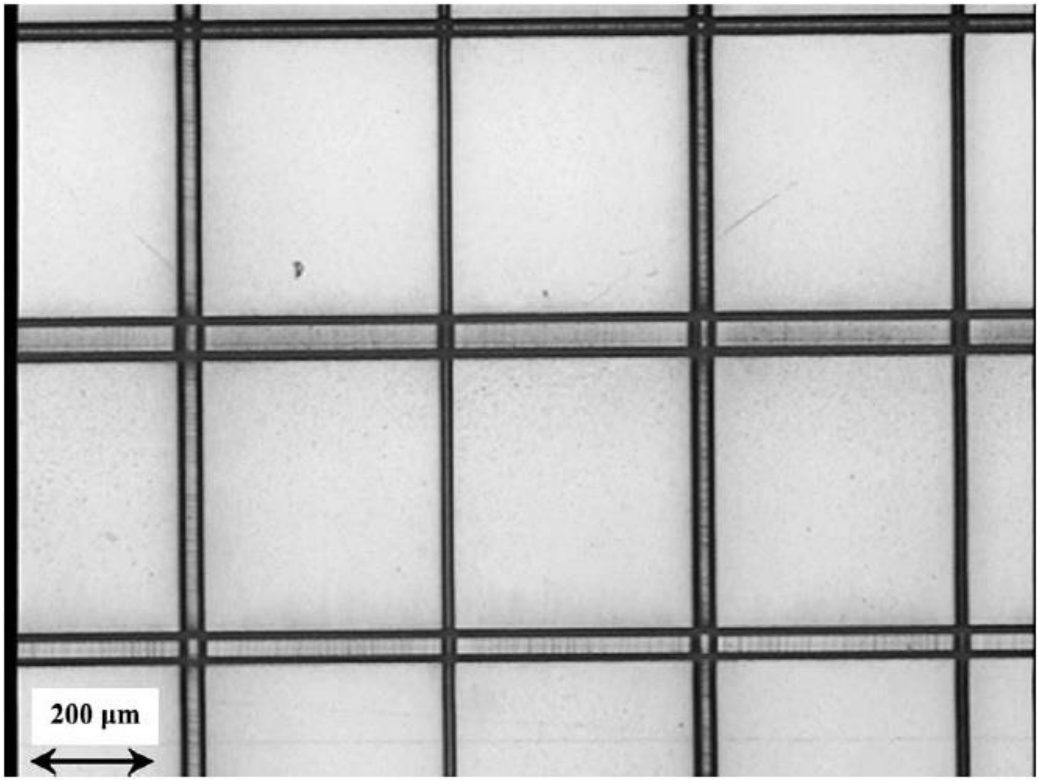

Fig. 2.8 – Overview of a partially-regular micromodel with pore dimensions equal in shape and varying in size [75].

Fractal geometries have been used in the last few decades to represent some of the porous medium in micromodels. In a broader sense, a fractal is a shape made of parts similar to the whole in some way, thus the term “self-similarity” or “expanding symmetry”. In fractal patterns, the replication is exactly the same at every visualization scale. Micromodels represented by fractal networks may appear to be completely irregular, but actually they are constituted of a mathematical pattern. In this context, the fractal patterns are generated according to the percolation theory, and they can either be spatially correlated or uncorrelated [82]. Spatial correlation means that fractal geometric dimensions are a function of the position in the network. According to this theory, the porosity of the model has to be at least 50% for a correlated network and 60% for an uncorrelated network for the occurrence of flow. Porosities lower than this threshold value exhibit insufficient connected channel across the micromodel. According to the

literatures, several researches have been conducted to model the flow networks of natural rocks by fabricating micromodels with fractal patterns [76–78]. A more recent application with fractal models can be found in the work of Cheng *et al.* [79] In their study, a photolithography process was used to fabricate the glass micromodels and a computer algorithm was applied to generate the fractal geometries, as shown by Fig. 2.9. The calculated porosity of the medium by image processing and it was equivalent to 64%, which is higher than the lower limit value established by the percolation theory. By using these fractal models, they were able to observe the relationship between interfacial areas of immiscible fluids and changes in pressure and saturation when two-phase flow was performed.

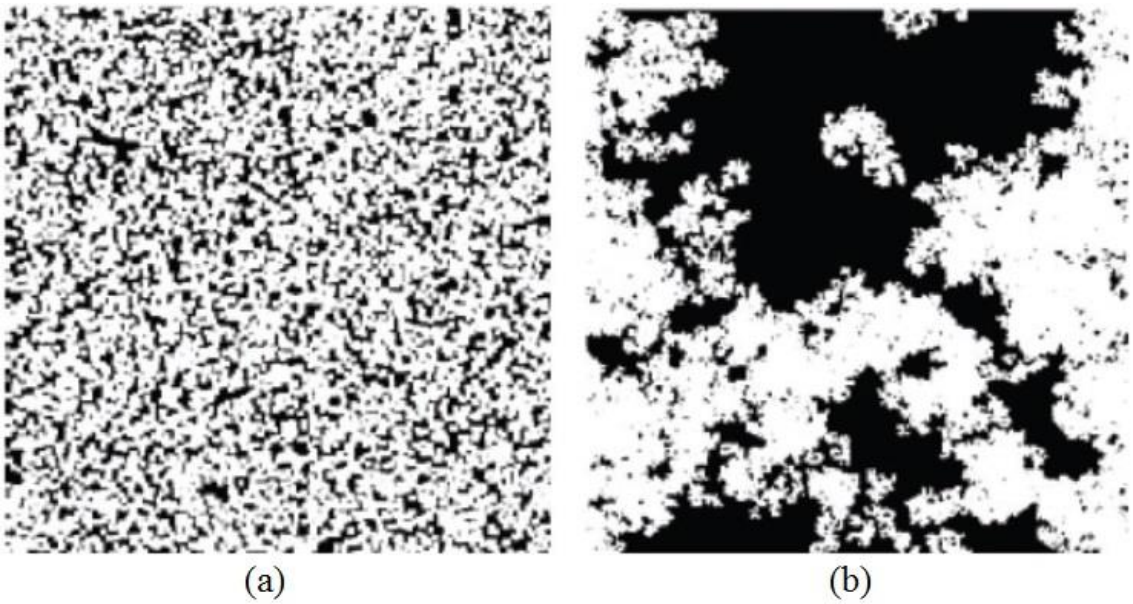

Fig. 2.9 – Examples of micromodels containing fractal patterns. (a) spatially uncorrelated pattern. (b) spatially correlated pattern [79].

At last, the pore networks of micromodels can be conceived by the generation of irregular patterns. In this category of networks, the main consideration for the geometry and features of the pattern is a lack of spatial correlation. Generally, pores or grains are randomly inserted in a domain while their sizes and geometrical shapes are chosen from statistical distributions. These irregular patterns are mostly designed to investigate flow behaviors in pore geometries that are present in either real porous media or in theoretical models. The main consideration when generating irregular patterns is to guarantee that fluids will be able to flow through all the connections of the model. In this context, Delaunay triangulation is frequently used to generate irregular patterns, since it requires that connections between nodes will not intersect each other [83].

Sandnes *et al.* [80] developed irregular pattern micromodels consisting of Hele-Shaw cell plates (Fig. 2.10). By the use of these random, labyrinth micromodels, they investigated viscous instabilities occurring between fluid-air interfaces, and compared their experimental data to numerical simulation results. Zhang *et al.* [81] provided another example of an irregular micromodel pattern based on Delaunay triangulation. They used a pore-network modeling (PNM) approach to enable the micromodel flow network and compared their flow results to numerical simulations (Fig. 2.11). To sum up, more sophisticated fractal and irregular patterns are recommendable when performing fluid displacement experiments in micromodels, while perfectly or partially regular patterns are suitable when understanding physical phenomena between fluids or deposition of compounds.

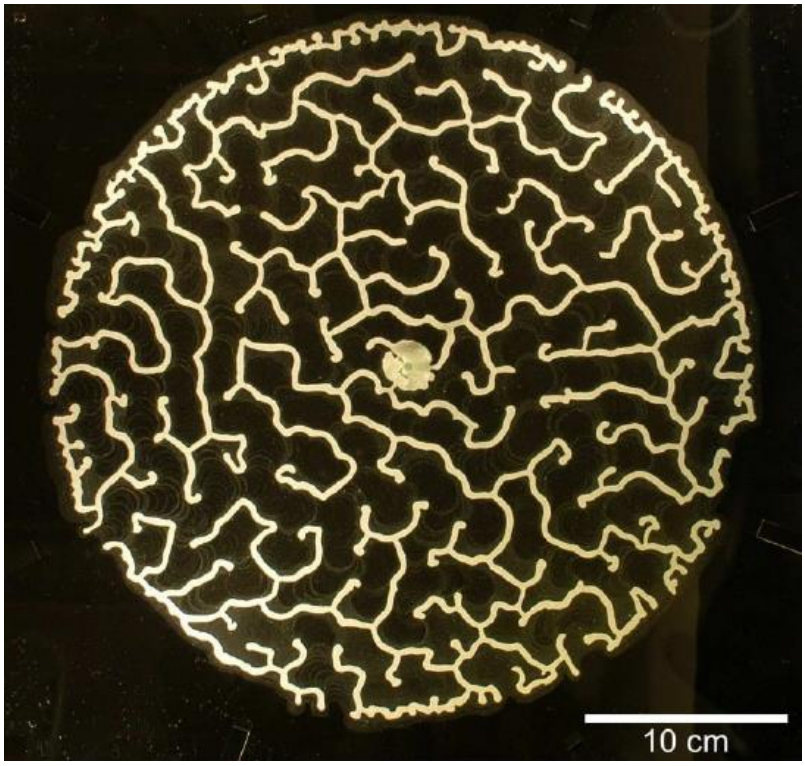

Fig. 2.10 – Overview of an irregular pattern labyrinth micromodel used in viscous fingering studies [80].

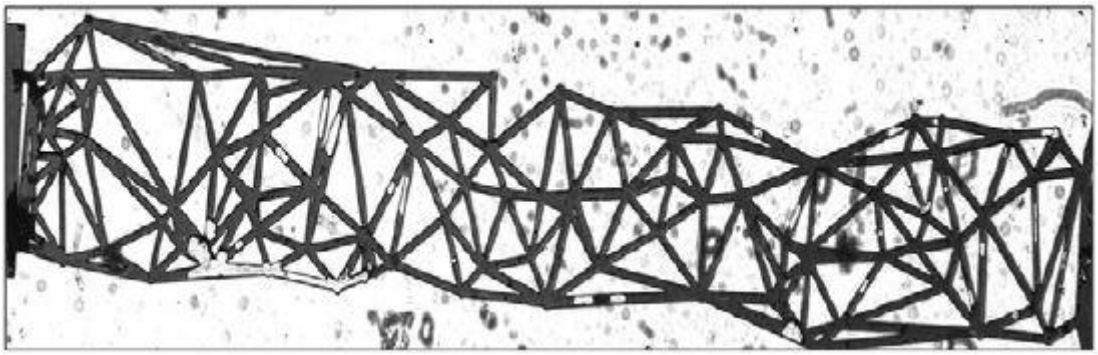

Fig. 2.11 – Irregular pattern micromodel based on Delaunay triangulation and designed by the pore-network modeling (PNM) approach [81].

When modeling real sedimentary rocks, the different geochemical processes of generation and dissolution of materials may significantly increase the complexity to describe their features [84]. In this context, rock texture is a key content to be considered when modeling real-rocks. It indicates the way particles or minerals were put together to constitute the rock. The particles size and distribution are responsible for the two most important petrophysical properties of a rock, *i.e.* porosity and permeability. As a recent approach that considered the rock texture, Park *et al.* [85] proposed a method to fabricate a rock-based micromodel by digital alterations of X-ray micro-CT images of Boise rock. Fig. 2.12 shows the process flow of their rock-based micromodel. They used a depth averaging technique to convert a 2.5D tomography slice into 2D, and then CFD simulations and CAD adaptations to guarantee flow through the network. A disadvantage is that 3D flow connections might be lost. To solve this problem, some grains must be removed manually to enable connections through pores that do not exist. Secondly, micro-CT images are unable to capture microporosities due to very-high magnification required. Finally, a solution to generate the pore-network is to incorporate grain-size distribution and statistical parameters. This might be done by using field values of these statistical parameters as inputs on a computer mesh generator algorithm.

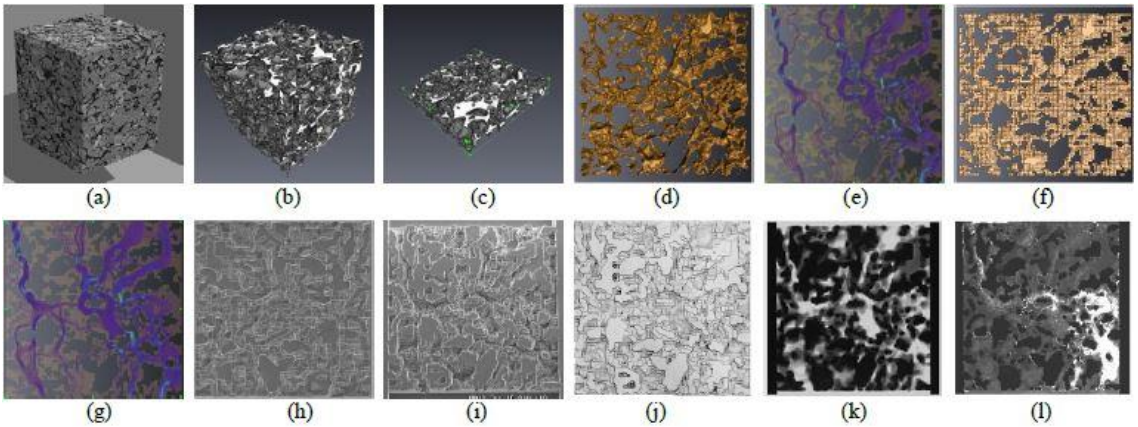

Fig. 2.12 – Process flow of the 2.5D rock-based micromodel. (a,b,c,d) refers to the obtaining, slice sectioning and depth averaging of the X-ray micro-CT image. (e,f,g) refers to CFD simulations in the 2.5D micromodel. (h,i) refers to SEM images of the brass mold and PMMA fabricated micromodel, respectively. (j,k,l) refers to microscopic images of the micromodel filled with water, dye, and particle flow experiment, respectively [85].

When constructing the porous network by a statistical approach, two different strategies may be taken: via pore-size distribution or via grain-size distribution. As a general approach in the oilfield, a pore-size distribution is obtained by injecting mercury at step-wise increasing pressures in a core sample [25]. The larger pores are filled first for lower pressures, followed by smaller pores at successfully higher pressures. An innovative method to obtain the pore-size distribution of a rock sample is to perform micro-CT imaging with pore-scale resolution [86]. However, this method requires some computational efforts, since some 3D connections in real-rocks must be adapted to 2D in order to enable flow in the micromodel. On the other hand, grain size distributions are more easily determined. The grain size is customarily defined as the average diameter of grains in sediments or lithified particles in rocks, expressed in millimeter. According to their size, the grains of clastic rocks can be classified in several broad classes, with each class corresponding to a specific rock type (Table 2.1) [87]. The grain sizes are commonly determined by two routine methods: sieve analysis and sedimentation method [84]. The results of grain-size analysis are often displayed as grain-size distribution curves. Generally, these results normally include cumulative grain-size distribution curves and grain-size frequency histograms. The statistical parameters of the grain-size distribution curves are directly related to most of petrophysical properties of rocks. Therefore, changes in porosity of rocks can be easily

analyzed when varying the shape of the grain-size distribution used to generate the porous network.

Table 2.1 – Grain-size classes for sediments and clastic rocks [87].

Grain-size [mm]	Class	Sediment	Rock
>1000	Boulder	Gravel	Conglomerate and breccia
100-1000	Cobble		
10-100	Pebble		
2-10	Granule		
1-2	Huge sand	Sand	Sandstone
0.5-1	Coarse sand		
0.25-0.5	Medium sand		
0.1-0.25	Fine sand		
0.05-0.1	Coarse silt	Silt	Siltstone
0.005-0.05	Fine silt		
<0.005		Clay	Claystone (mudstone)

An important parameter that relates the grain-size statistical parameters and rock petrophysical properties is grain sorting. The sorting of a grain population is a measure of the range of grain-sizes and their spread around the mean grain size [87]. It is basically an indication of the uniformity of the grain-sizes within a rock. In well-sorted rocks, the grains are very similar in size, while poorly-sorted rocks have a wide distribution of grain-sizes. Regarding their petrophysical properties, well-sorted rocks are generally more porous and have high permeability, while poorly-sorted rocks have a lower porosity and permeability. A widely used statistical parameter to determine the degree of sorting within a rock is the standard deviation of the grain-size distribution. Folk and Ward [88] proposed a formula to calculate this standard deviation:

$$\sigma = \frac{\phi_{84}-\phi_{16}}{4} + \frac{\phi_{95}-\phi_{5}}{6.6}, \quad (1)$$

where phi (ϕ) is a logarithmic transformation: $\phi_i = -\log_2 d_i$; d_i is grain diameter in millimeters; the subscripts 5, 16, 84, and 95 represent percentiles of a cumulative grain-size distribution curve. By Eq. (1), the standard deviation of regular grain-size distributions generally ranges from <0.35 to >4.00. Fig. 2.13 shows a schematic representation of varied sorting levels within a rock and their associated standard deviation range values. As followed by intuition, well-sorted rocks have lower standard deviation, while poorly-sorted rocks have higher standard deviation. Beard and Weyl

[89] investigated the relation between sorting and porosity in artificially mixed and wet-packed sands. Table 2.2 shows their results and respective values.

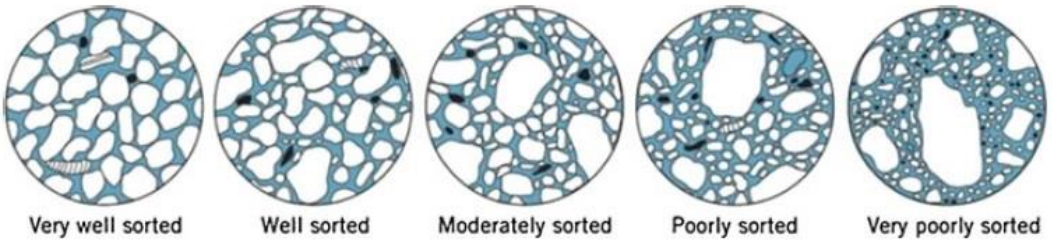

Standard deviation	<0.35	0.35–0.50	0.50–0.71	0.71–1.00	1.00–2.00	2.00–4.00	>4.00
Scale	Very well sorted	Well sorted	Moderately well sorted	Moderately sorted	Poorly sorted	Very poorly sorted	Extremely poorly sorted

Fig. 2.13 – Schematic diagram of sorting levels of sediment particles and a sorting classification scale based on standard deviation ranges [84].

Table 2.2 – Relationship between sorting level and average porosity for artificially mixed and wet-packed unconsolidated sands [89].

Sorting	Average porosity
Extremely well	0.424
Very well	0.408
Well	0.390
Moderately	0.340
Poorly	0.307
Very poorly	0.279

2.2 Nanofluids for EOR

Nanotechnology has become the buzz word of the last decade. The precise manipulation, control, and properties of matter in the 1-100 nanometers dimension have revolutionized many industries. In this context, several reviews regarding the general applications of nanotechnology in the O&G industry have been published recently [6,90–92]. More specifically, a series of reviews concerning the use of nanotechnology in EOR have also been made [5,73,93–97]. Traditional EOR techniques generally face important challenges regarding their broader use in a field scale. Chemical methods, for example, are often limited by the high cost of chemicals, possible fluid losses during injection, and formation damage [98]. In gas methods, the high mobility ratio between injected gas and oil may lead to the formation of viscous fingers, resulting in a large amount of residual oil being uncovered during the process [99]. Thus, less expensive,

environmental friendly and more efficient EOR methods are required. Nanoparticles (NP) have the ability to offer alternative solutions to unsolved challenges in EOR. The first of NPs primary advantage in EOR is related to their ultra-small size [100]. Being smaller than regular pore bodies and throats, NPs can easily flow and block some ultra-small connections, thus increasing permeability in adjacent larger pores. Moreover, they can penetrate and flow through some pores that traditional injected fluids are unable to, hence contacting more swept zones and increasing macroscopic sweep efficiency. The second advantage of NPs is their very high specific surface area [101]. The reduced NPs size improves some surface performance characteristics that are of great importance to oil recovery. Finally, an additional concern to the use of chemical in field scale is their environmental friendliness. In this context, most of the NPs frequently used are less harmful to the environment when compared to chemicals. For example, silica NPs, the most common nanoparticles in EOR, are composed of the same principal mineral component of sandstones reservoirs [45].

The comprehension behind the principal recovery mechanisms to be achieved is of great importance when designing a nano-assisted EOR application. In this context, each nanoparticle formulation can address to specific objectives. NPs can be generally used in three different forms in EOR: nanoemulsions, nanocatalysts, or nanofluids. Nanoemulsion is basically an emulsion stabilized by NPs, with droplet size in the range of 50-500 nm [102]. The unique physicochemical characteristics of nanoemulsions suggest that they can be successfully used to recover the residual oil trapped in the small pores of reservoir rocks by capillary forces. Nanocatalysts can be defined as nano-sized metal particles used as catalysts for EOR during steam injection in heavy oil reservoirs [103]. Their primary function is to upgrade the heavy oil into lighter products by the means of chemical reactions known as aquathermolysis. The third NPs approach and motivation of this work is the use of nanofluids. The term “nanofluid” concerns to any base fluid with nanoparticles dispersed as a colloidal suspension. The base fluid can be water, oil or gas. Being first developed for other applications, the use of nanoparticles as nanofluids have recently acquired a greater attention as a potential to EOR operations.

The preparation of nanofluids requires a careful process. The nanoparticles must be encountered in stable suspension in a base fluid over a long period of time, with little or no agglomeration of particles and no chemical change of the fluid [104]. If unstable, the nanoparticles may lose their potential in oil recovery processes. Devendiran and

Amirtham [105] provided a full review about the various methods to enhance the stability of nanofluids. A common method is to change the pH value far from the isoelectric point (IEP). In the IEP, the zeta potential of a fluid is zero, meaning that hydration or repulsive forces between suspended particles are negligible. Therefore, there is a high tendency of particles coagulation in the IEP [106]. Also, high zeta potential values are an indication of high hydration forces between NPs and good stability [107]. Another method to enhance nanofluid stability is to use surfactants. Surfactants can create continuity between NPs and basefluids by acting as a bridge between them [108]. The created connection increases the dispersion and stability of NPs in the basefluid. The other method to prepare nanofluids is the ultrasonic vibration, either as a bath- or probe-based device [109]. By ultrasonication, high frequency waves generate a continuous agitation, promoting a physical dispersion of the nanofluid.

Currently, there is a broader sense about the major EOR mechanisms related to nanofluid injection. Fig. 2.14 describes some of these reported mechanisms [5]. As one of the most important mechanisms, Fig. 2.14(a) shows the osmotic generation of a structural disjoining pressure [110]. The injection pressure in the nanofluid causes the NPs in suspension to arrange themselves in well-ordered layers in the confined region between the oil phase and rock/connate brine. These well-ordered layers of NPs form a wedge-shaped film that locally increases the entropy of nanofluids and exerts a disjoining pressure at the interface more than that of the bulk liquid. This additional pressure acts to separate the oil phase from the rock, thus recovering more oil than previously possible with traditional injection fluids. The process of generation of the disjoining pressure is basically osmotic, and is related to the Brownian motion and electrostatic repulsion of the nanoparticles. Parameters that affect this pressure are: NPs size and amount, temperature and salinity of nanofluids, and surface characteristics of the rock. When large amounts of NPs are present, the upward force can be up 50,000 psi [111]. Hendraningrat *et al*. [112] studied the effect of some influencing parameters in SiO_2 nanofluid flooding, especially particles-size. They performed contact angle and coreflood analysis for 7nm, 16nm, and 40nm average-diameter silica nanoparticles. The study showed an incremental oil recovery as nanoparticle size decreased. Meanwhile, contact angles also decreased with decreased size. They claimed that, as nanoparticles size decreases, their ability to flow through smaller size pore throats and mobilize some residual oil increases, mainly due to the structural disjoining pressure mechanism. El-

Diasty [113] also analyzed the effect of SiO_2 NPs size (5nm to 60nm) for nanofluid flooding in an Egyptian sandstone formation. Its results confirmed the same conclusions taken by Hendraningrat *et al*. [112].

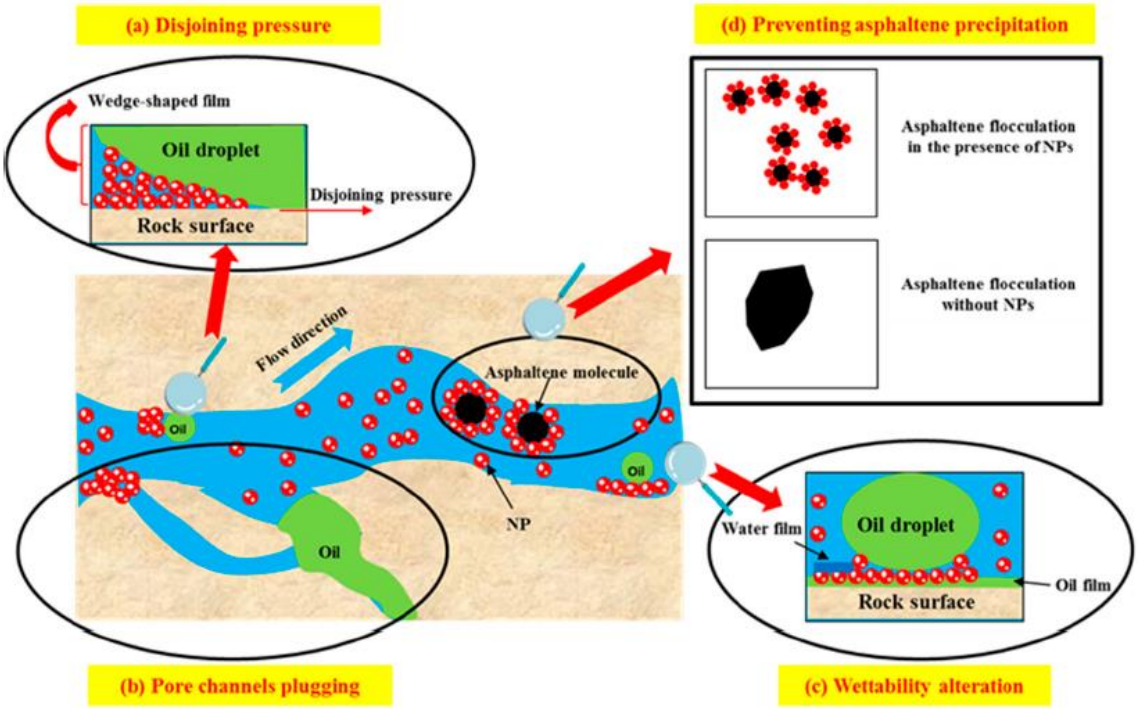

Fig. 2.14 – The schematic of some EOR mechanisms of nanofluids. (a) osmotic generation of a wedge-shaped film of well-ordered layers of NPs. This film locally increases the nanofluids entropy at the interface between oil phase and rock, thus exerting an additional disjoining pressure. (b) pore channels plugging of NPs, which diverts nanofluids flow to contact previously unswept regions. (c) wettability alteration to more water-wet conditions in order to enhance oil recovery. (d) prevent asphaltene precipitation by surface stabilization of NPs [5].

Fig. 2.14(b) shows the pore channels plugging EOR mechanism of the nanofluids. This mechanism is subdivided into two other mechanisms, depending mainly on the relationship between the size of the NPs and the size of the pore throats [114]. Both mechanisms are being illustrated by Fig. 2.15. If the NPs are larger than the pore throat, it is called mechanical entrapment. Usually, pore throat sizes are in microns, being thousand times higher than NP sizes. Therefore, the nanoparticles are able to flow through most of the rock pores without mechanical entrapment. However, some smaller rock connections in the nano-scale might exist, or larger metal NPs be injected [115]. These situations can generate mechanical entrapment of nanoparticles. On the other hand, if NPs are smaller than a pore throat and pore plugging occurs, it is called log-jamming. The narrowing of the flow area when nanofluids flow from pore bodies to

pore throats lead to an increase in velocity. This increase in velocity makes the H_2O particles of the base fluid to flow faster than the NPs in suspension, causing accumulation of NPs at the entrance of the pore throat. This NPs blockage promotes an additional pressure in the adjacent pore throat, thus releasing trapped oil. Once the oil is freed, the surrounding pressure drops and the NPs plugging gradually disappears. Both pore plugging mechanisms results in a diversion of nanofluids to contact previously unswept oil areas.

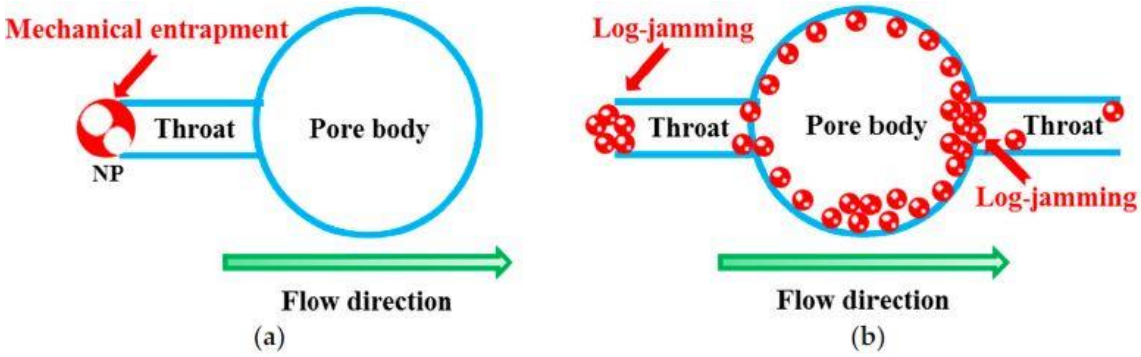

Fig. 2.15 – Schematic representation of the two pore channels plugging mechanisms caused by nanoparticles. (a) mechanical entrapment; when NP sizes are larger than pore throat sizes. (b) log-jamming; when NPs are smaller than pore throat sizes [115].

The third mechanism denoted by Fig. 2.14(c) is wettability alteration promoted by nanofluids. As a key parameter governing oil recovery, the wettability of the rock has a direct relationship to other petrophysical measurements, such as capillary pressure and fluids relative permeability. At a constant saturation, a more water-wet condition implies in lower capillary pressure and higher oil relative permeability [116,117]. These two trends enable a higher percentage of oil to be recovered during production. Therefore, the wetting tendency of the rock is related to the oil recovery factor. According to the literature, different nanoparticles have been experimentally tested in different rock types regarding wettability changes. Giraldo *et al*. [118] demonstrated the wettability alteration by alumina-based nanofluid injection in sandstone cores. Fig. 2.16 shows their experimental results of relative permeability before and after Al_2O_3 injection, indicating an increase in oil relative permeability after treatment. Hendraningrat *et al.* [119] also demonstrated the role of Al_2O_3 NPs in wettability alteration of sandstones. Li *et al*. [64] and Roustaei and Bagherzadeh [120] conducted experiments by injecting SiO_2 NPs in sandstone and carbonate cores, respectively. Both results showed that silica nanoparticles can be used as wettability modifiers for these

two types of rocks. The effect of TiO_2 NPs as wettability modifier in quartz plate has also been experimentally demonstrated [121] The use of SnO_2 NPs has also been reported [93]. Finally, Karimi *et al.* [122] found that ZrO_2-based nanofluids promoted wettability change of carbonate reservoir rock.

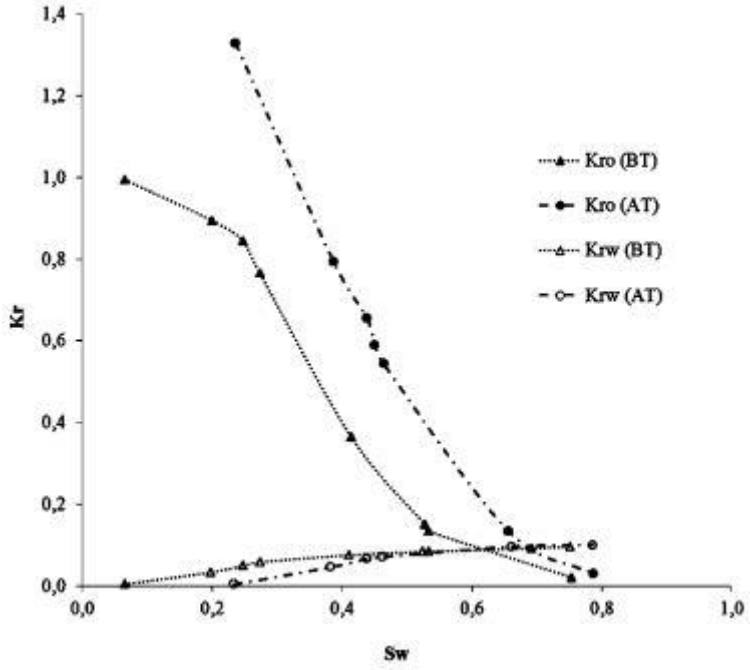

Fig. 2.16 – Relative permeability curves before and after alumina-based nanofluid injection in sandstone core. The symbols represent experimental data. The notation AT and BT indicates that measurements were carried out after treatment or before treatment, respectively. At a constant saturation, the injection of Al_2O_3 nanofluid increased oil relative permeability and decreased water relative permeability [118].

The precipitation and deposition of high-molecular-weight components of petroleum in surface facilities, tubulars and within the reservoir is a well-known production problem [123]. A common example is asphaltene. Asphaltenes precipitation is caused by a number of factors including changes in pressure, temperature and composition. The two main causes of precipitation are reduction in pressure during primary depletion and mixing of oil with injected solvent (mainly hydrocarbon gases or CO_2) in IOR processes. In the reservoir, asphaltenes precipitation leads to undesirable wettability alterations and formation permeability reduction. Thus, solutions able to mitigate asphaltenes precipitation during IOR processes are greatly needed. In this context, some researchers have found that NPs are effective to prevent asphaltenes precipitation (Fig. 2.14(d)). Alomair *et al.* [100] tested a mixed nanofluids dispersion of SiO_2-Al_2O_3 and observed that as the concentration increased, asphaltene precipitation

was delayed. Tarboush and Husein [124] showed that NiO NPs have high affinity towards asphaltenes adsorption, being able to stabilize these components. Kazemzadeh *et al.* [125] investigated the effects of metal oxide nanoparticles (SiO_2, NiO, and Fe_3O_4) on oil recovery in a micromodel and determined how they adsorbed asphaltene and prevented its precipitation. A study went further and analyzed the effect of various parameters on asphaltene adsorption on NPs [126]. Its results showed that asphaltene adsorption increased with contact time between these components. The adsorption also increased with asphaltene content and decrease of temperature and water content in the medium.

Another major EOR mechanism in chemical flooding is the reduction in interfacial tension (IFT) between the oil phase and injection fluid. As mentioned before, reservoir engineers use capillary pressure relationships to predict flow capacity throughout the life of the reservoir. In this context, a lower capillary pressure will correspond to a higher flow capacity of fluids. A standardized relationship between capillary pressure and IFT is the Young-Laplace equation [127].

$$P_{cow} = P_o - P_w = \gamma_{ow}\left(\frac{1}{R_1} + \frac{1}{R_2}\right), \tag{2}$$

where P_{cow} is the capillary pressure between oil and water; P_o and P_w are the pressure of oil and water, respectively; γ_{ow} is the IFT between the oil and water phases; and R_1 and R_2 are the principal radii of curvature of the shared interface. The relationship in the way it is written is for water as the wetting fluid and oil as the nonwetting fluid. It shows that a reduction in the interfacial tension will lead to a decrease in capillary pressure, hence increasing production. Eq. (2) is also used experimentally to evaluate the IFT between fluid phases [128]. Several researches reported that some NPs can be potential agents to reduce IFT, being another EOR mechanism in nanoflooding. Hendraningrat *et al.* [44] evaluated the IFT for hydrophilic SiO_2 NPs suspensions with varied concentration in synthetic seawater (brine, NaCl 3wt.%) and synthetic oil. The dynamic IFT reduced from 65nM/m for brine to 28nM/m for 0.5wt.% SiO_2 NPs. Later, Hendraningrat *et al.* [10] repeated the experiments with the same NPs but used a North Sea crude oil instead. The IFT reduced from 19nM/m for brine to 8nM/m for a 0.05wt.% SiO_2 NPs. However, Li *et al*. [64] reported that SiO_2 NPs have no effect in IFT reduction. They conducted their experiments with 0.2wt.% SiO_2 NPs in 3.8wt.% NaCl synthetic seawater (SSW) containing hydrophilic acid (HCl) to stabilize the NPs

in two different pH values (pH = 2.0 and pH = 3.0). Only a slight reduction in IFT from 21.9nM/m to 16nM/m with NPs was observed but with varying pH instead. Moreover, it was reported that SiO_2 NPs stability (0.2wt.%) with HCl addition was improved from 1 day to 9 days. The role of other NPs in IFT has also been investigated. Hendraningrat and Torsaeter [121] reported that Al_2O_3 NPs (0.05wt.%) in synthetic brine with PVP stabilizer (1w.t%) have no effect in IFT. They have also tested TiO_2 NPs, but no results were obtained due to "fluid milkiness".

At last, another major EOR mechanism is reduction in the mobility ratio between fluid phases. The mobility of a fluid is defined as its relative permeability divided by its viscosity [129]. This parameter combines a rock property with a fluid property. Since viscosity is in the denominator, gases generally have a high mobility. As a key parameter in EOR, the mobility ratio is defined as the mobility of the injecting or displacing phase divided by the mobility of the remaining or displaced phase. For immiscible gas injection, the mobility ratio can be written as:

$$M = \frac{\frac{k_{rg}}{\mu_g}}{\frac{k_{ro}}{\mu_o}} = \frac{k_{rg}\mu_o}{k_{ro}\mu_g} = \left(\frac{k_{rg}}{k_{ro}}\right)\left(\frac{\mu_o}{\mu_g}\right), \quad (3)$$

where k_{rg} is the gas relative permeability; μ_g is the gas viscosity; k_{ro} is the oil relative permeability; and μ_o is the oil viscosity. The mobility ratio has a direct influence in the mechanics of oil displacement. High mobility ratios causes and early breakthrough and leads to viscous fluid instabilities, called as "viscous fingers" (Fig. 2.17) [130]. The formation of viscous fingers implies in a higher portion of the reservoir being uncovered by injection fluid, thus decreasing the macroscopic sweep efficiency of the recovery process. Therefore, a decrease in the mobility ratio of fluids is needed. Since relative permeability is a rock property, the reduction in mobility ratio is achieved by either decreasing oil phase viscosity or increasing injection fluid viscosity. As an example, Ogolo *et al.* [93] explained that Al_2O_3 is capable of reducing the oil phase viscosity in heavy oil reservoirs, achieving a higher recovery when the NPs were dispersed in brine. They also analyzed the use of Fe_3O_4 and Ni_2O_3 NPs. They reported that iron oxide performed reasonably to increase nanofluid viscosity; however nickel oxide had better results, since it can both increase nanofluid and decrease oil viscosities. Another study made by Shah and Rusheet [131] found that the viscosity of CO_2 gas stabilized by CuO NPs was 140 times greater than CO_2 alone, thus explaining the use of CuO NPs in EOR.

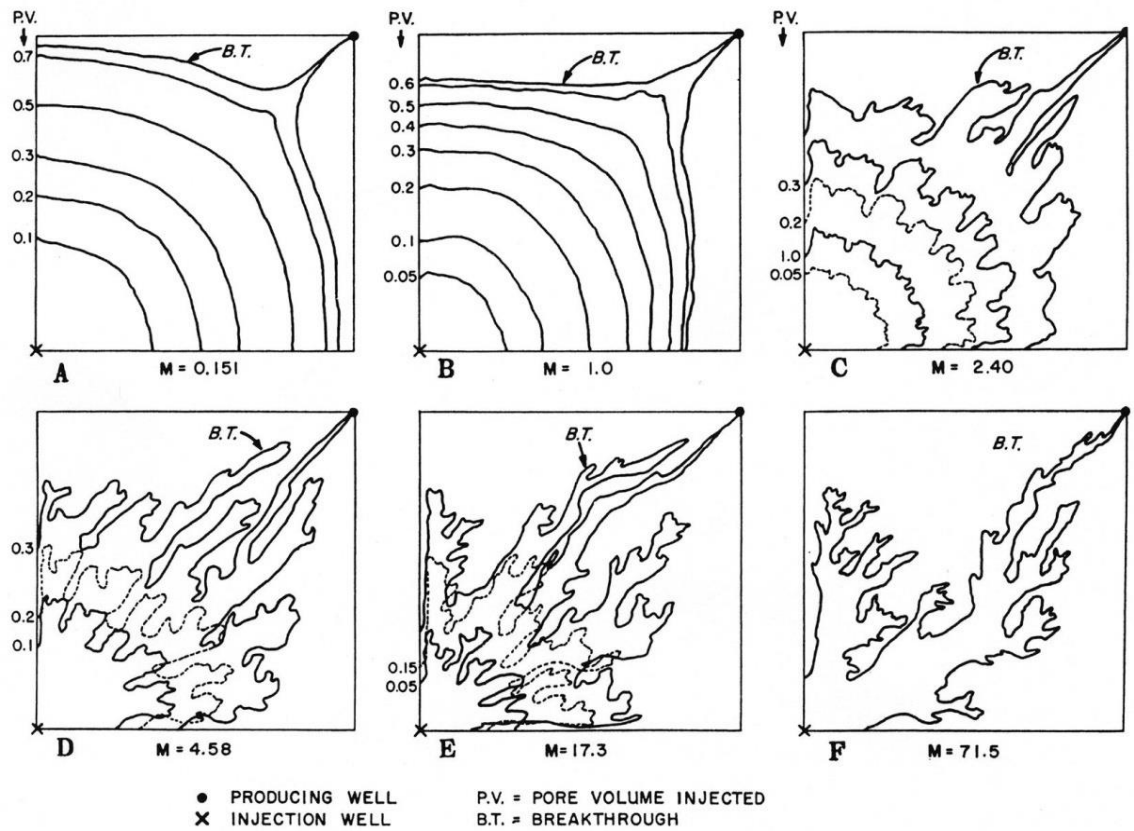

Fig. 2.17 – Gas/oil displacement fronts for various mobility ratios (0.151 to 71.5) and PV injected until breakthrough. The increase in mobility ratio leads to early breakthrough and viscous instabilities, called as "viscous fingers" [130].

As a very recent application of nanofluids for EOR, magnetic nanoparticles (MNPs) can be injected to aid the recovery of highly viscous fluids. In this context, the application of a magnetic field helps to overcome the low mobility ratio and high capillary pressure involved in the movement of heavy oil. Known as "ferrofluids", these MNPs are basically magnetite nanoparticles (Fe_3O_4) coated with a layer of super-hydrophobic material which selectively repels water and adsorbs oil. The applicability of ferrofluids has already been seen to clean-up oil spills in the Gulf of Mexico and was suggested by Shekhawat *et al.* [132] as a potential in EOR/IOR. The magnetic recovery mechanism would work by having an in-situ injection of nanofluids and forcing their movement toward the reservoir by the application of a repelling magnetic field from downhole tools. After adsorption with heavy oil, the coated MNPs would be retrieved by an inward attractive magnetic field toward the borehole. The authors also suggested an improved economic benefit in this mechanism as the injected nanoparticles can be recovered, separated from the adsorbed oil and further re-injected into the reservoir.

To summarize, several different research studies have been recently conducted to evaluate the effectiveness of the various nanofluids for EOR. In this context, the nanoparticles applicable to EOR can be subdivided into the three categories of metal oxide, organic and inorganic nanoparticles. Table 2.3 relates some of the nanoparticles reviewed in this chapter and their associated dominant EOR mechanisms. The main mechanisms observed for nanofluids were the decrease of the mobility ratio, IFT reduction and wettability alteration. Some nanoparticles require further investigation regarding their applicability for oil recovery. A more descriptive review about the studies performed with different nanoparticles for EOR was done by Negin *et al.* [95].

Table 2.3 – Some nanoparticles tested for EOR and their associated dominant mechanisms [95].

Nanoparticles	**Dominant EOR mechanism**				**Major References**
	Decrease the mobility ratio	IFT reduction	Wettability alteration	Require further investigation	
SiO_2		X	X		[10,45,64,93]
Al_2O_3	X		X		[93,121]
CuO	X				[131]
Fe_2O_3/Fe_3O_4	X				[93,132–134]
Ni_2O_3	X				[93,103,135]
SnO_2			X		[93,136]
TiO_2			X		[121,137]
ZrO_2			X		[93,122]
ZnO				X	[93,138]
Carbon-based				X	[139,140]

2.3 Nanofluids in micromodels for EOR

In the previous chapters, it was reported some of the different applications of micromodels in EOR and nanofluids in EOR, respectively. In micromodel experiments, most of the EOR studies were performed by chemical EOR injection (surfactants, polymers and alkalis). In contrast, nanofluids applications in EOR were mostly reserved to coreflood analysis. In fact, only a few research studies have been conducted by injecting nanofluids in micromodels [35,38,74,40,44–46,48,64–66]. Regarding the geometric regularity of the pore-network, the nanofluid/micromodel studies were divided in perfectly regular [35,38,40,74], partially regular [44–46,48] and irregular [64–66]. Also, all of these studies were performed in glass micromodels. The NP type used was mostly silica [44–46,48,64–66,74], with a few applications of alumina [35,40] and titanium dioxide [38].

The preparations of the nanofluids were considerably different for each NP formulation analyzed. Throughout the studies conducted with SiO_2 nanoparticles, the compositions of base fluids changed from solely deionized water to more complex solutions. For example, Rostami *et al*. [48] used deionized water only as the base fluid for its SiO_2 nanoparticles. Hendraningrat *et al*. [44] and Li *et al*. [45,46] prepared their silica nanofluids with a synthetic seawater (SSW) solution as base fluid (NaCl 3 wt.% and deionized water). Later, Li *et al*. [64] modified its SSW by adding more ions in its composition and also HCl to enhance nanofluid stability and evaluate the effect of pH in nanofluid performance. As another approach to enhance stability, Zallaghi *et al*. [74] and Mohajeri *et al*. [66] prepared their silica nanofluids by adding commercial surfactants in 10000 ppm NaCl brine solution and deionized water, respectively. At last, Barkhordari and Jafari [65] used four types of base fluids to disperse silica nanoparticles: distilled water, ethanol, n-hexane and gas condensate. Relative to alumina and titanium dioxide NPs, distilled water was used as the same base fluid in these studies, however titanium dioxide suspension was only maintained by the use of a commercial surfactant [35,38,40]. Regarding NP concentration, the majority of SiO_2 nanofluid were prepared in concentrations ranging from 0.01 wt.% to 0.5 wt.%. Only Barkhordari and Jafari [65] were able to prepare higher SiO_2 concentrations of 1 wt.% up to 5 wt.%. Alumina nanofluid studies were conducted with concentration ranges of 0.1% to 1%. Cheraghian [38] prepared titanium dioxide nanofluids by the use of a commercial surfactant in high concentrations of 2 wt.% to 2.4 wt.%.

Only a few studies have performed interfacial tension and contact angle analysis, being strictly reserved to SiO_2 nanoparticles. As the earliest study, Hendraningrat *et al*. [44] reported a IFT reduction from 65mN/m to 28mN/m with a 0.5 wt.% NP concentration and synthetic light oil (0.8g/cc and 2cp at 25°C). Li *et al.* [45] reported a reduction in IFT from 19mN/m to 9 mN/m with a lower NP concentration of 0.05 wt.% and North Sea light crude oil (0.82g/cc and 5.1cp at 25°C). Rostami *et al*. [48] also reported a IFT reduction from 20mN/m to 15mN/m with a 0.2 wt.% NP concentration and an Iranian light crude oil (0.87 g/cc and 17.7cp at 25°C). On the other hand, Li *et al*. [64] observed no IFT alteration by conducting experiments with a 0.2 wt.% NP concentration and light crude oil (0.89g/cc and 40.6cp at 25°C). They claimed this stable behavior due to the addition of HCl to stabilize the nanoparticles. At last, Mohajeri *et al*. [66] reported a slight IFT reduction from 21mN/m to 18mN/m with 0.1 wt.% NPs and an Iranian light crude (0.84g/cc and 6cp at 25°C). Regarding contact

angle, all of the studies have observed wettability alteration with nanoparticles. Li *et al.* [45] reported a CA decrease from 54° to 22° with a 0.1 wt.% NP concentration. Later, Li *et al*. [64] reported a CA decrease from 56° to 22° with a 0.2 wt.% NP concentration with HCl added (pH = 2.0), and Rostami *et al*. [48] observed a CA decrease from 135° to 88° with the same 0.2 wt.% NP concentration. Finally, Mohajeri *et al*. [66] performed CA measurements in a 0.1 wt. % NP concentration with and without commercial surfactant. Without surfactant, they reported a CA reduction from 100° to 78°. Surfactant solely reduced the CA from 100° to 73°, and the combination of surfactant and NPs dramatically reduced CA to 30°.

As a general requirement in all studies, micromodels were used to assess the pore-scale EOR mechanisms of the different nanofluid flooding techniques. These studies have also analyzed the differential pressure and permeability changes in the micromodel by nanofluid injection. Some have compared the experimental tests to CFD computer simulations [35,40,48]. However, only the most recent studies have evaluated the macroscopic efficiency of nanofluids in the oil recovery [38,48,64–66,74]. Regarding the SiO_2 NP experiments, Rostami *et al*. [48] reported a 9% additional oil recovery with a 0.2 wt.% NP concentration. Li *et al*. [64] had similar results, reporting a 11% additional oil recovery with the same 0.2 wt. % NP concentration. Mohajeri *et al*. reported additional oil recoveries by 0.1 wt. % NP with and without surfactants of 48% and 23%, respectively. Zallaghi *et al*. [74] have also performed experiments with surfactant addition, and reported an additional oil recovery of 23% with 0.2 wt.% NP concentration. Barkhordari and Jafari [65] conducted experiments with four different base fluids for SiO_2 nanoparticles. They reported an additional oil recovery of 21% with a high NP concentration of 5 wt.% in distilled water. Their additional oil recovery increased to 38% with the same 5 wt.% NP concentration when miscible gas condensate was used as the base fluid. As a different NP type, Cheraghian [38] performed titanium dioxide NP injection in a 2.2 wt.% concentration with surfactant addition and observed a slightly additional oil recovery of 5%. Macroscopic oil recovery experiments with alumina NPs have not been performed. Table 2.4 shows a list of research studies conducted with nanofluids in micromodels and some of their parameters and results.

In this study, the macroscopic oil recovery by SiO_2 NPs with biosurfactant addition will be evaluated in a PDMS micromodel containing an irregular well-sorted grain-size network. Additionally, interfacial tension and contact angle measurements will be performed to confirm the major EOR mechanism related to nanofluid flooding.

Table 2.4 – List of research studies conducted with nanofluids in micromodels and some of their respective parameters and results.

Author(s)	Year	Geometry	NP type	NP size [nm]	Base fluid	NF conc. [wt.%]	NF vis [cp]	Oil dens [g/cc]	Oil vis [cp]	IFT reduction [mN/m]	CA reduction [°]	Add. RF [%]
Hendraningrat *et al.* [44]	2012	Partially regular	SiO_2	15-50	NaCl (3 wt.%)	0.1 – 1	1.4 (1wt.%)	0.8	2	65 – 28 (0.5wt.%)	-	-
Li *et al.* [45]	2013	Partially regular	SiO_2	7	NaCl (3 wt.%)	0.01 – 0.1	1.017 (0.1wt.%)	0.82	5.1	19 – 9 (0.05wt.%)	54 – 22 (0.1wt.%)	-
Li *et al.* [46]	2014	Partially regular	SiO_2	7	NaCl (3 wt.%)	0.01 – 0.1	1.017 (0.1wt.%)	0.82	5.1	19 – 9 (0.05wt.%)	54 – 22 (0.1wt.%)	-
Li *et al.* [64]	2018	Irregular	SiO_2	7	SSW + HCl	0.2	-	0.89	40.6	0	56 – 22 (0.2wt.%)	11% (0.2wt.%)
Zallaghi *et al*. [74]	2018	Perfectly regular	SiO_2	7	NaCl (10 wt.%) + Surf	0.02 – 0.2	-	0.93	14	-	-	32% (0.2wt.%)
Barkhordari and Jafari [65]	2018	Irregular	SiO_2	-	Various	1 – 5	2.4 (3wt.%) 3.9 (5wt.%)	0.95	340	-	-	21% (5wt.%)
Mohajeri *et al*. [66]	2019	Irregular	SiO_2	15	Distilled water + Surf	0.02 – 0.1	-	0.84	6	21 – 18 (0.1wt.%)	100 – 78 (0.1wt.%)	23% (0.1wt.%)
Rostami *et al*. [48]	2019	Partially regular	SiO_2	20	Deionized water	0.05 – 0.2	1.0002 (0.2wt.%)	0.87	17.7	20 – 15 (0.2wt.%)	135 – 88 (0.2wt.%)	9% (0.2wt.%)
Meghdadi and Heyhat [35]	2013	Perfectly regular	Al_2O_3	40	Distilled water	0.1 – 1	1.215 (1wt.%)	-	-	-	-	-
Meghdadi and Afrand [40]	2017	Perfectly regular	Al_2O_3	40	Distilled water	0.1	1.215 (1wt.%)	-	-	-	-	-
Cheraghian [38]	2016	Perfectly regular	TiO_2	<100	Distilled water + Surf	2 – 2.4	-	0.97	1320	-	-	4.8% (2.2wt.%)

3 MATERIALS AND METHODS

This chapter will present the methodology developed by this work. First, it will be explained how the pore-networks of the micromodels were generated using a computer algorithm. Then, the process of fabricating micromodels containing the generated pore-networks will be described. As the other main area of this work, the preparation and characterization methods of nanofluids will be explained. To perform a nano-EOR experiment, the design of a microfluidic setup and microfluidic experimental method will be presented. At last, the procedure to acquire and process the captured images of flow during the EOR experiments will be described.

3.1 Pore-network generation

Following a statistical approach, the grain-size distribution and standard deviation were used to generate various pore networks with different sorting levels. This generation was done in collaboration with the D.Sc. candidate Raquel Fedrizzi. In this procedure, a computer algorithm in MATLAB was adapted from an original algorithm written by Enno de Vries, a Ph.D candidate advised by Ph.D Amir Raoof from the Department of Earth Sciences in the University of Utrecht, the Netherlands. The algorithm is divided into three main steps: set of input parameters; generation of grain-size distribution; and population of domain with random-form grains.

In the first step of setting the parameters, the size of domain in millimeters is required. Generally, micromodel domains are considered to be rectangular or square, although circular or different domain forms can also be generated. After that, statistical parameters of the desired grain-size distribution are inserted. These parameters consist in the minimum, maximum and mean grain radius; and the standard deviation of the grain-size distribution. It is important to note that the spread of the grain-size distribution is directly related to the domain size. In this context, if the relationship between the mean grain size and domain size is high, the number of inserted grains will decrease. On the other hand, if the domain size is enlarged, the number of inserted grains will increase, which can directly affect the microfabrication duration depending on the selected method. To account for changes in the shape of the generated grains, a polyshape function in MATLAB was introduced. The polyshape function can generate different geometric forms from an original form. It requires three inputs that are subdivided in the degree of deformation of the shapes, the number of polylines that will be used to create the new forms, and how the new forms will be similar to each other

(called blob width). After introducing the shape parameters, a minimum distance value between grains is required to guarantee flow through the generated porous network. Additionally, an estimation of porosity is required by the user. It is important to mention that the porosity of the generated network is generally higher than the estimated porosity, since part of the inserted grains will be located in the outer boundaries of the model. At last, the number of points in the domain in which the grains can be inserted is required. Table 3.1 shows the list of inputs necessary to generate the pore-networks.

Table 3.1 – List of inputs parameters to generate the pore-networks.

Input	Description
xMax	Domain size in the x-axis
yMax	Domain size in the y-axis
rMin	Minimum radius of the generated grains
rMax	Maximum radius of the generated grains
rMean	Mean radius of the generated grains
rStd	Standard deviation of the generated grain-size distribution
degree	Degree of deformation in the generated shapes
numPoints	Number of points that will be used to generate the polylines
blobWidth	Similarity of the generated forms to each other
minDist	Minimum distance between adjacent grains
porEst	Estimated porosity of the network
domPoints	Number of points in the domain in which grains can be inserted

The second step of the algorithm consists in the generation of the grain-size distribution. This generation is done by the use of the statistical input parameters presented before. First, a randraw function in MATLAB is used to generate a statistical distribution of numbers based on the statistical input parameters. This function is an efficient random variates generator which can generate over 50 different statistical distributions. In this context, a truncated normal distribution was chosen, since the normal distribution is considered as a basis model for grain-size distributions [84]. Moreover, the truncation eliminates values higher than the maximum radius and lower than the minimum radius. After the generation of the statistical distribution of numbers based on the input parameters, the statistical distribution is converted into a grain-size distribution. This step is performed by another function called randfor_poreflow, which was written by the group of Ph.D Amir Raoof from University of Utrecht and has a restricted access. Thus, the idea behind this function that converts statistical distributions to grain-size distributions will not be explained. As an adaption performed by this work, the standard deviation of a grain-size distribution proposed by Folk and

Ward´s formula (Eq. 1) is calculated. This is done by converting the generated grain diameters into a logarithm phi scale, arranging them in a frequency distribution, and calculating the percentiles shown by Eq. 1. By calculating the standard deviation proposed by Folk and Ward, the sorting level of the generated grain-size distribution can be obtained by Fig. 2.13.

In the third step of the algorithm, the population of the domain with the generated grains is performed. An important input parameter in this step is the domain points, since it is an indication of the number of possible options for the grain to be inserted. First, a random grain obtained by the grain-size distribution is selected and inserted into the domain, having its center exactly in a point stipulated by the domain points. Then, this grain is deformed according to the polyshape function and its respective input parameters. Furthermore, a second grain is chosen from the statistical distribution and inserted into the domain. However, before this step is done, the algorithm checks if this grain will overlap the other (or others) grain (s) in the domain. Moreover, it checks if the minimum distance between this additional grain and the other grains is guaranteed. After its insertion, the grain is deformed and the procedure continues. At each grain insertion, the porosity represented by the remaining blank area of the domain is calculated. The algorithm ends when the calculated porosity matches the porosity set by the user. Table 3.2 shows a list of the output parameters of the algorithm. The numerical output parameters are the final porosity; the number of grain inserted; the standard deviation of the grain-size distribution calculated by Eq. 1; the sorting level related to the pore-network, and the location and diameter of inserted grains. The image outputs of the algorithm are the image of the pore-network containing the grains and the graphical grain-size distribution. It is important to note that no numerical values regarding the shape deformations of grains are saved by the algorithm, thus the grain deformation step is only limited to the visual pore-network. Moreover, the difference between the final porosity and the estimated porosity may lead to a difference in the mean grain radius, since some smaller grains are inserted to fill the blank network. To summarize, Fig. 3.1 shows a flowchart containing the steps described to generate the pore-networks.

Table 3.2 – List of output parameters of the generated pore-networks.

Output	*Description*
porFin	*Final porosity of the network*
numGrains	*Number of grains inserted in the domain*
σFolk	*Standard deviation calculated by Folk and Ward´s formula (Eq. (1))*
sorting	*Sorting level obtained by* Fig. 2.13
locGrain	*Location of inserted grains*
diaGrain	*Diameter of inserted grains*
network	*Image of the generated pore-network*
grainDist	*Image of the generated grain-size distribution*

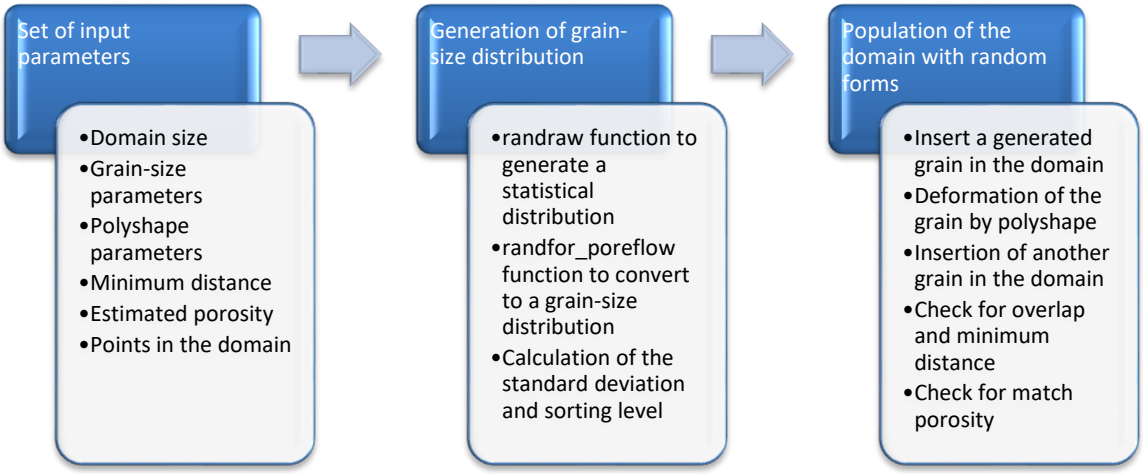

Fig. 3.1 – Flowchart of the steps described to generate the pore-networks.

3.2 Micromodels fabrication

The complete procedure to fabricate the micromodels was performed in LabMEMS/COPPE/UFRJ. It was divided in the micromilling process to fabricate the replica molding (REM), and the soft lithography process to manufacture the micromodel. This methodology to fabricate the micromodel was based in the work of Colman [23]. In the first step of the micromilling process, the generated pore-networks were inserted in a template by AutoCAD software. This template was designed in such a way to permit fluids to be injected through a connection line, migrate uniformly towards and through the pore-network, and exit by another connection line. As followed by literature, the architecture of the template plays a major role when performing a microfluidic analysis [141]. Therefore, some design parameters must be evaluated, such as the number and diameter of inlets/outlets, the roundness of corners, and the distance of the wide entrance region before the pore-network. Throughout this research, these design parameters have been altered after each unsuccessful flow experiment,

generating newer and more optimized templates. Some of the generated templates will be presented in the results section.

After the elaboration of CAD templates containing the generated pore-network, the micromodel fabrication procedure was conducted. This procedure combined the use of a CNC micro-milling machine to fabricate replica molds and soft-lithography to manufacture the PDMS micromodels. Firstly, CAD files were converted to program codes that represented instructions for precise movements to be carried out by the CNC micro-mill machine. The micro-mill machine basically works by removing raw material from a substrate with a miniature cutting tool made from a strong-resistance metal (Fig. 3.2). As an important manufacturing parameter, the diameter of the cutting tool must be smaller than the diameter of the micromodel features. Also, for 2D microfabrications, the relationship between the diameter of the cutting tool and the duration of the process is quadratic. Therefore, as an example, a 3-fold reduction in the tool diameter represents 9 more hours of fabrication. To create the molds, a 200μm diameter tungsten carbide micro tool (Performance Micro Tool) was used. The micro tool worked on an acrylic mold by cutting the substrate at a constant height of 100μm, thus creating the grains. After the replica mold fabrication, a cleaning procedure with deionized water was performed to remove impurities generated by the mechanical milling microfabrication.

Fig. 3.2 – Microdrill CNC milling machine used to fabricate the micromodel molds. A tungsten carbide micro tool cut through an acrylic substrate by the means of a program code. The removed material from the acrylic mold represent the grains of the pore-network [142].

With the microfabrication of acrylic replica molds containing the templates, the soft lithography process to manufacture the micromodel followed up. The selected material to conduct this process was the polymer PDMS (Sylgard 184, Dow Corning). The complete soft lithography procedure with PDMS has already been described in the literature [23]. In the first step of this procedure, a PDMS pre-polymer solution was mixed with a curing agent (Sylgard 184, Dow Corning) in a 10:1 mass/mass proportion. Air bubbles within the mixture were removed by a vacuum pump. The mixture was deposited onto the replica mold, and put back in a vacuum chamber to remove new air bubbles that might have appeared. Then, the replica mold containing the PDMS mixture was placed in an oven at 60°C for 2 hours to achieve full polymerization. After the curing process, the PDMS layers were carefully removed from the mold. It must be emphasized that this polymer slab consists in the lower half of the micromodel, with the grains at its superior plane. Therefore, the same lithography procedure must be conducted in another mold to enable a PDMS cover to seal the micromodel. After creating the cover, the two PDMS slabs must be bonded and sealed. This was done by applying a Corona treatment or air plasma at both polymeric surfaces and manually

bonding them. The Corona treatment is a surface modification technique that uses a low temperature corona discharge plasma to alter the properties of a surface [143]. The plasma is generated by applying high voltage to an electrode terminal. It must be noted that an insulating material was placed beneath the micromodel substrate in order to apply the Corona treatment. However, the application of plasma treatment on PDMS provides a temporary wettability change of the polymer surface [144]. In its main form, PDMS is hydrophobic, but when plasma is applied, it changes to hydrophilic and reverts back to hydrophobic after a period [145]. For that reason, all flow experiments were conducted in a minimum of 24 hours after plasma treatment. To conclude the micromodel fabrication, circular holes were made at the cover slab to enable the connection of the flow network with the outward injection lines. Fig. 3.3 shows a flowchart containing the steps described to fabricate the micromodel.

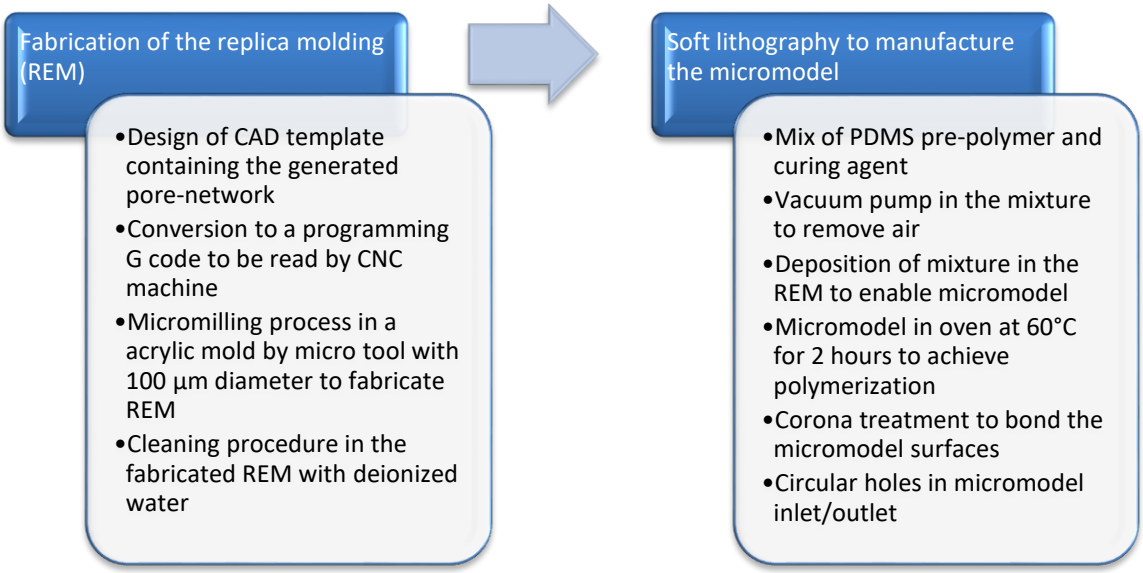

Fig. 3.3 – Flowchart of the steps described to fabricate the micromodel.

3.3 Nanofluids

The experimental procedure performed in this section was divided in two main parts: preparation of silica nanofluids and their characterization and interfacial-property measurements with oil and PDMS. The procedures to prepare the nanofluids and characterize their interfacial properties with oil/micromodel were performed in GRIFIT/COPPE/UFRJ in collaboration with the M.Sc. candidate student Nathália Dias. The nanofluid characterization measurements were made in LIAP/COPPE/UFRJ.

3.3.1 Preparation of nanofluids

The SiO_2 nanofluids were prepared by precursor silicon dioxide nanoparticles in nanopowder form, with average particle size of 12nm (Sigma Aldrich). Five different nano-SiO_2 concentration dispersions were designed: 0.01wt.%, 0.05wt.%, 0.1wt.%, 0.2wt.% and 0.5wt.%. This concentration range was chosen to match the concentration ranges of research studies conducted with SiO_2 NPs in micromodels [44–46,48,64,66,74]. Before explaining the preparation of the nanofluids, it is important to mention the safety procedures regarding the handling of nanoparticles. All of the following steps were conducted by wearing appropriate mask and gloves. As the first step, the precursor nanoparticles in a powder form were weighted in a precision balance (standard deviation of +-0.0002g) according to their respective desired concentration values. After weighting the NPs, the weighted samples were put in a flask in conjunction with a volume of base fluid measured by a volumetric pipette. Here, the base fluid selected was a nanofiltered NF90 water, in order to put in evidence the action of nanoparticles and suppress the action of ions present in conventional water. The complete procedure for obtaining and measuring the properties of NF90 water was described by Nicolini *et al*. [146]. This ultrapure water was obtained by a nanofiltration process on a seawater (SW) sample. The nanofiltration process used a commercial NF90 membrane and operated at a pressure of 15bars. The ion concentration in the permeate stream is a function of the membrane used for the nanofiltration. Table 3.3 shows the ionic compositions and properties of SW and NF90 water. It can be seen that the NF90 water has a much less ionic concentration when compared to SW. In this context, the ionic composition of the aqueous solution was analyzed by different methods in GRIFIT/COPPE/UFRJ. SO_4^{2-} and HCO_3^- concentrations were measured by ion chromatography (Metrohm, 882 Compact IC Plus), while the mono- and divalent-cations were determined by atomic absorption spectrophotometry (Perkin Elmer Analyst 200/400) and inductively coupled plasma optical emission spectrometry (Perkin Elmer Optma 5300 DV). The concentration of the others anions, Cl^- and Br^-, were obtained by potentiometric titration (Metrohm 808).

Table 3.3 – Ionic composition and properties of seawater (SW) and nanofiltered NF90 water [146].

Ionic concentration [mg/L]	SW	NF90	Ionic concentration [mg/L]	SW	NF90
Na^+	9532	467	Cl^-	18.855	780
K^+	490	23	Br^-	53	1.0
Mg^{2+}	1261	5.2	SO_4^{2-}	2548	49
Ca^{2+}	371	1.1	HCO_3^-	145	19
Ba^{2+}	1.0	0.4	pH	7.4	6.5
Sr^{2+}	5.4	0.0	Density [g/cm³]	1.022	0.998

After putting the NPs together with the ultrapure water, an ultrasonication method was selected to disperse the nanoparticles. This ultrasonication procedure consisted in inserting the nanofluid samples inside a profiled probe which applied ultrasonic vibration in 90W in a sequence of 3 steps of 9 min periods with another 9-min rest period to avoid overheating, which could affect the NPs properties. Fig. 3.4 shows the prepared SiO_2 nanofluids in varied concentrations, with NP concentration increasing from right to left. It can be seen that as the NP concentration increases, the turbidity of the dispersions also increases. After preparing the nanofluids in an ultrapure water, the same procedure was repeated with the addition of a biosurfactant. The biosurfactant was used in collaboration with the D.Sc. candidate Viviane Prates from EQ/UFRJ. In her research, the biosurfactant was obtained after the extraction of fatty acids from glycerin, one of the major by-products of biodiesel production process [147]. This biosurfactant helps to maintain the nanoparticles in stable suspension for a longer time, thus preventing sedimentation and progressive flocculation. During the nanofluid preparation, the biosurfactant is added before the ultrasonication. Regarding its use, a biosurfactant concentration of 0.05wt.% was chosen, which is equivalent to the critical micellar concentration (CMC) of this product. The CMC is defined as the concentration of surfactants above which micelles form and all additional surfactants go to the micelle system. In this concentration level, the biosurfactant is most effective to decrease the interfacial tension between the NPs and the base fluid.

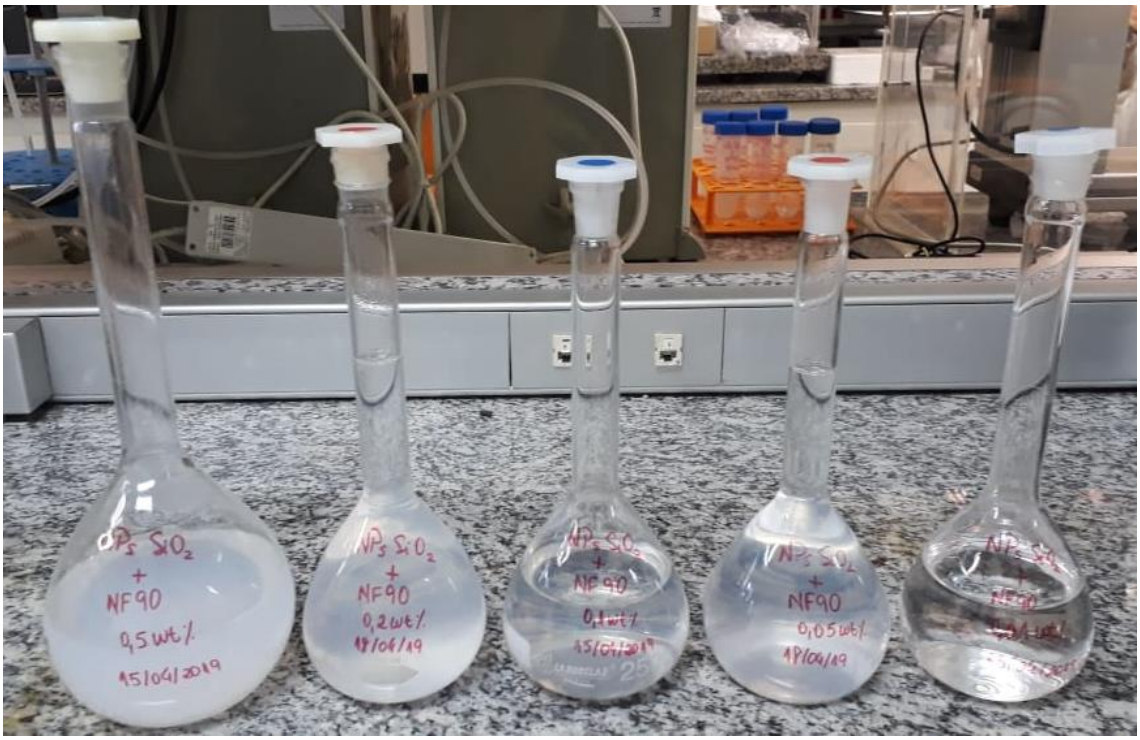

Fig. 3.4 – Prepared SiO_2 nanofluids in varied concentrations. From left to right: 0.5 wt.%, 0.2 wt.%, 0.1 wt.%, 0.05 wt.%, 0.01 wt.%.

3.3.2 Nanofluids characterization and interfacial measurements

In order to characterize the prepared SiO_2 nanofluids, zeta potential and particle size analyses were performed. These measurements were conducted using a Zetasizer Nano S90 (Malvern Instrument). In this instrument, the average hydrodynamic diameters of the nanoparticles were measured by dynamic light scattering (DLS) method, while zeta potential were measured by the phase analysis light scattering method (PALS). All measurements were conducted in triplicates to improve precision and in 1 hour after nanofluid preparation to evaluate stability in a short period.

To evaluate interfacial properties, a Brazilian pre-salt oil sample (LRAP/COPPE/UFRJ) was selected. Table 3.4 shows some of the oil properties, including API gravity, specific gravity and viscosity at different temperatures. The oil specific gravity was measured by densitometer (DMA 4500, Anton Paar, LRAP/COPPE/UFRJ), while the dynamic viscosity was measured by viscometer (SVM 3000, Anton Paar, DOPOLAB/COPPE/UFRJ). To evaluate the interfacial properties of nanofluids in contact with pre-salt oil and PDMS, a goniometer instrument was used (Dataphysics OCA 15, Germany). Fig. 3.5 shows a schematic of the goniometer arrangement to evaluate IFT (Fig. 3.5(a)) and contact angle (Fig. 3.5(b)) [146].

Interfacial tension values of prepared nanofluids and pre-salt oil systems were obtained using the pendant-drop method. In this technique, an oil drop is left pendant in a nanofluid medium as the external phase inside of a transparent quartz cell. After stable, the contour of the oil pendant-drop is measured optically and fitted with a contour calculated by the Young-Laplace equation (Eq. 2) to obtain the IFT between the fluid phases [148,149]. On the other hand, the wettability of the PDMS was evaluated in the same goniometer but using a sessile-drop method instead [150]. By using this method, a drop of pre-salt oil was placed at the PDMS surface with nanofluid as external phase in the same quartz cell. The contact angles for each nanofluid concentrations were determined by fitting a contour on the drop via Eq. 2, considering the micromodel surface as the baseline of the measurements. To summarize, Fig. 3.6 shows the flowchart containing the steps required to prepare, characterize and evaluate the interfacial properties of nanofluids.

Table 3.4 – Properties of pre-salt Brazilian crude oil.

API gravity [°]	24.71	
Temperature [°C]	Density [g/cm^3]	Viscosity [cP]
20	0.9016	306.920
25	0.8904	219.210
40	0.8867	59.621
60	0.8722	20.289
80	0.8586	10.785

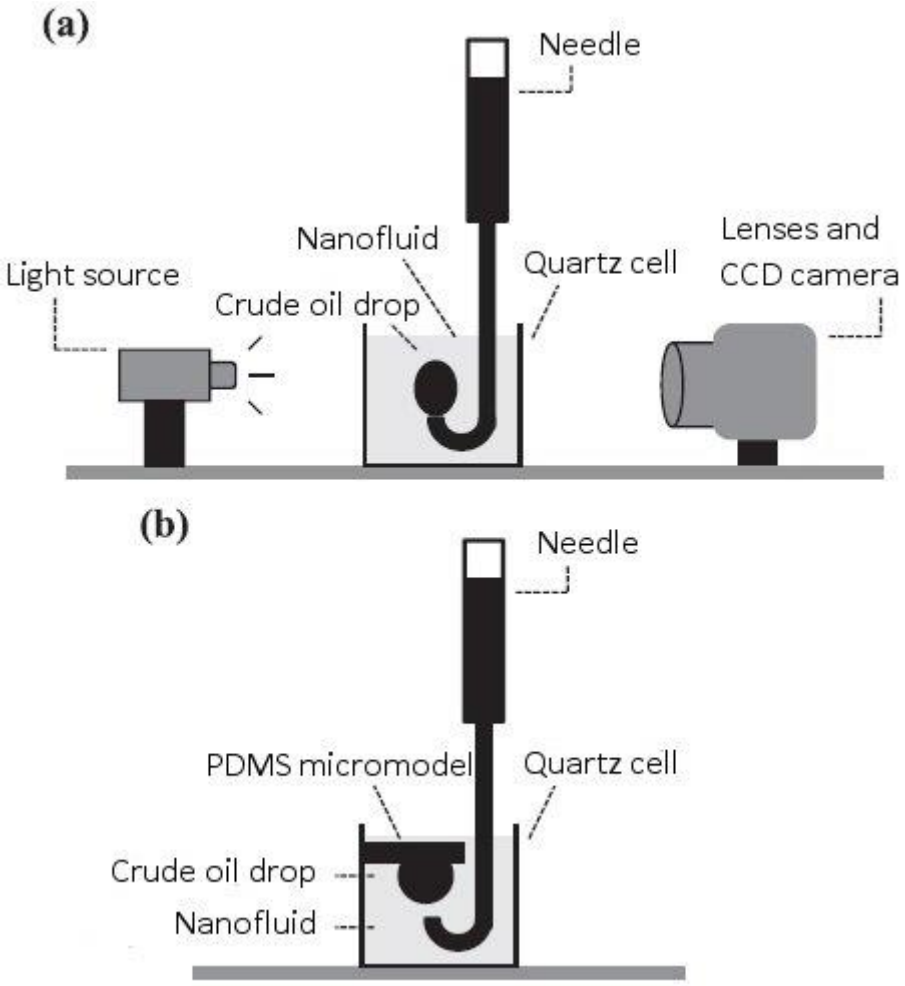

Fig. 3.5 – Schematic diagram of the goniometer instrument to evaluate (a) IFT measurements and (b) contact angle measurements [146].

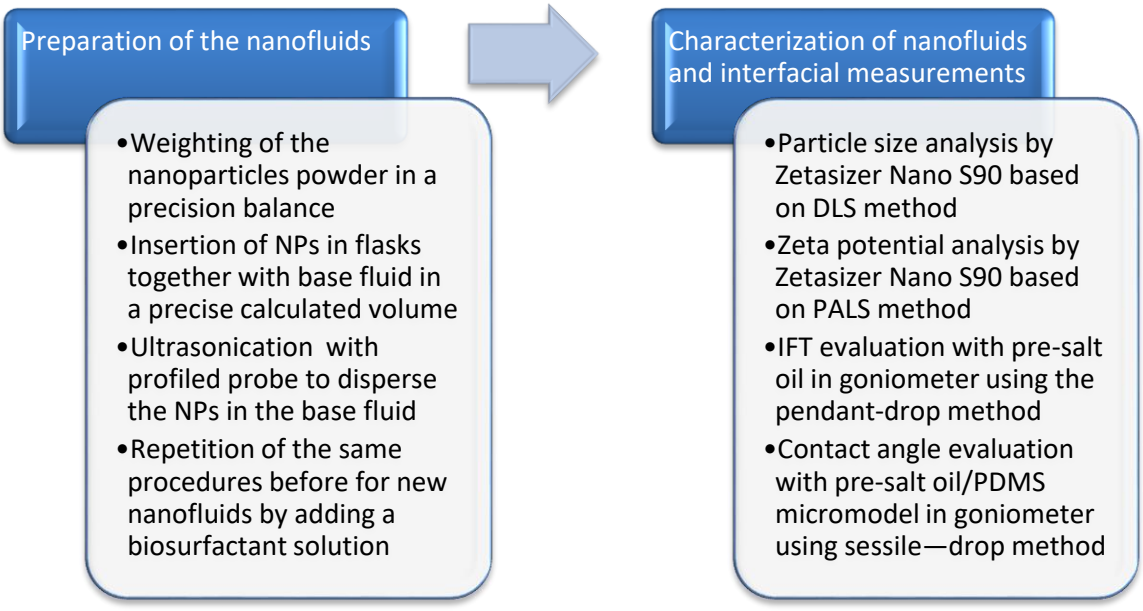

Fig. 3.6 – Flowchart of the steps described to prepare and characterize the nanofluids.

3.4 Microfluidic setup and EOR experimental method

Visualization methods in micromodels are commonly classified in four groups: use of cameras, microscope visualization, photo-luminescent volumetric method, and fluorescent microscopy [18]. The choice of whether taking pictures or recording videos is basically a function of the variable of interest. In fluid-displacing experiments, two variables may be analyzed: the average saturation of fluids in the entire flow network or specific fluid-fluid interfaces. Furthermore, a high image acquisition rate may be required in dynamic physicochemical experiments that involve the precipitation or deposition of compounds [151]. Cameras are often used due to their flexibility when high magnification and resolution are not required. They may also have an extra objective lens to increase magnification, or be attached with charge coupled devices (CCD) for higher resolutions. In contrast, microscopes are used when there is a need for very high resolution. This is the case when interfacial area between fluids is being analyzed. However, due to the limitation in the optical window of a microscope, saturation of fluids in a large micromodel cannot be determined. Moreover, its low image acquisition rate makes it unable to evaluate dynamic effects.

As a more advanced visualization technique, photoluminescent volumetric imaging (PVI) can be used to acquire high resolution images in 2D or even 3D micromodels. Montemagno and Gray [152] introduced this method for two-phase immiscible flow by doping the wetting phase with fluorophores that partitioned onto fluid-fluid interfaces. In their system, a laser beam excited the fluorophores and thus illuminated the fluid-fluid interface. A CCD camera was used to capture the fluorescent images, which after processing were able to generate a three-dimensional data set. A limitation of this method is that refractive indices of fluids must match with the refractive index of micromodel in order to transmit light and observe fluid flow. Another application of fluorescent microscopy is the micro-particle imaging velocimetry (µ-PIV). In µ-PIV, micrometer-size particles are used as markers in fluid flow to measure instantaneous velocity fields in experimental fluid mechanics. In fact, these particles must emit light when they get de-excited, follow the movement of the fluid, not affect fluid properties and remain in suspension [153]. By using this method, 2D images can be obtained. 3D images can also be obtained if µ-PIV is combined with a confocal microscope. Confocal microscopy is based on the same principal of µ-PIV , being ideal for quasi-static effects when very high resolution is needed [154].

In this work, a complete experimental setup was mounted to perform microfluidic experiments in PDMS micromodels. To visualize fluid flow, a digital camera (Lumix, DMC-GH4, 12-25mm lens) has been used. The decision of using camera rather than microscope was due to the optical window of microscope which could not reach the entire pore-network to observe fluid-saturation changes in the micromodel. Moreover, backlight illumination was provided to enhance the brightness of captured images. The injection apparatus consisted in syringes (BD plastic, 1mL), syringe-pumps (Harvard Apparatus, Pump 11 Elite), and connection lines. Fig. 3.7 shows the experimental setup and a zoom image of the micromodel region during the secondary recovery experiment.

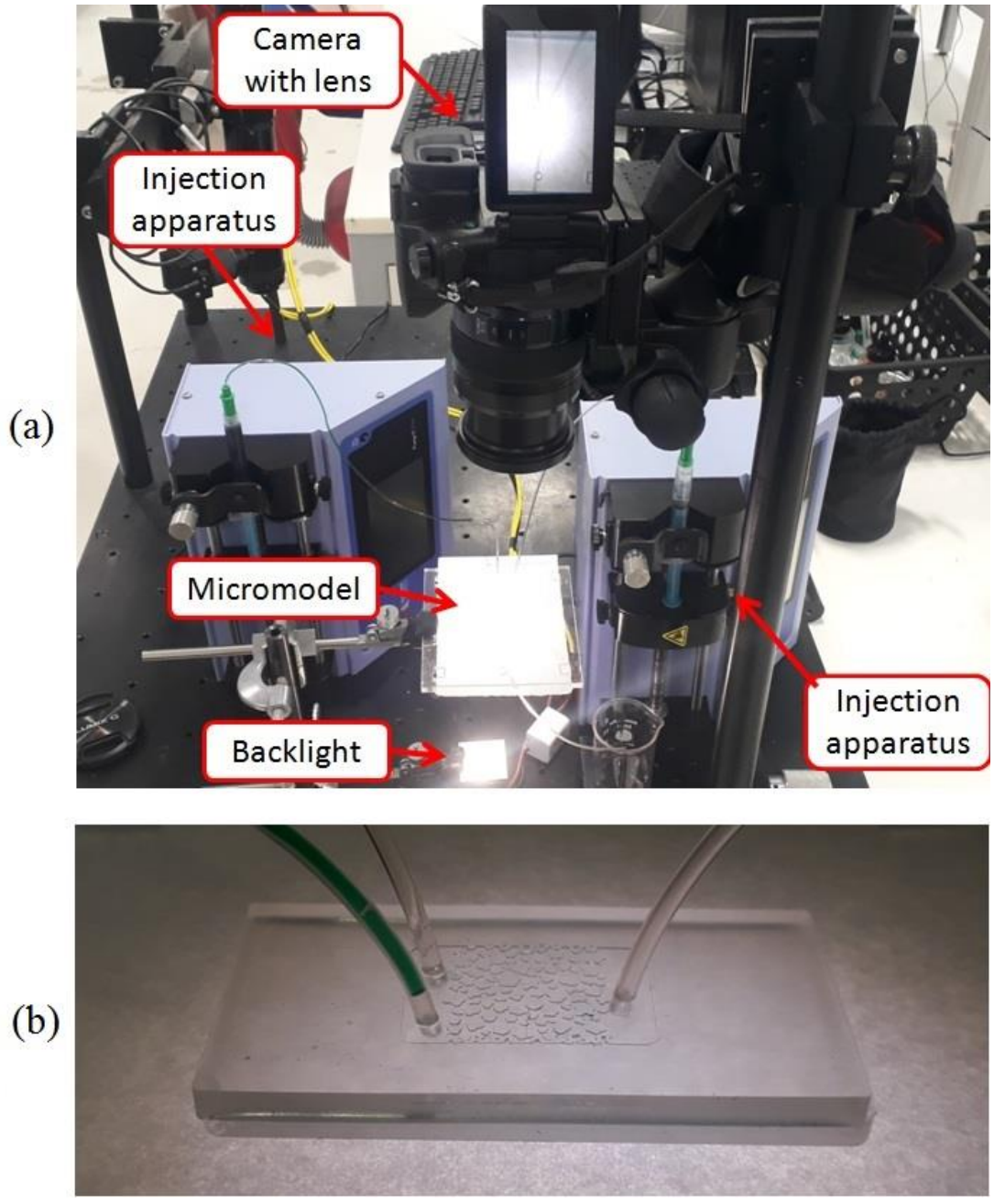

Fig. 3.7 – (a) Designed microfluidic setup. (b) Magnified image of the micromodel region.

Regarding flow tests, experimental methods were designed to simulate two possible options for a real nano-EOR field application [46]. These options were divided in (1) injecting the nanofluid as tertiary recovery after brine flooding; or (2) injecting the nanofluid as secondary recovery. In the tertiary recovery experiment, oil was injected to completely saturate the micromodel, and then consecutively displaced by brine- and nanofluid- flooding as the secondary and tertiary recovery processes, respectively. In the secondary recovery experiment, nanofluid was injected to displace oil in the absence of brine flooding. Both experiments were conducted by initially saturating the micromodel with a colorless mineral oil (Sigma Aldrich, 0.862g/mL density at 25°C, 63.6 – 70.4cP viscosity at 40°C). The brine was synthetically prepared in order to match the ionic composition of the formation brine related to the pre-salt oil used in the IFT and CA measurements. The complete procedure to prepare and characterize the brine was done by the M.Sc. candidate Nathália Dias in LRAP/COPPE/UFRJ. The ionic composition of prepared brine is being shown in Table 3.5. For fluid movement observations, the brine and nanofluid were dyed with a blue dye and yellow dye, respectively. It is important to mention that only a small volume of water soluble dye was used, thus not interfering in the fluids interfacial properties. The equivalent pore volume (PV) of the micromodel was calculated to be 4µL by multiplying the dimensions of the designed pore-network with the designed porosity. A very low injection flow rate of 0.2µL/min was chosen in order to represent the O&G industry conventional value of flow in oil reservoirs of 1ft/day [155]. A SiO_2 nanofluid concentration of 0.1wt.% with biosurfactant was selected for both nano-EOR experiments since it showed the best IFT results. In the tertiary recovery experiment, 4 PVs each of brine and nanofluid were injected, while in the secondary recovery experiment 8 PVs of nanofluid were injected. Images have been captured for both experiments after each subsequent PV injected. Fig. 3.8 shows the flowchart containing the steps described to design the microfluidic setup and the EOR experimental methods.

Table 3.5 – Ionic composition of injected brine.

Ion	Concentration [ppm]	Ion	Concentration [ppm]
Na^+	57,400	Sr^{2+}	716
Ca^{2+}	1,264	Cl^-	103,825
Mg^{2+}	302	Acetate	210
K^+	1,735	Li^+	28
Ba^{2+}	17	Br^-	492

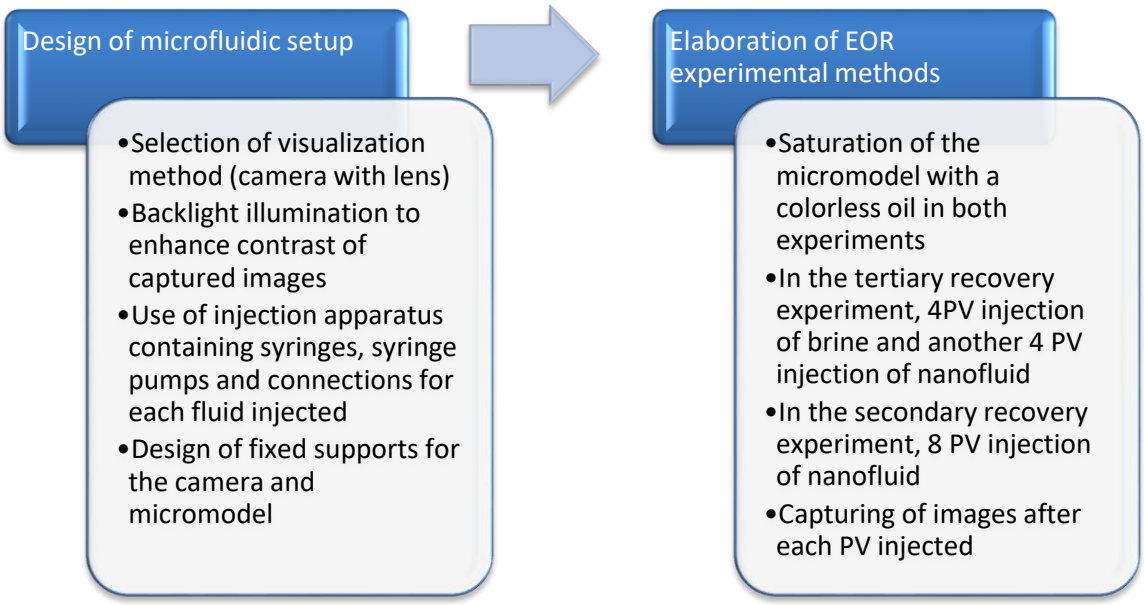

Fig. 3.8 – Flowchart of the steps described to design the microfluidic setup and elaborate the EOR experimental methods.

3.5 Image processing

After acquiring images of fluid flow after each PV injected in both experiments, image processing techniques were required to quantify the recovery factor (RF) along the experiments. These image processing techniques will be explained in details through this section, being divided in the following five steps: (1) *darkening* of the lightest color tones to enhance contrast; (2) *rotation and cropping* of the micromodel to match the designed pore-network area; (3) *stacking* of flow image of each PV with previous images due to air movement; (4) use of *segmentation* to account for the contributions of each fluid to the oil recovery; (5) *coupling* of the segmented image with the designed pore-network image to observe fluid movement between grains.

When visualizing the flow through a micromodel with cameras or microscopes, the natural contrast of the fluid tones may not be sufficient to directly observe fluid/fluid interfaces in captured images. This holds true especially for lighter color tones. In this context, the first step of the image processing consisted in the darkening of the lightest color tones to enhance contrast. This step was done by installing the Adobe Photoshop Lightroom software, which provides several tools for editing and organizing digital images. After installing the program, the captured images were imported and saved. Then, the first image was selected and edited by clicking in the revelation menu. The revelation menu provides dozens of different image treatments, which can also aid

in different problems. To change a specific color tone, the user must scroll down the HSL/Color menu, which contains hue, saturation and luminance bars for eight different color tones. To darken a color tone, the user must set the saturation bar in high and the luminance bar in low. Additionally, the revelation menu provides a series of different filters. Here, it was selected the filter of maximum contrast. Fig. 3.9 shows an example of an original image and a darkened image for the tertiary recover experiment. The yellow color tone represented by the nanofluid was darkened to brown; therefore the visualization of fluids in the micromodel was greatly improved.

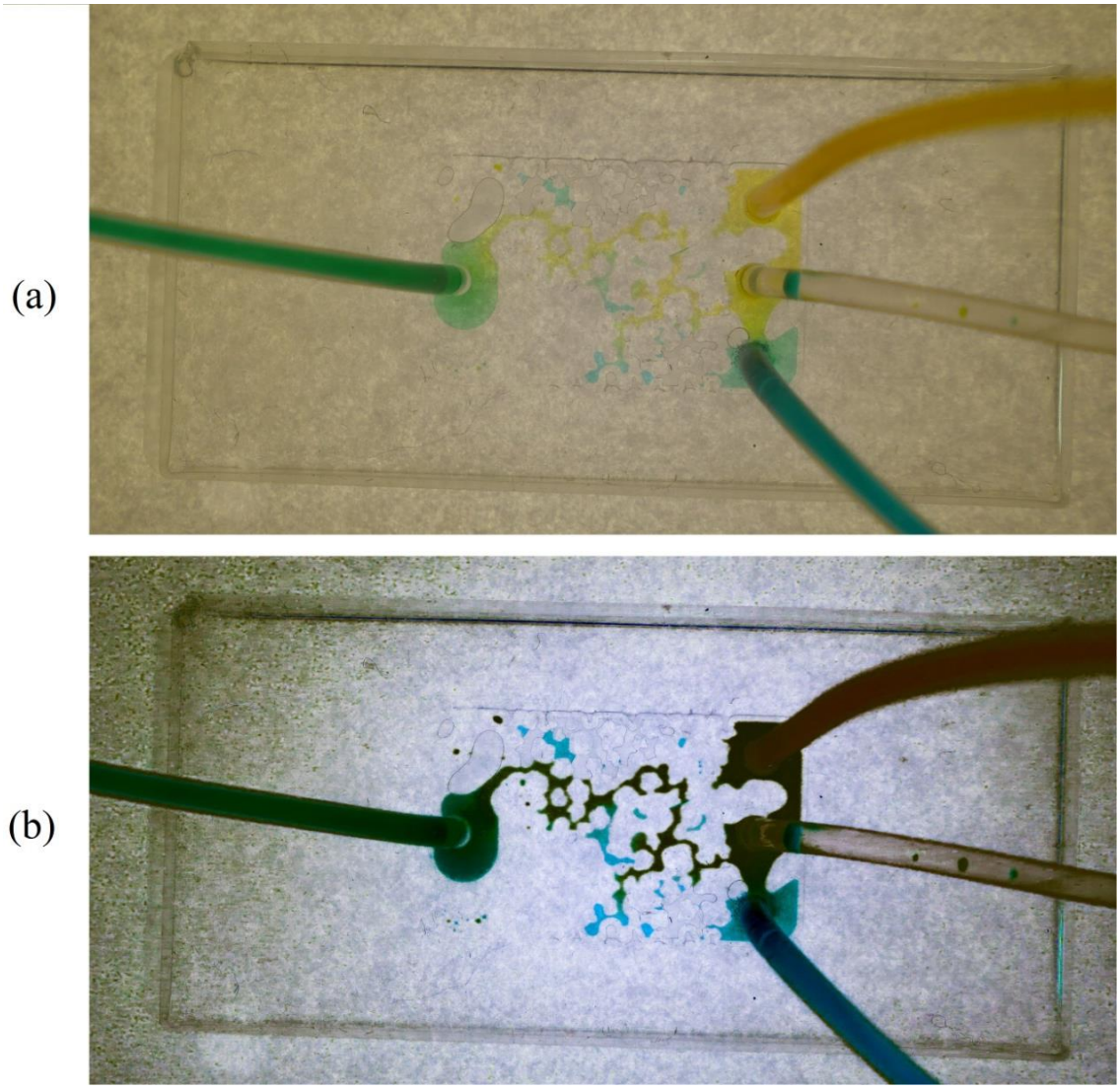

Fig. 3.9 – First step of image processing consisting in the darkening of the lightest color tones to enhance contrast. The image shows examples of (a) original captured image (b) processed image after darkening of the yellow color tone represented by the nanofluid.

After using Adobe Photoshop Lightroom software, all of the following steps to process the captured images will be taken in the ImageJ software. As the second

processing step, image rotation and cropping procedures will be performed in the darkened image. Fig. 3.10 shows the visual images of the steps necessary to rotate and crop images the micromodel images by using ImageJ. In order to rotate an image, first the user has to draw a baseline to obtain the angle that the baseline forms with horizontal. Fig. 3.10(a) shows the upper end of the micromodel as the baseline for rotation, since this line is parallel to the upper end of the pore-network. When the line is drawn, the angle with horizontal is directly shown. To rotate the image according to this angle, the user has to click on the Image toolbar, then transform and rotate. After setting the angle, the micromodel in the image becomes horizontal (Fig. 3.10(b)). As the other step, the rotated image has to be cropped as exactly as possible to the designed pore-network. To perform this, a vertical line is draw from the upper to bottom edges of the pore-network. This scale line is intended to have in pixels the vertical dimension of the pore-network in millimeters (Fig. 3.10(c)). Thus, to convert the scale from pixels to millimeters, the user has to click on the Analyze toolbar and then in set scale. Now, it is possible to draw a square having the same dimensions in millimeters as the predicted from the design of the pore-network (Fig. 3.10(d)). This square will be used to crop the image according to the pore-network. However, it is not possible to directly visualize the location of the pore-network according to the image. In fact, some features in the designed pore-network have to be used as references to guide the precise location of the pore-network. Fig. 3.10(e) shows the cropped image by using a specific grain as a reference to the designed pore-network (Fig. 3.10(f)). Despite seemed to be difficult at first sight, this rotation and cropping step becomes easier as the previous images are processed, being also used as references to crop the pore-network. Moreover, an error in one cropped imaged will be observed when performing further processing steps.

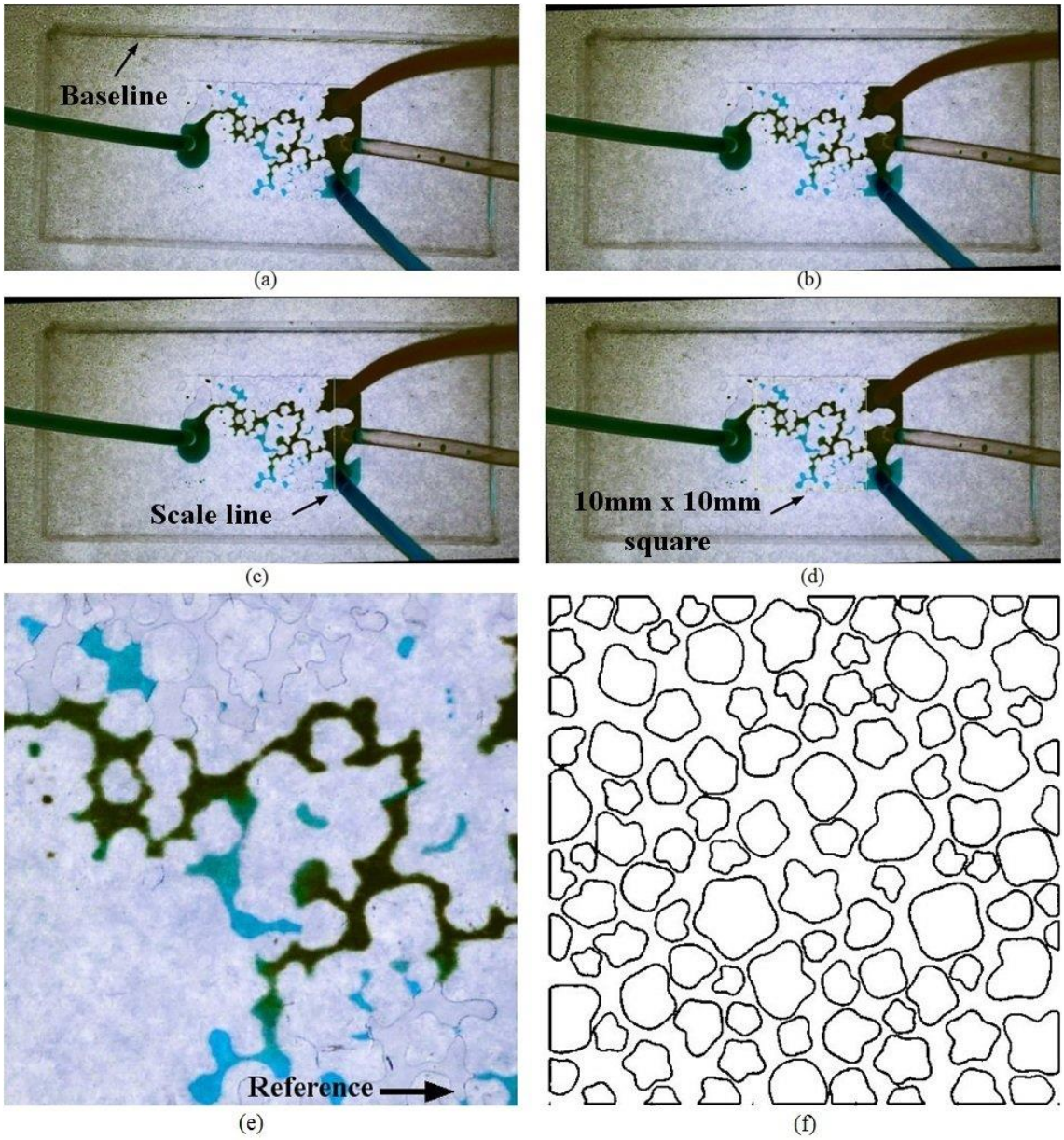

Fig. 3.10 – Rotation and cropping processing step. (a) darkened image with a baseline drawn for rotation. (b) rotated imaged. (c) vertical line drawn to be used as a scale line to convert pixels in millimeters. (d) square drawn in the exactly dimensions predicted from the designed pore-network. (e) cropped image using as a grain as reference. (f) designed pore-network image to be used as reference.

The presence of air inside the micromodel is a constant issue that persisted in all microfluidic experiments performed. Several attempts have been performed to mitigate this effect. The changes in the design of the CAD templates of the micromodels were made to avoid air entrapment. To start any flow experiment, the air inside the micromodels has to be fully removed. However, some air seemed to appear and migrate from the lateral edges to the center of the pore-network as the experiment progressed. In

fact, this air-invasion effect was even more considerable due to the long duration of the EOR experiment, which injected 8 PVs of fluids in a very low flow rate for several hours. Then, a strategy used was to combine the flow images in which air was more present to previous images which air had not been appeared. This combination was done by performing a stacking step in ImageJ. In order to stack images, the user has to open the images to be combined, click on the Image toolbar, then stack and images to stack. The resulting stack has to be converted in a 8-bit image by clicking in the Image toolbar, type and 8-bit. After that, the 8-bit image is converted into a RGB image by also clicking in the image toolbar, then color and stack to RGB. Fig. 3.11 shows an example of the image stacking process. In Fig. 3.11(a), a cropped image of nanofluid is being shown with some air regions denoted by green and red areas. By observing the image, the user would consider these air regions were not originally displaced by the injected fluid. However, Fig. 3.11(b) shows that during the green areas were in fact originally oil displaced by brine flooding, whether red areas were basically air invasion during the experiment. The stacking combination of images offers the required tool to identify air movement and injected fluid movement. Fig. 3.11(c) shows the stacking results of the two images. It can be seen that the green areas representing the air that was previously injected fluid are now colored. On the other hand, the red areas that must not be considered remain colorless. By doing the stacking process, the recovery factor after each PV injected can be more precisely calculated.

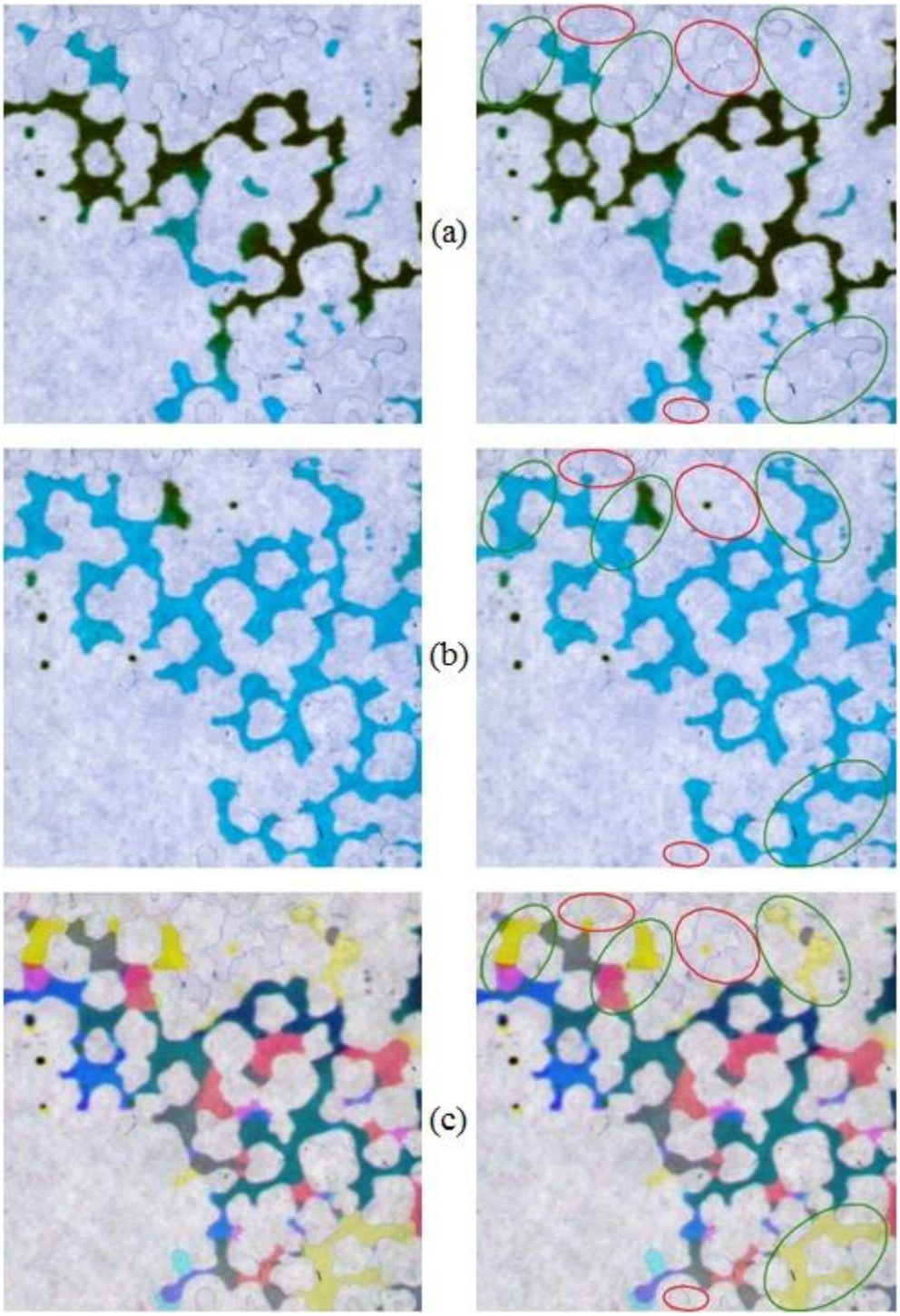

Fig. 3.11 – Example of the image stacking process. (a) Image of nanofluid flooding containing green and red areas representing air. (b) A previous image of brine flooding in the same experiment. It can be seen that the green areas consisted of injected fluid, while red areas were only air movement. (c) Stacked combination of the two images. The green areas that should be accounted for oil recovery are now colored, while the red areas that have to be neglected are colorless.

After stacking the images, it is now possible to account for the contribution of each fluid to the oil recovery. To perform this step, a segmentation process in the stacked images is necessary. This step was done by installing a plug-in in ImageJ software called Trainable Weka Segmentation. As a brief explanation, the Weka plug-in combines a collection of machine learning algorithms with a set of selected image features to produce pixel-based segmentations. Therefore, it is possible to combine the contributions of each fluid injected to oil recovery, and also discard any fluid that must not be accounted (for example, entraining air during experiments). To use the Weka plug-in, the user has to click on the plugins toolbar, then segmentation and Trainable Weka Segmentation. After that, the user has to select the color tones that will be accounted for segmentation. Fig. 3.12 shows the segmentation step on the stacked image and its results. It can be seen that the segmented image almost match the stacked image. Additionally, it is also possible to calculate the fraction of the resulting image that is covered by the segmented color, or in this case, injected fluid. This step is done by clicking in the analyze toolbar, and then in measure. If the area of injected fluid is not directly informed, the user has to click on results, options, set measurements, and select the area fraction option. Moreover, if the ImageJ software is left open after each segmentation and area fraction calculation, the resulting area percentages for each image will be informed, although it is important to manually note the area percentages.

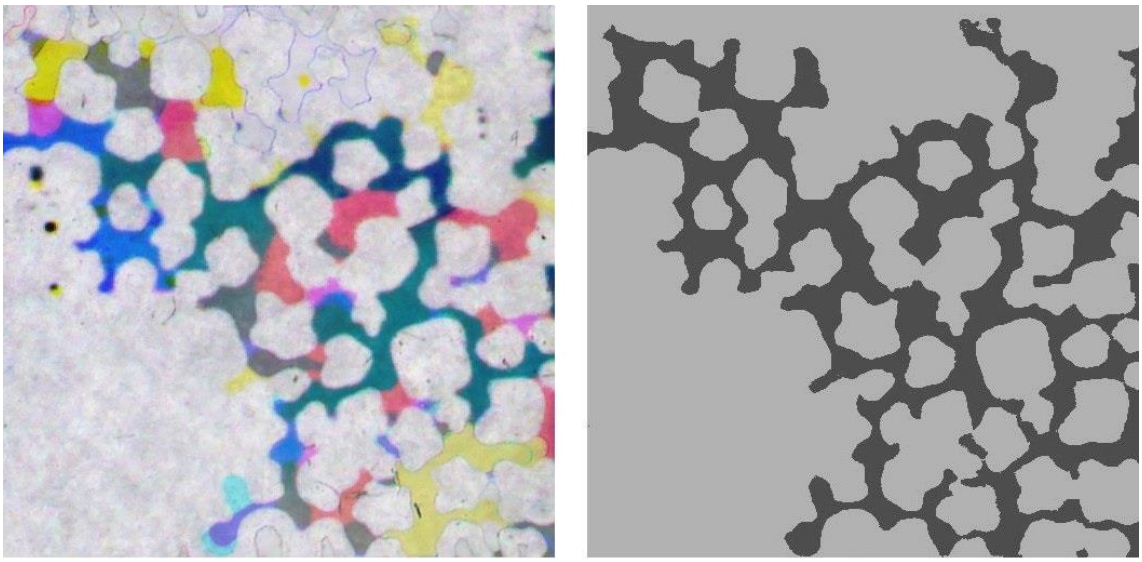

Fig. 3.12 – Segmentation processing step performed on (a) stacked image and (b) resulting image after segmentation.

In order to better observe the fluid invasion along the pore-network, the segmented image has to be coupled with the original pore-network image containing the grains. Fig. 3.13 shows the steps required to exactly couple the images. First, the pore-space of the original generated image (Fig. 3.13(a)) is filled with black color (Fig. 3.13(b)). In fact, any color might be used, but black was chosen in order to represent oil. Then, the black-filled image is stacked with the segmented image by doing the stacking process previously described. The stacked image must be converted to 8-bit, then converted again to RGB. The final coupled is then obtained (Fig.3.13(d)), showing the injected fluid in red, oil in black and grains in green. Fig. 3.14 contains a flowchart to summarize the five steps of the complete image processing procedure.

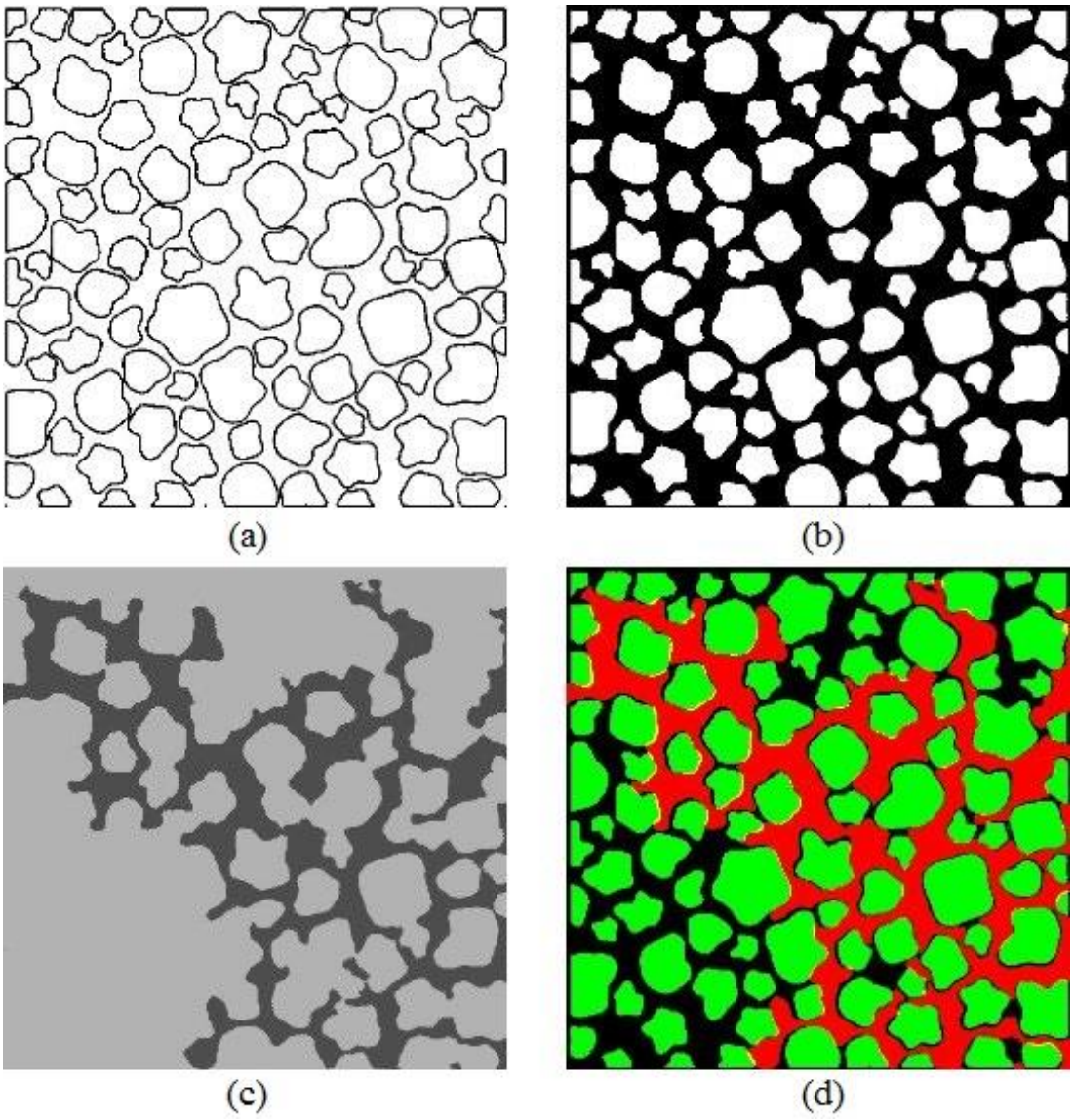

Fig. 3.13 – Coupling step on the segmented image. (a) original generated binary image. (b) binary image after filling the pore-space with black color. (c) segmented image. (d) coupled final image showing the injected fluid in red, grains in green and oil in black.

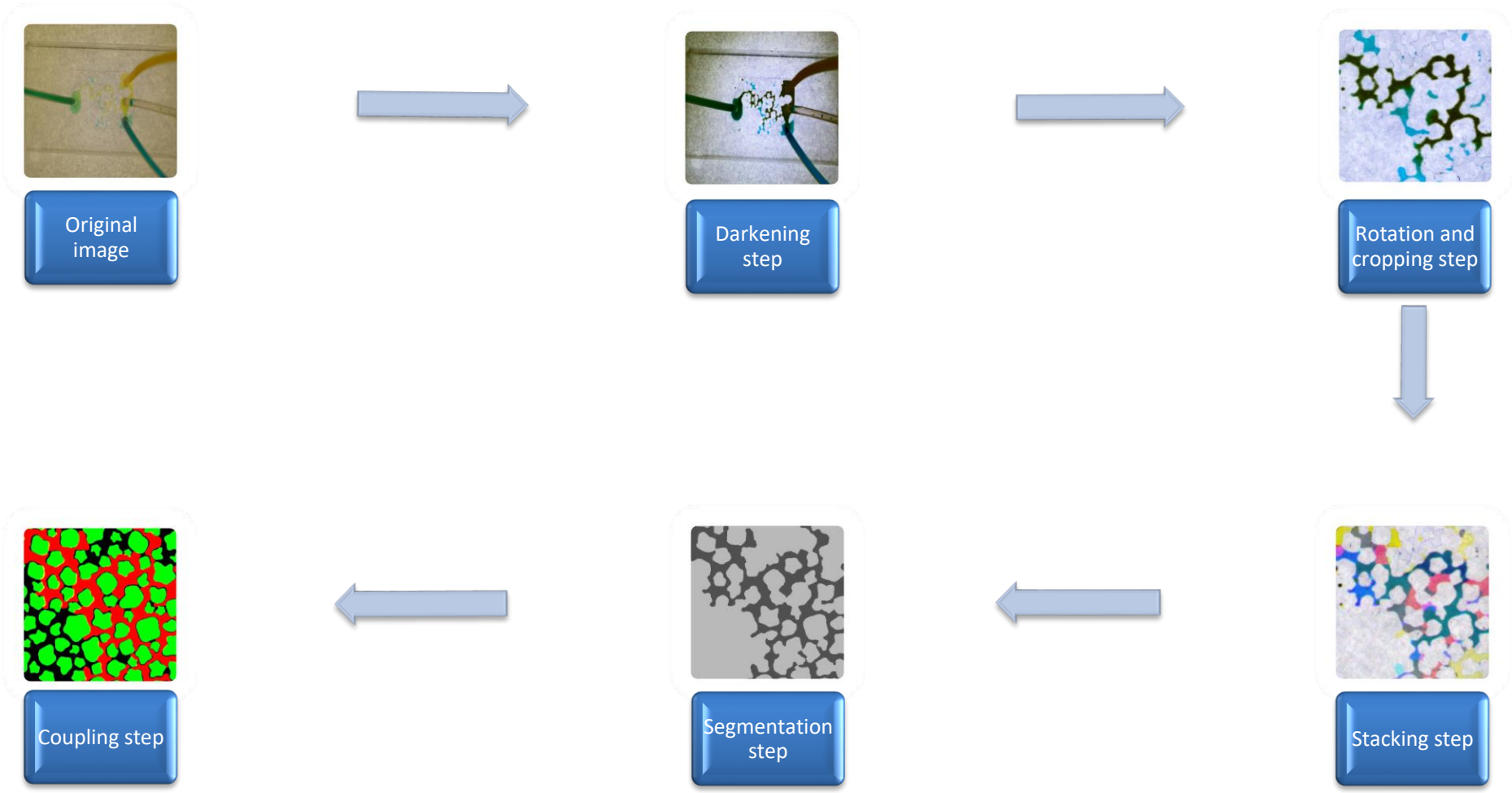

Fig. 3.14 – Flowchart containing the five steps described to perform the complete image processing procedure on captured images.

4 RESULTS AND DISCUSSION

Here, the results obtained by the methods previously introduced will be presented. First, several different generated pore-networks with various sorting levels and degrees of grain deformation will be shown, discussing aspects related to the similarity to real-rocks. After that, the designed CAD templates containing a generated pore-network will be presented, and topics related to the fabrication of the replica molding (REM) will be discussed. Moreover, the dimensional characterization of micromodels will be reported. Then, the SiO_2 nanofluids characterization results will be presented and discussed. IFT results and contact angle analysis will also be performed and their results will be discussed based on the literature. EOR flow experiments were carried out and the comparison between tertiary nanofluid flooding and secondary nanofluid flooding will be done, discussing the results based on the IFT and CA experiments.

4.1 Pore-networks

By the means of the adapted algorithm, several different pore-networks with different sorting levels and degrees of grain deformation were generated. A 10mm x 10mm square domain was chosen since higher domains would require several days for performing the EOR experiments. On the other hand, smaller domains might not have the sufficient number of grains to vary sorting and represent a porous medium. In order to represent a sandstone porous medium Table 2.1, the four grain-size classes of sandstones must be selected, ranging from fine sand (minimum diameter of 0.1mm) to huge sand (maximum diameter of 2mm). Therefore, for each generation, the minimum and maximum grain radii were kept constant and equal to 0.05mm and 1.0mm, respectively. The mean grain radius was also constant and equal to the average value of the distribution, thus 0.525mm. A minimum distance between grains of 50 micrometers was set, which is equivalent to capillary pores in conventional sandstones [84]. The standard deviations of the grain-size distributions were altered for each sorting level. The degree of deformation of grain was also altered for each simulation in order to represent the various grain-shapes existing within real-rocks. The estimated porosity for each sorting level was set according to Table 2.2. It is important to remember that this estimated porosity is slightly lower than the final porosity. Table 4.1 shows the list of inputs parameters and output parameters to generate the pore-networks with different sorting levels and degrees of deformation. Fig. 4.1, Fig. 4.2 and Fig. 4.3 shows computer generated pore-networks and grain-size distributions for well-, moderately-

and poorly-sorted rocks in various degrees of grain deformation. It can be seen that the general form of the grain-size distributions remains similar as grain deformation changes. However, a positive skewness appears when the sorting level changes from well-sorted to poorly-sorted. This tendency is represented by the increase in the number of fine grains in poorly-sorted rocks that are inserted in order to fill the pore-space and decrease the porosity. Moreover, a slight difference between the generated and input main grain radius may appear due to the removal of grains in the domain boundaries.

Table 4.1 – List of inputs parameters and output parameters to generate the pore-networks with different sorting levels and degrees of deformation.

Sorting Level	Input parameters										Output parameters		
	rMin [mm]	rMax [mm]	rMean [mm]	rStd	degree	numPoints	blobWidth	min Dist [mm]	porEst	domPoints	porFin	numGrains	σFolk
Well	0.05	1.00	0.525	0.15	1	100	7	0.05	0.35	50000	0.42	74	0.36
Well	0.05	1.00	0.525	0.15	3	100	7	0.05	0.35	50000	0.39	85	0.42
Well	0.05	1.00	0.525	0.15	5	100	7	0.05	0.35	50000	0.40	100	0.37
Moderately	0.05	1.00	0.525	0.35	1	100	7	0.05	0.30	50000	0.36	97	0.72
Moderately	0.05	1.00	0.525	0.35	3	100	7	0.05	0.30	50000	0.36	101	0.79
Moderately	0.05	1.00	0.525	0.35	5	100	7	0.05	0.30	50000	0.36	109	0.77
Poorly	0.05	1.00	0.525	2	1	100	7	0.05	0.22	50000	0.32	186	1.30
Poorly	0.05	1.00	0.525	2	3	100	7	0.05	0.22	50000	0.28	244	1.30
Poorly	0.05	1.00	0.525	2	5	100	7	0.05	0.22	50000	0.29	217	1.32

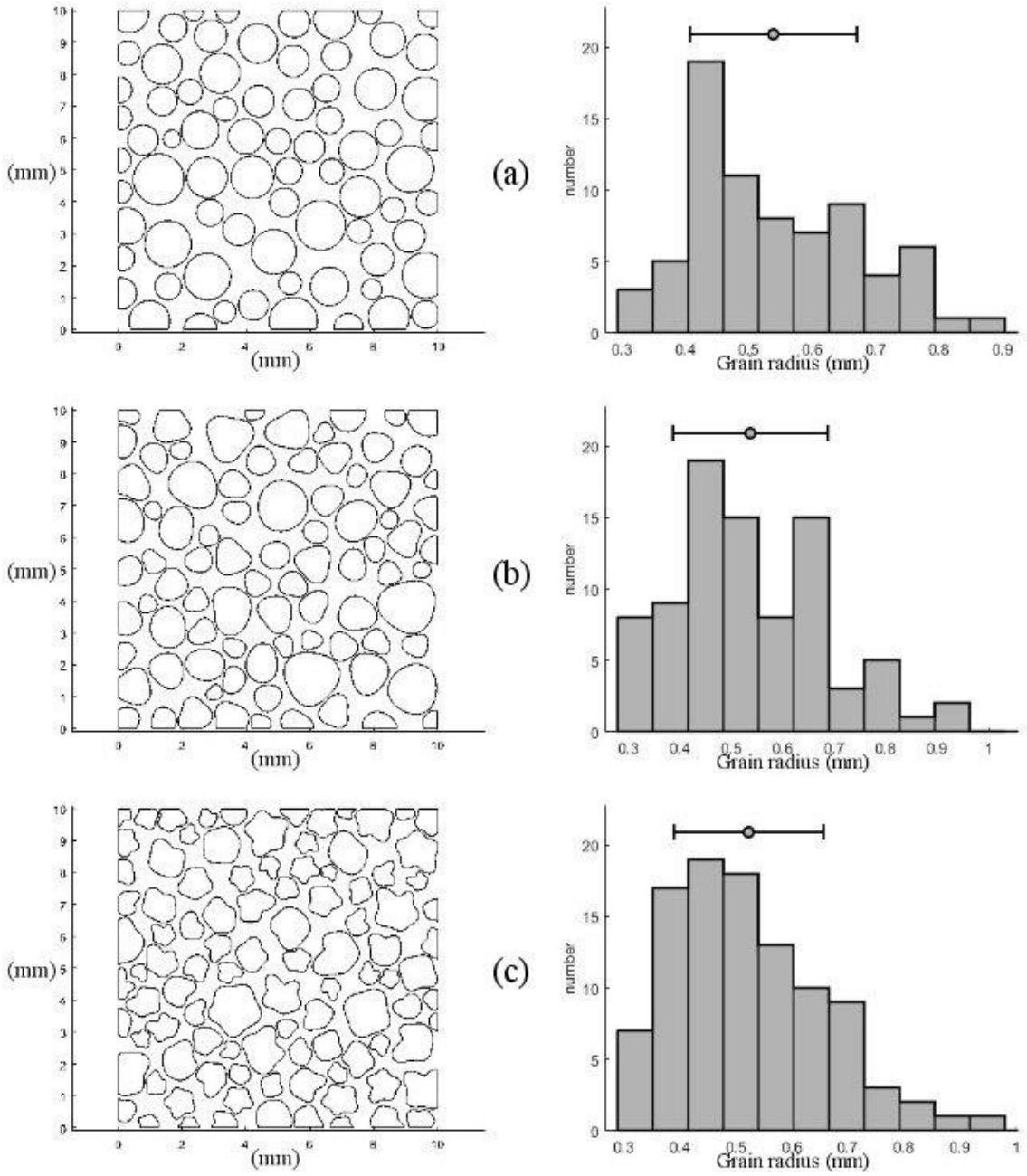

Fig. 4.1 – Computer generated pore-networks and grain-size distributions for a well-sorted rock in various degrees of grain deformation. (a) rounded grains represented by degree 1, (b) slightly deformed grains represented by degree 3, (c) highly deformed grains represented by degree 5. Regarding the grain-size distributions, the mean grain radius and standard deviations are also being represented by the upper box-plots.

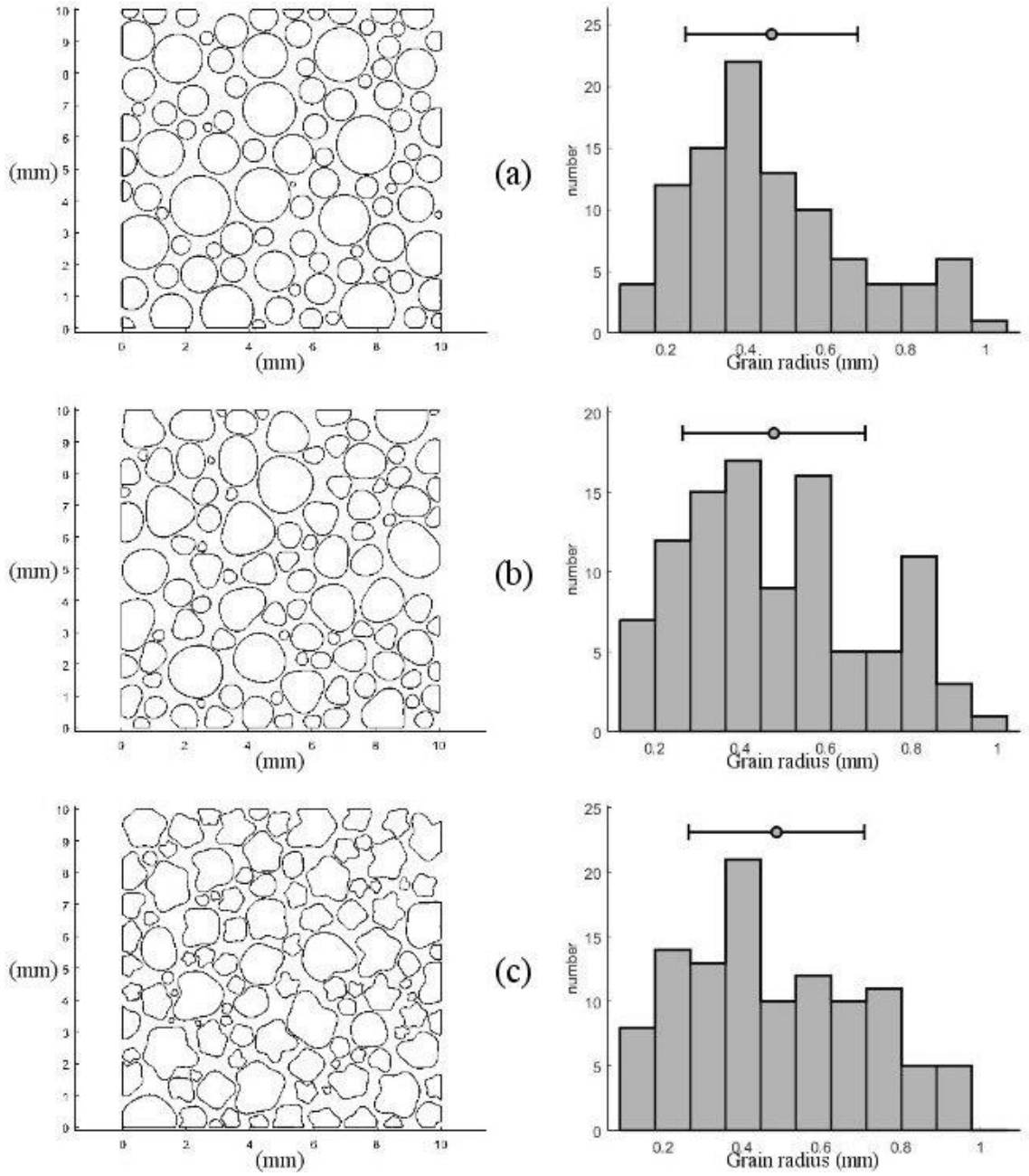

Fig. 4.2 – Computer generated pore-networks and grain-size distributions for a moderately-sorted rock in various degrees of grain deformation. (a) rounded grains represented by degree 1, (b) slightly deformed grains represented by degree 3, (c) highly deformed grains represented by degree 5. Regarding the grain-size distributions, the mean grain radius and standard deviations are also being represented by the upper box-plots.

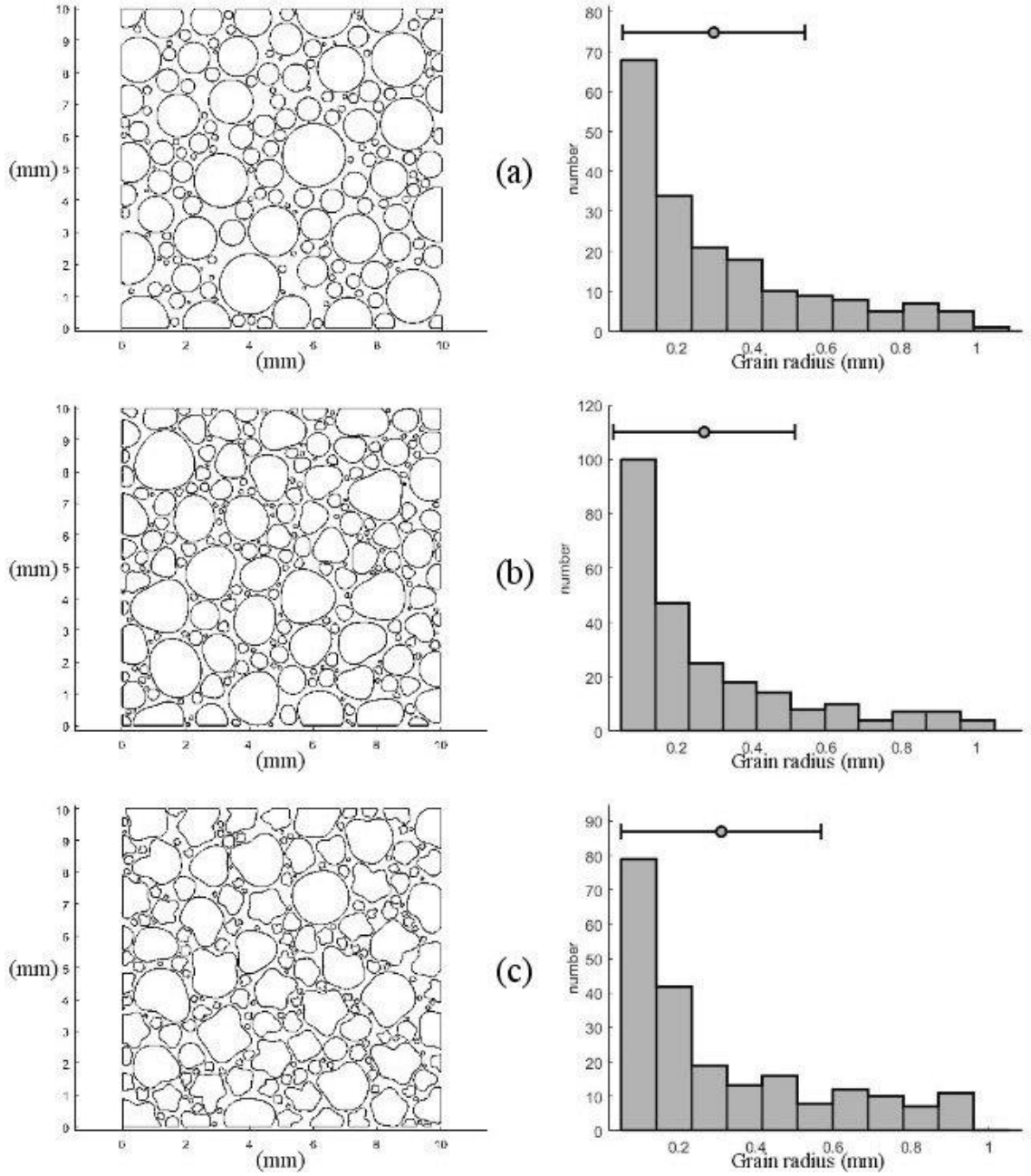

Fig. 4.3 – Computer generated pore-networks and grain-size distributions for a poorly-sorted rock in various degrees of grain deformation. (a) rounded grains represented by degree 1, (b) slightly deformed grains represented by degree 3, (c) highly deformed grains represented by degree 5. Regarding the grain-size distributions, the mean grain radius and standard deviations are also being represented by the upper box-plots.

4.2 Micromodels

After generating the pore-networks in different sorting levels and degrees of grain deformation, one pore-network was selected to be fabricated into a micromodel. The choice of which network would be fabricated as a function of the time that would be expended during the fabrications. Since poorly-sorted and moderately-sorted

networks had a higher number of inserted grains (Table 4.1), the pore-network selected was the well-sorted containing highly deformed grains (Fig. 4.4).

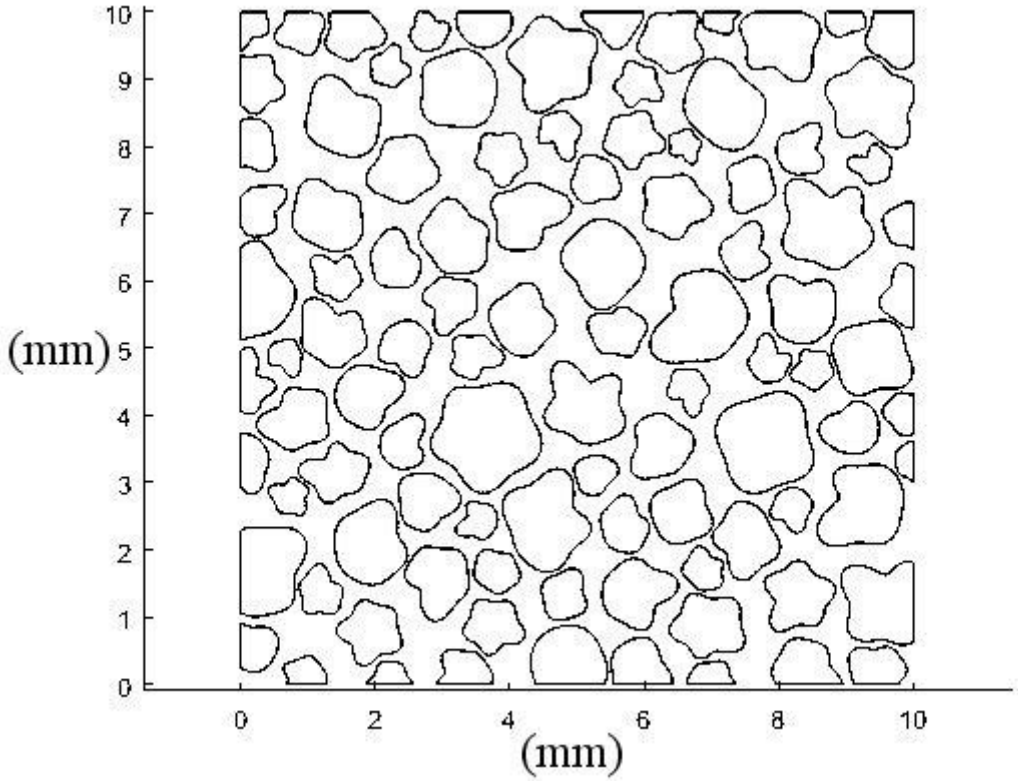

Fig. 4.4 – Selected pore-network to be fabricated containing a well-sorted level and highly deformed grains (degree 5).

As the pore-network was selected, it was inserted in designed CAD templates in order to be fabricated. In this context, three different CAD templates were designed (Fig. 4.5). The arrows are representing the entries for injected fluids. Template (a) consisted of one entry and one exit, eight inlet/outlet channels of equal width (0.4mm), and a wide region of 1.5mm length adjacent to the pore-network. Template (b) consisted of three entries and one exit (0.4mm width), with no inlet/outlet channels. The addition of two entries in this template was due to the consecutive injection of three fluids during EOR experiments. Moreover, it has been seen that the presence of the eight inlet/outlet channels in template (a) had no effect on the flow profile, since some channels were blocked by entrained air during flow experiments. Finally, in template (c), the connection lines were inserted directly into the wide region adjacent to the pore-network, which had its width slightly enlarged to 3.5mm. Flow experiments have shown that this template was the one that best performed, allowing injected fluids to enter the pore-network uniformly and hindering the presence and migration of entrained air.

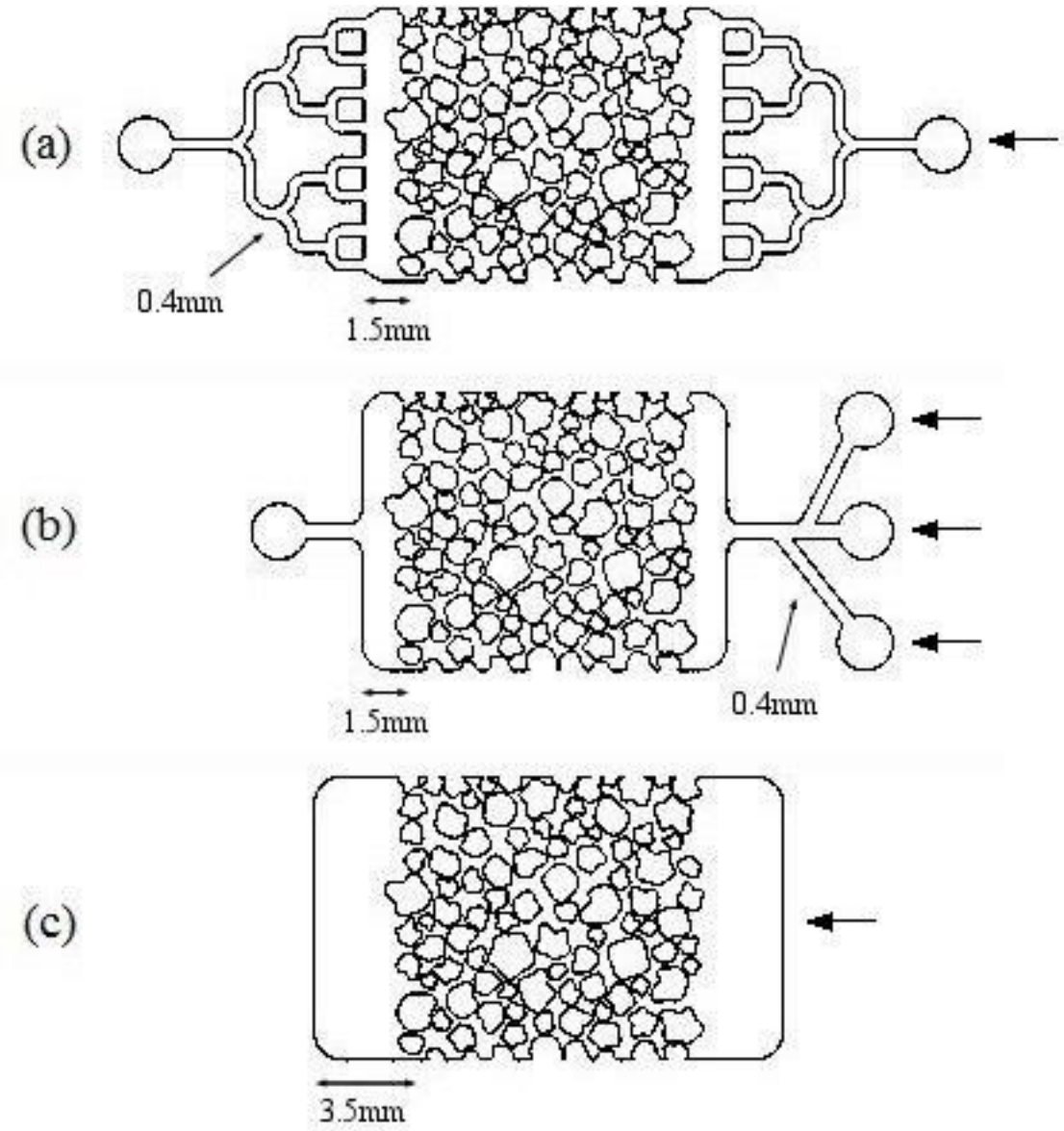

Fig. 4.5 – Three different templates designed with a well-sorted generated porous-network. Template (a) consists of eight inlet/outlet channels of 0.4mm constant width, and an entrance region of 1.5mm length. Template (b) consists of three entries and one exit of 0.4mm width, with no inlet/outlet channels. Template (c) consists only of a wide entrance region of 4mm length. Flow experiments have shown that this template was the one that best performed, allowing injected fluids to enter the pore-network uniformly and hindering the presence and migration of entrained air.

As the CAD template to be fabricated was selected, a computer process was applied to convert the CAD file into a programming G code to be read by the CNC machine. To micro mill onto the acrylic mold, four different procedures with different microtools were performed (Table 4.2). The first procedure consisted in leveling the mold with a 3000μm diameter microtool, cut velocity of 320mm/min, 8000rpm speed

rotation and 5 steps of 0.5mm. The second procedure was the refining of the mold with a 500μm diameter microtool, cut velocity of 480mm/min, 24000rpm speed rotation and 1 step of 0.11mm. The third procedure was the facing of the channels surface with a 200μm diameter microtool, cut velocity of 584mm/min, 54000rpm speed rotation and 1 step of 0.01mm. At last, a pore milling procedure was applied with a 200μm diameter microtool, cut velocity of 584mm/min, 54000rpm speed rotation and 4 steps of 0.025mm. Fig. 4.6 shows the fabricated replica mold of the template (c) with scale bar.

Table 4.2 – Parameters of the micromilling process to fabricate the replica molding (REM).

Milling procedure	Microtool diameter [μm]	Cut velocity [mm/min]	Number of steps	Speed rotation [rpm]
Leveling	3000	320	5	8000
Refining	500	480	1	24000
Channel facing	200	584	1	54000
Pore milling	200	584	4	54000

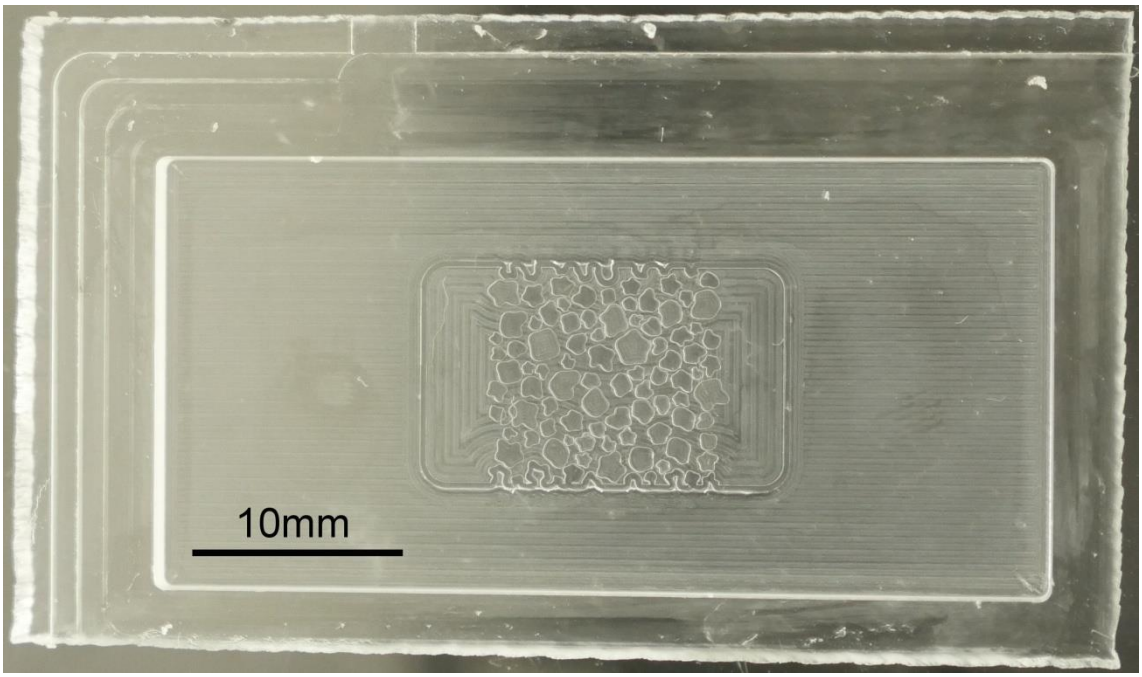

Fig. 4.6 – Fabricated replica mold of the template (c) containing a generated well-sorted pore-network with highly deformed grains. Scale bar is being represented in the image.

After fabricating the REM, several micromodels were manufactured to perform flow experiments. In this context, is of great importance to characterize the dimensional features of the micromodel in order to evaluate the resemblance to the designed CAD template. The complete procedure to characterize the micromodel was performed in LabMEMS/COPPE/UFRJ, by the collaboration of the M.Sc. candidate Ingrid Curcino and D.Sc. candidate Raquel Fedrizzi. In this context, 2D and 3D microscopic images have been taken

(Hirox RH-2000) to characterize the micromodel pore-network. In this procedure, four regions were selected from the four corners of the pore-network (Fig. 4.7) and the distance between grains and inner grain dimensions were compared to the predicted from the CAD template. Fig. 4.8 and Fig. 4.9 show micromodel microscope images and CAD images for the selected region in the upper left corner. By comparing the images, it can be seen that the distances slightly differ, although the exact location of the lines might be different. Fig. 4.10 shows a 3D microscope image of the micromodel in order to characterize the height of the grains. It can be observed that, in this region, the height of the manufactured micromodel is almost equal to the height of the designed CAD template, being equivalent to 102μm and 100μm, respectively. The appendix A contains additional 2D and 3D images for the other selected regions in order to characterize the micromodel. (Fig. A.1 to Fig. A.9). In these images, it can also be seen that the distances between grains and the distances within grains are slightly different, although the 3D microscope images shows that the height of the micromodel in these regions is almost equal to the height of the designed CAD template.

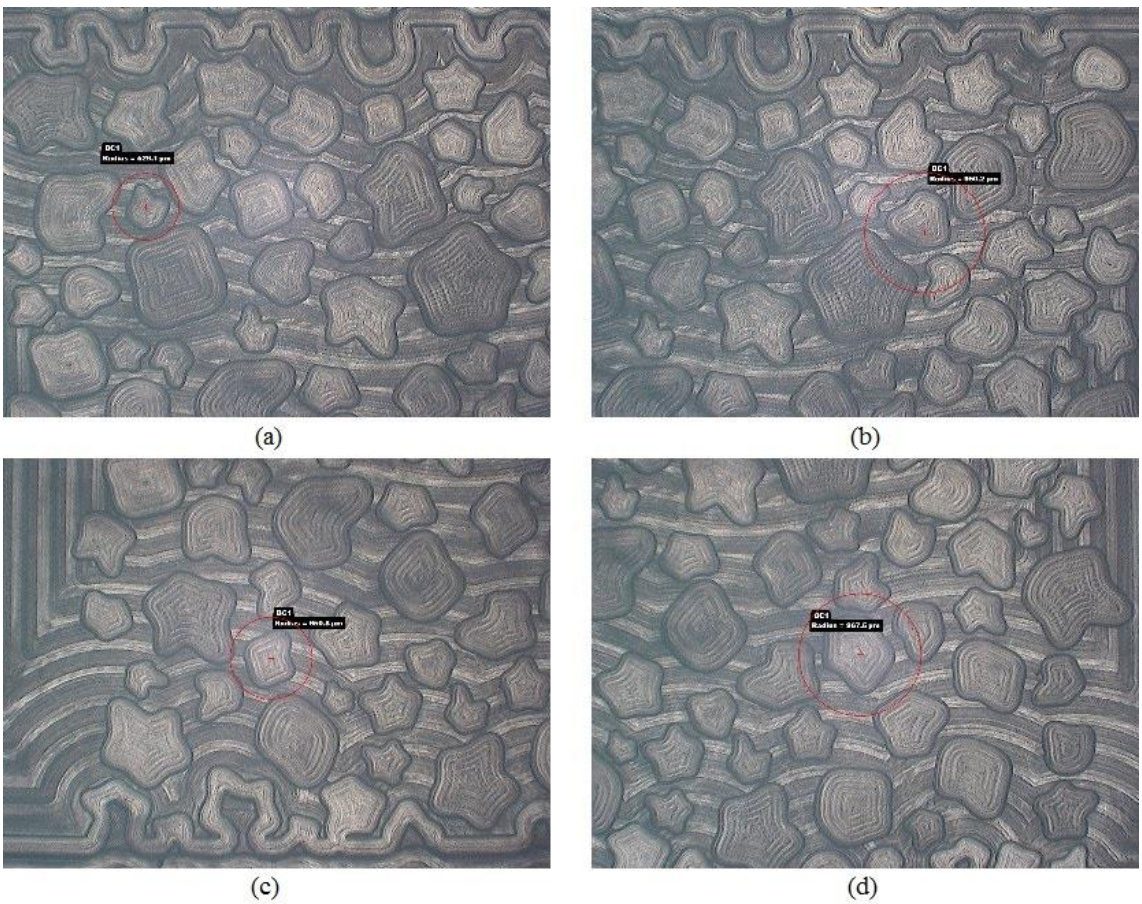

Fig. 4.7 – Microscopic images of micromodel containing the four corners of the pore-network and selected regions to be dimensionally characterized. (a) upper left corner, (b) upper right corner, (c) bottom left corner, (d) bottom right corner.

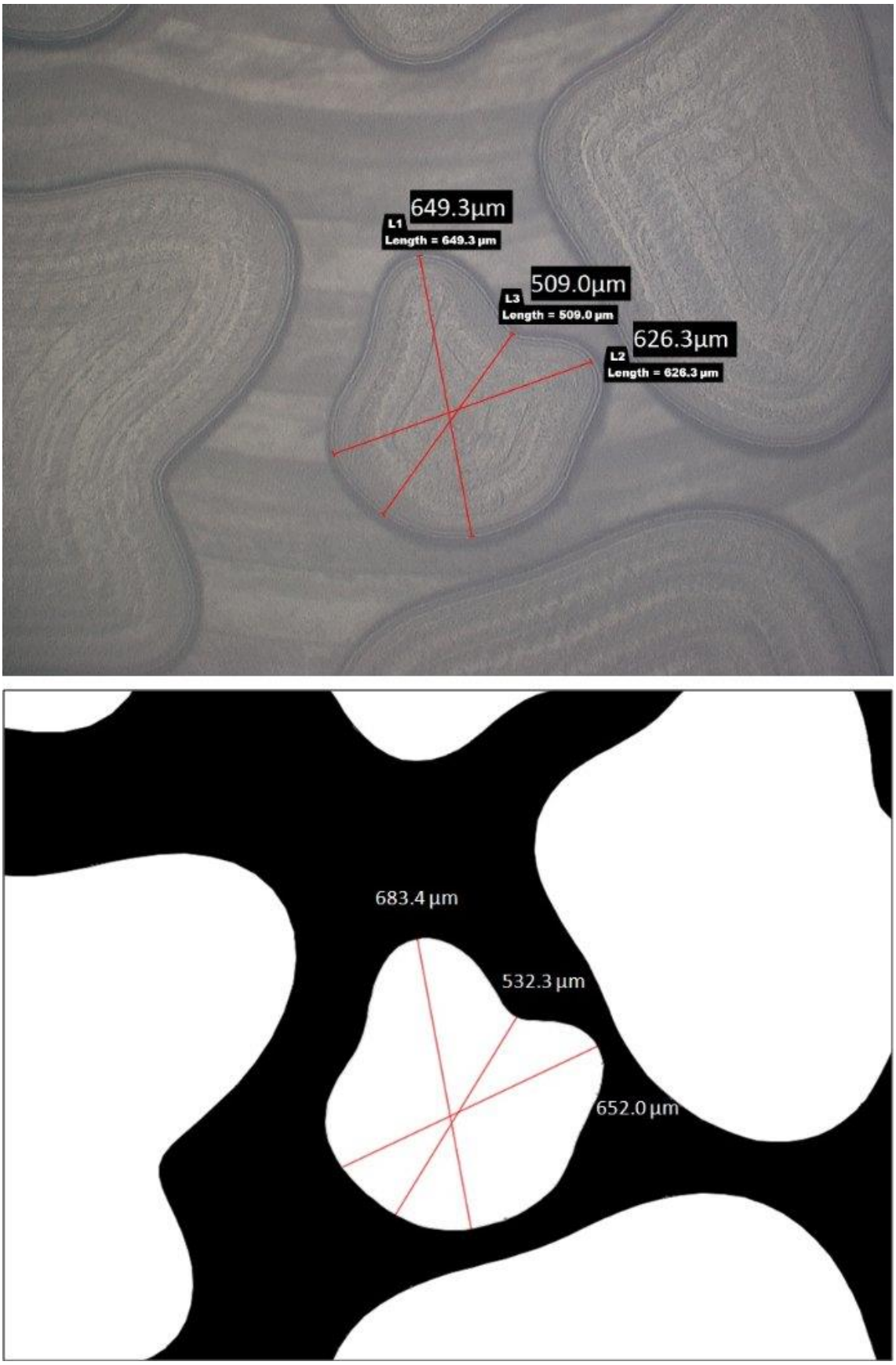

Fig. 4.8 – Micromodel microscope image and CAD image of the selected region in the upper left corner showing the inner dimensions of the grain.

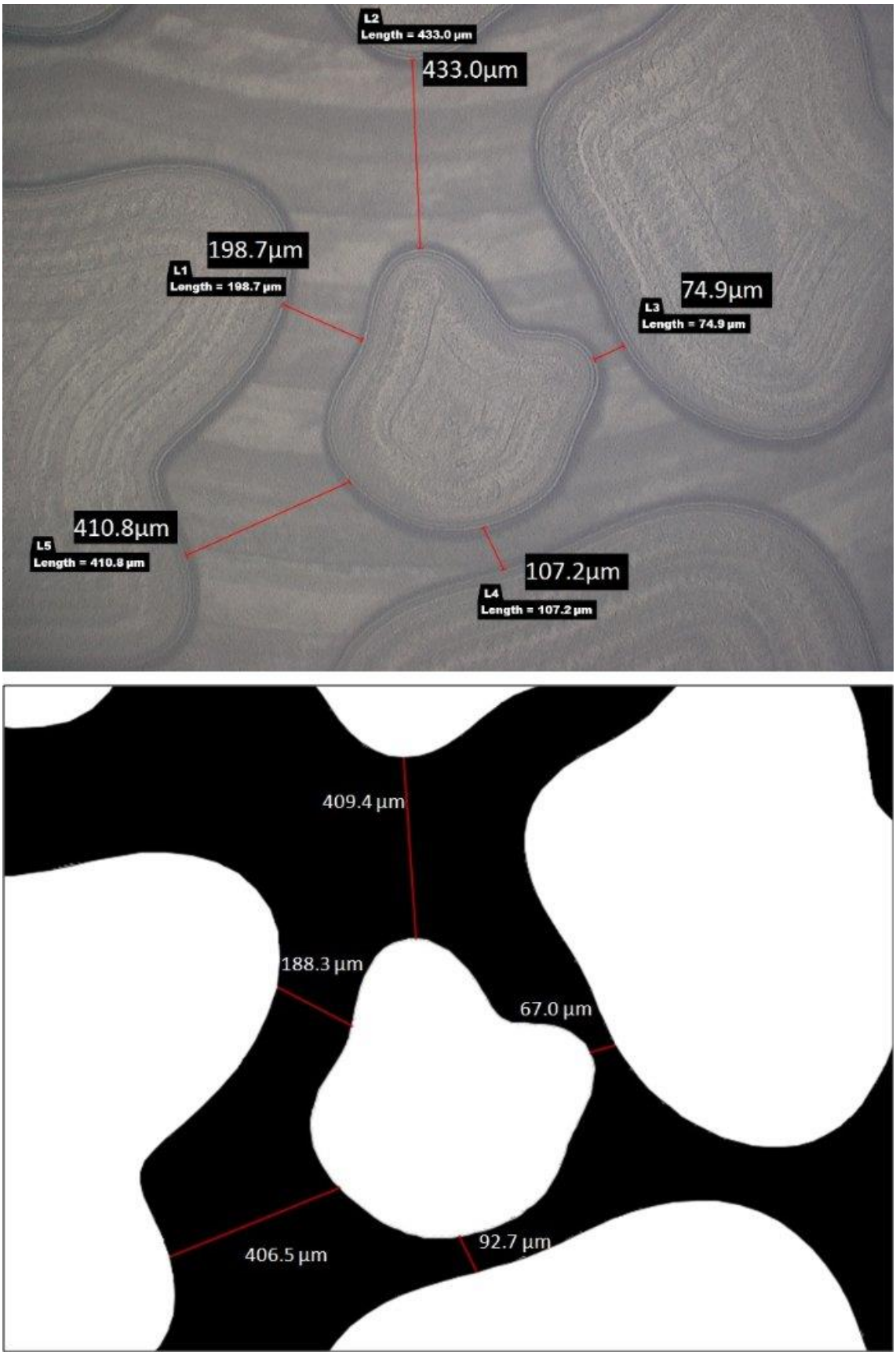

Fig. 4.9 – Micromodel microscope image and CAD image of the selected region in the upper left corner showing the pore dimensions between adjacent grains.

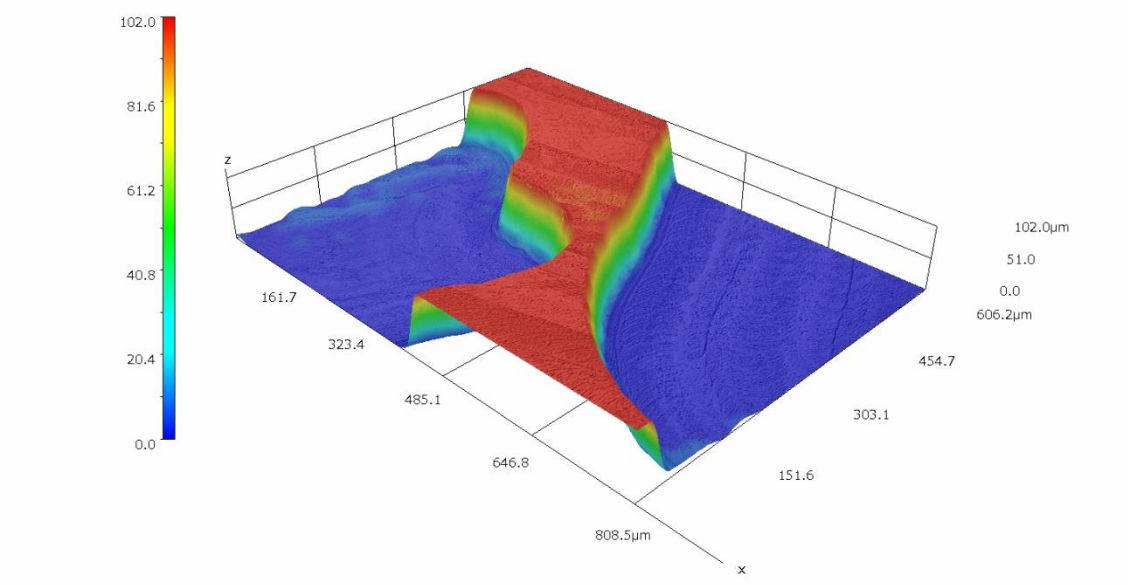

Fig. 4.10 – Micromodel 3D microscope image of the selected region in the upper left corner. Two adjacent grains are being represented in blue, while the pore space is represented in red. The scale bar is in micrometers. The image shows that the fabricated height of the micromodel (102µm) in this region is almost equal to the designed height (100µm).

4.3 Nanofluids characterization

The first step to characterize the prepared SiO_2 nanofluids was to measure their density for the varied concentrations. The densities of the nanofluid dispersions were measured by using a densitometer (DMA 4500, Anton Paar, LRAP/COPPE/UFRJ) at 25°C. Table 4.3 shows the measured density values for each of the concentrations prepared. It can be seen that the densities of the nanofluids are practically constant with silica concentration, being approximately equal to the density of the base fluid. This behavior was expected since silica NPs have low density and were prepared in low concentrations. As an important parameter in EOR, the dynamic viscosity of an injected fluid has also to be considered. As reported by the literature, SiO_2 nanofluids possess little effect on viscosity (Table 2.4). For example, Rostami *et al.*[48] reported that a 0.2 wt.% SiO_2 NP concentration in distilled water has a 1.0002cp dynamic viscosity, being almost equal to the viscosity of fresh water. As the NP concentration increases to 1 wt.%, the dynamic viscosity of the nanofluid increases to 1.4cp [44]. In fact, Barkhordari and Jafari [65] evaluated the dynamic viscosity of silica nanofluids in distilled water for higher NP concentrations. They reported that a 3 wt.% and 5 wt.% NP concentration would increase the viscosities of the nanofluids to 2.4cp and 3.9cp, respectively.

Table 4.3 – Densities of prepared SiO_2 nanofluids in ultrapure water at 25°C.

Nanofluid concentration [wt.%]	Density at 25 °C [g/cm^3]
0	0.9980 ± 0.0001
0.01	0.9980 ± 0.0001
0.05	0.9982 ± 0.0001
0.1	0.9983 ± 0.0001
0.2	0.9984 ± 0.0001
0.5	1.0000 ± 0.0001

As previously discussed, nanofluids may present some instability issues over several parameters, such as pH, temperature, NPs type and size, and injection time after preparing. It is important to assure that nanoparticles in suspension are stable in order to maximize oil recovery in nanofluid flooding. Progressive coagulation and agglomeration of particles may hinder the potential benefits related to nanofluid injection. In this context, particle size analyses were carried out for the various SiO_2 nanofluid concentrations by dynamic light scattering (DLS) measurements. Fig. 4.11 to Fig. 4.15 shows the particle size results by intensity for each prepared nanofluid concentration. These measurements were conducted in triplicates, with the average hydrodynamic diameters and polydispersity index (PDI) being expressed in the images. It can be seen that the particle size curves form unimodal distributions regardless of NP concentration. Moreover, low PDI values were obtained, confirming the homogeneity of the size distributions. Fig. 4.16 shows a graphical representation of NPs size as a function of nanofluid concentration. By considering error bars due to triplicates, it can be seen that the average hydrodynamic of NPs remains constant with concentration. On the other hand, the average diameter value was around 200nm, being significantly higher than the 12nm SiO_2 NP diameter in precursor form. In this context, Li *et al*. [64] reported a similar size increase for SiO_2 NPs, changing from 7nm diameter in precursor stage to 158.6nm diameter with DLS in suspension in distilled water. They claimed that the hydrophilic tendency of NPs and their high specific surface area generally lead to a size increase of more than 100nm when in suspension in a base fluid.

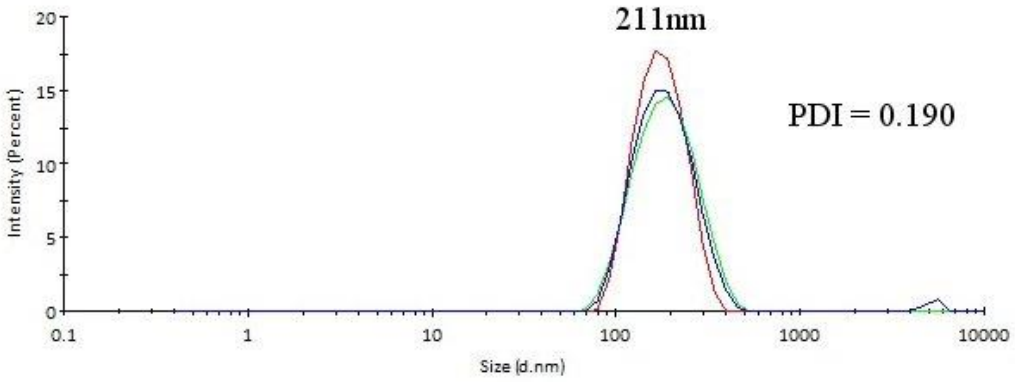

Fig. 4.11 – Particle size analysis for 0.01 wt.% SiO_2 nanofluid by intensity obtained in triplicates. The average hydrodynamic diameter of nanoparticles and average polydispersity index (PDI) are also being informed.

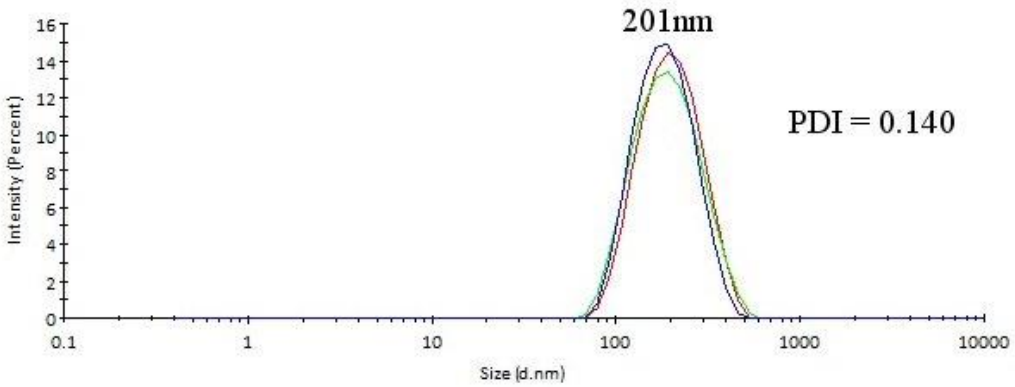

Fig. 4.12 – Particle size analysis for 0.05 wt.% SiO_2 nanofluid by intensity obtained in triplicates. The average hydrodynamic diameter of nanoparticles and average polydispersity index (PDI) are also being informed.

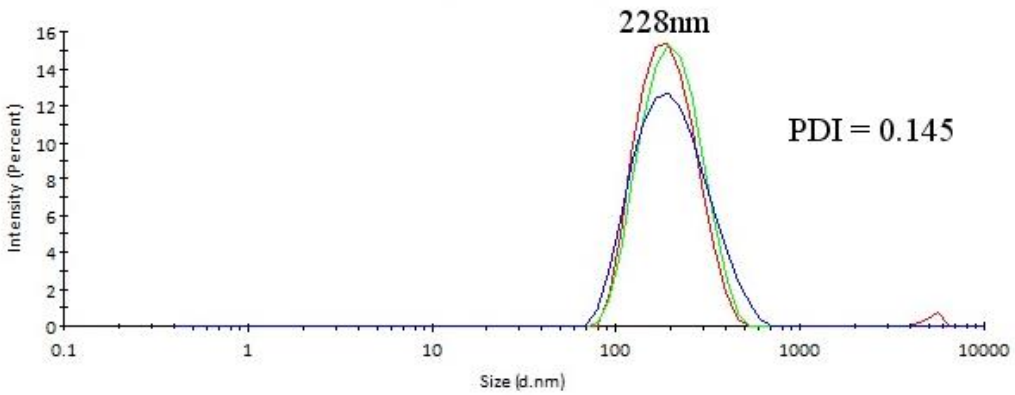

Fig. 4.13 – Particle size analysis for 0.1 wt.% SiO_2 nanofluid by intensity obtained in triplicates. The average hydrodynamic diameter of nanoparticles and average polydispersity index (PDI) are also being informed.

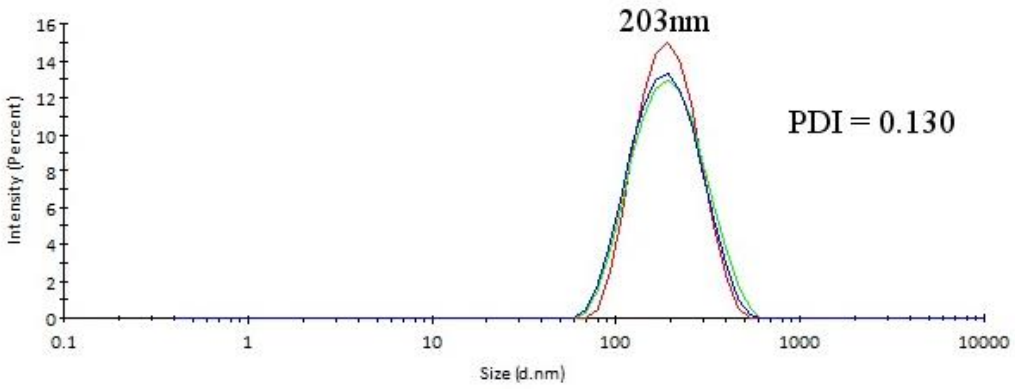

Fig. 4.14 – Particle size analysis for 0.2 wt.% SiO_2 nanofluid by intensity obtained in triplicates. The average hydrodynamic diameter of nanoparticles and average polydispersity index (PDI) are also being informed.

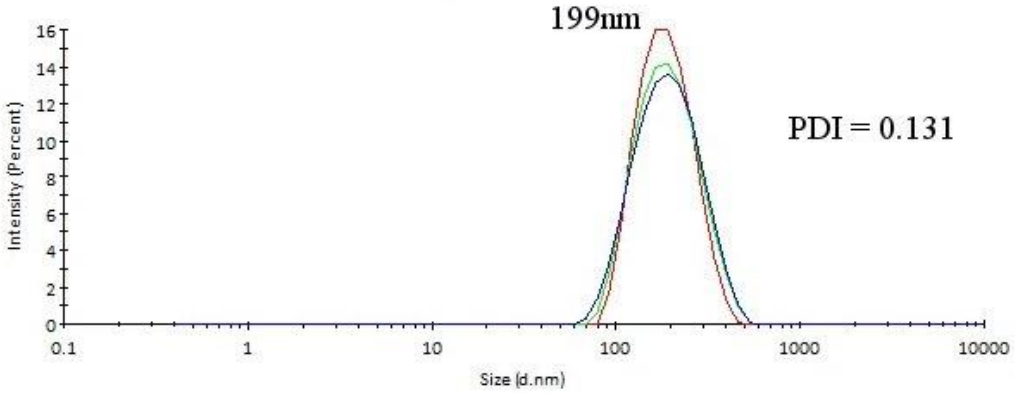

Fig. 4.15 – Particle size analysis for 0.5 wt.% SiO_2 nanofluid by intensity obtained in triplicates. The average hydrodynamic diameter of nanoparticles and average polydispersity index (PDI) are also being informed.

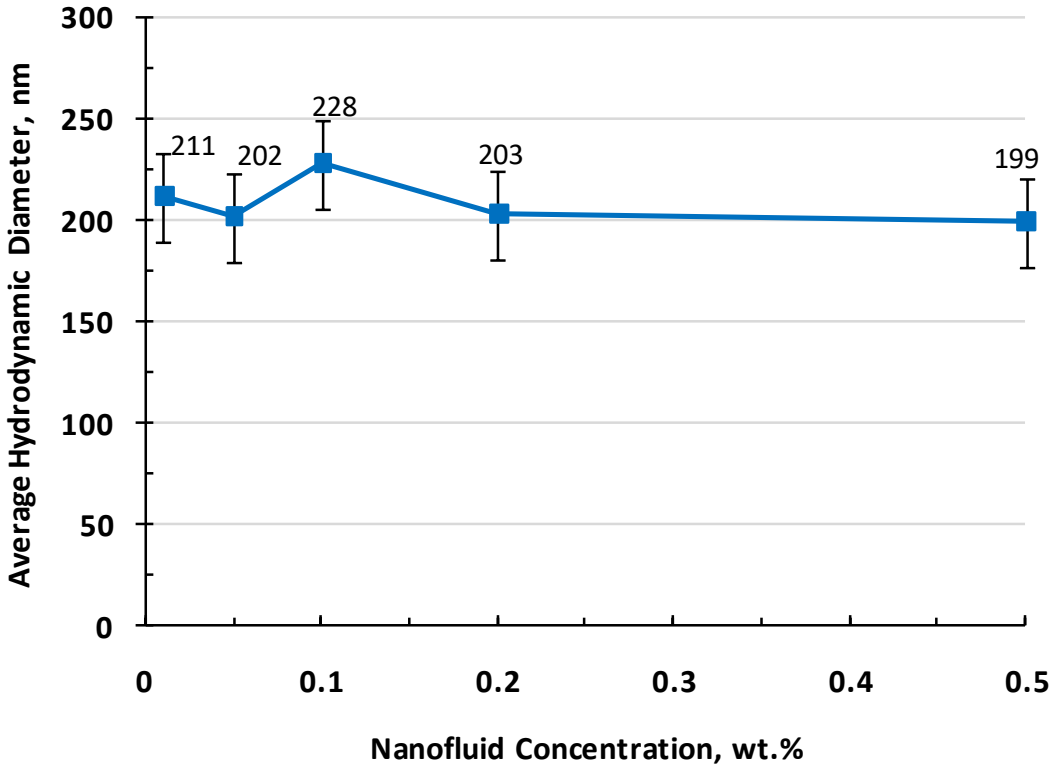

Fig. 4.16 – SiO_2 NPs size as a function of NP concentration. It can be seen that the average hydrodynamic of NPs remains constant with concentration. Error bars represent the standard deviation values in triplicates.

Following particles-size measurements, zeta potential analysis were carried out to evaluate nanofluid stability. Zeta potential is an electro-kinetic parameter that may be determined by the surface charge of particles in suspension in a polar medium. According to the DLVO theory, the stability of suspensions is directly related to the magnitude of zeta potential [156]. For high zeta potential absolute values, Van der Waals forces that aggregate particles are overcome by the repulsion due to their surface charges. It is accepted that zeta potential absolute values higher than ±30mV are sufficient to promote stability of water suspensions [157]. Fig. 4.17 shows zeta potential values for the SiO_2 nanofluids concentrations in neutral pH based on phase analysis light scattering (PALS) method. Zeta potential values for lower concentrations were around -30mV, increasing to -40mV for 0.1 wt.% NP concentration and then lowering to -24mV for 0.5 wt.% NP concentration. Moreover, it can be seen that SiO_2 NPs in water suspension are negatively charged for neutral pH. In this context, silica nanoparticles may present unsatisfied silicon- and oxygen- surface free bonds when manufactured. In an aqueous medium, these free bonds are neutralized by H^+ and OH^- species. The partial or total surface hydroxylation lead to the formation of silanol

groups [$Si(OH)_n$]. These silanol groups dissociates in pure water through the following reactions:

$$\equiv SiOH + OH^- \rightleftharpoons Si - O^- + H_20$$

$$\equiv SiOH + H^+ \rightleftharpoons Si - OH_2^+ + H_20$$

Alves and Baldo [157] studied the effect of pH in the zeta potential of silica nanoparticles. They reported that the isoelectric point (IEP) of SiO_2 NPs in distilled water is generally around pH = 2.5. This is the reason why silica nanoparticles are negatively charged in neutral or slightly acidic pH, as shown by Fig. 4.17. By considering the error bars associated to the triplicates, it is not possible to identify a variation tendency of zeta potential with concentration. Also, some NP concentrations showed zeta potential values higher than the ±30mV zeta potential value considered for stability, while other concentrations showed values lower than this threshold. Therefore, the confirmation of whether the NPs were considered stable or not by zeta potential analysis was not possible.

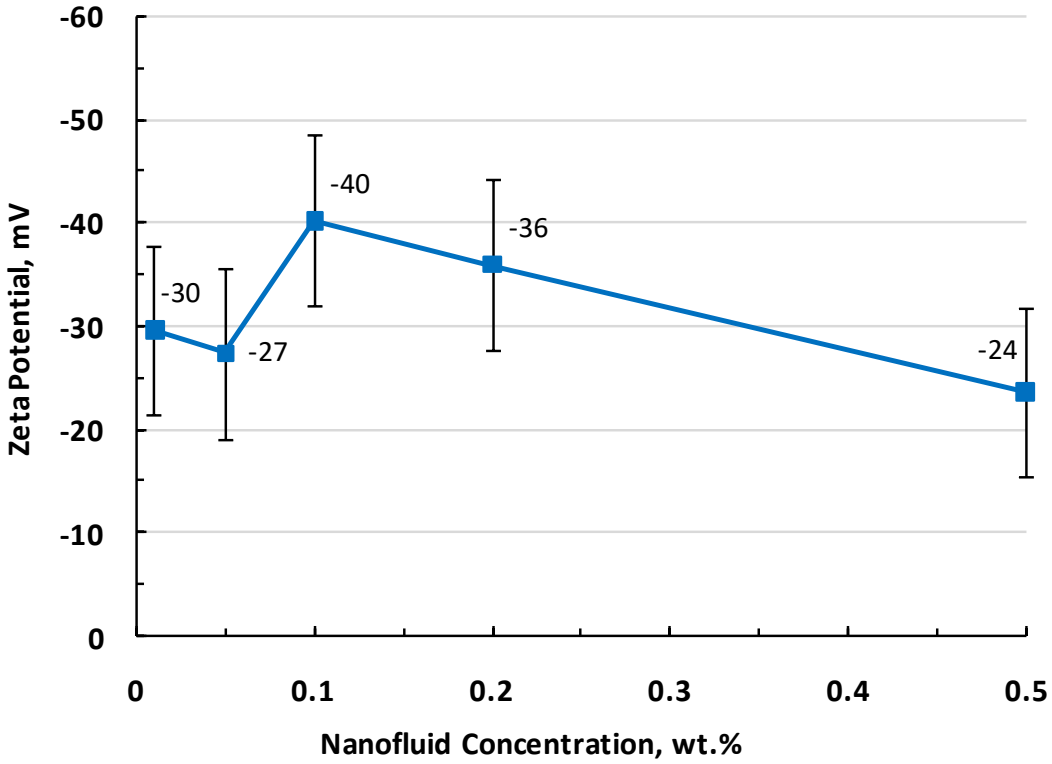

Fig. 4.17 – Zeta potential for nanofluids in neutral pH based on phase analysis light scattering (PALS) method. Error bars represent the standard deviation values in triplicates.

4.4 Interfacial and surface properties

Interfacial tension (IFT) and contact angle (CA) analyses were performed in order to evaluate the major mechanisms related to SiO_2 nanofluid flooding. These measurements were conducted by using the goniometer instrument. For IFT analysis, oil drops were left pendant in nanofluids in varied concentrations. For CA analysis, the oil drops were displaced onto the PDMS micromodel surface with nanofluids in varied concentrations as the external phase. Moreover, IFT measurements were conducted with and without the addition of biosurfactant, while CA measurements were conducted without biosurfactant addition due to the surface characteristics of the PDMS micromodel. IFT and CA measurements for the high NP concentration of 0.05 wt.% were not obtained due to the lack of optical visualization through the sample Table 4.4 contains a list of the obtained results for IFT and contact angles. The 0 wt.% nanofluid concentration corresponds to basically base fluid, or base fluid with biosurfactant in the case of IFT measurement. A 5% error was considered in all obtained measurements due to the absence of triplicates. Oil drop images related to these IFT and CA measurements are being shown in the appendix B (Fig. B.1, Fig. B.2 and Fig. B.3).

Table 4.4 – Interfacial tension (IFT) and contact angle (CA) results using the goniometer instrument. IFT measurements

Nanofluid concentration [wt. %]	IFT [mN/m]		CA [°]
	SiO_2 NPs	SiO_2 NPs + Biosurf	SiO_2 NPs
0	32.24	12.83	117.1
0.01	28.73	15.15	124.8
0.05	27.59	16.93	126.2
0.1	27.16	15.26	128.2
0.2	28.08	17.15	122.1

The reduction in interfacial tension between oil and injected fluid is an important mechanism for EOR, especially in surfactant flooding. According to Young-Laplace equation (Eq. 2), a decrease in IFT generates a reduction in capillary pressure between fluids, thus mobilizing the trapped oil remaining in some smaller pores and increasing oil recovery. In this context, the trend that IFT follows with SiO_2 NPs nanofluid concentration may be considered as a function of several parameters, such as pH, salinity, NP size, type of base fluid, composition of crude oil, as many others. Fig. 4.18 shows IFT values for crude oil/nanofluids in varied concentrations with and without

biosurfactant added. Without biosurfactant, IFT presents a slightly reduction with nanofluid concentration, from 32mN/m to 27mN/m for 0.1 wt.%. However, the addition of biosurfactant significantly reduced IFT from 32mN/m to 13mN/m, and then showing a minor increase with nanofluid concentration. Roustaei *et al.* [158] reported a IFT reduction with SiO_2 NPs and described this mechanism by the energetically favorable tendency that NPs have to adsorb at a fluid-fluid interface. When nanoparticles replace water/oil molecules, the new interactions across the interface are now between hydrophilic complexes and water at one side and hydrophobic complexes and oil at the other side. Since these new interactions are much stronger than regular water/oil interaction, the tension across the interface is then reduced. Mohajeri *et al*. [60] also reported an IFT reduction with silica NPs and claimed that was due to the formation of a mixed layer of NPs and natural surfactants existing in the oil, such as asphaltenes and resins. However, as nanoparticles concentration increases more than a critical value, natural surfactants in the oil will not be permit to adhere at this interface, leading to a slightly increase in the IFT between fluids [159]. Eshraghi *et al.* [160] also emphasized this increasing IFT behavior with nanofluid concentration due to surfactant replacement. They reported that the optimum SiO_2 nanofluid concentration with surfactant was 0.1 wt.%. In this context, Fig. 4.19 shows the oil drop image of the 0.1 wt.% SiO_2 NPs with biosurfactant as external phase. This NP concentration was the one selected to the secondary and tertiary EOR experiments.

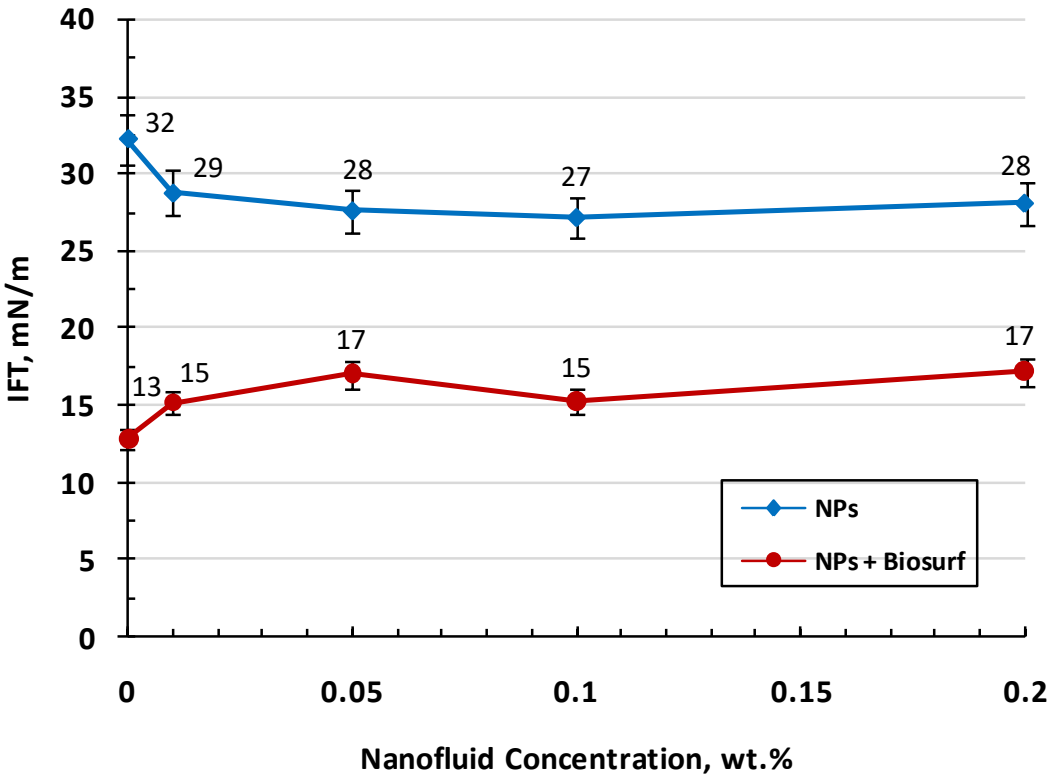

Fig. 4.18 – IFT for crude oil/SiO_2 nanofluids with and without biosurfactant. Without biosurfactant, IFT slightly reduced with increasing NPs concentration, remaining stable after a critical value. On the other hand, the addition of biosurfactant significantly reduced IFT from 32mN/m to 13mN/m, showing a minor increase with nanofluid concentration.

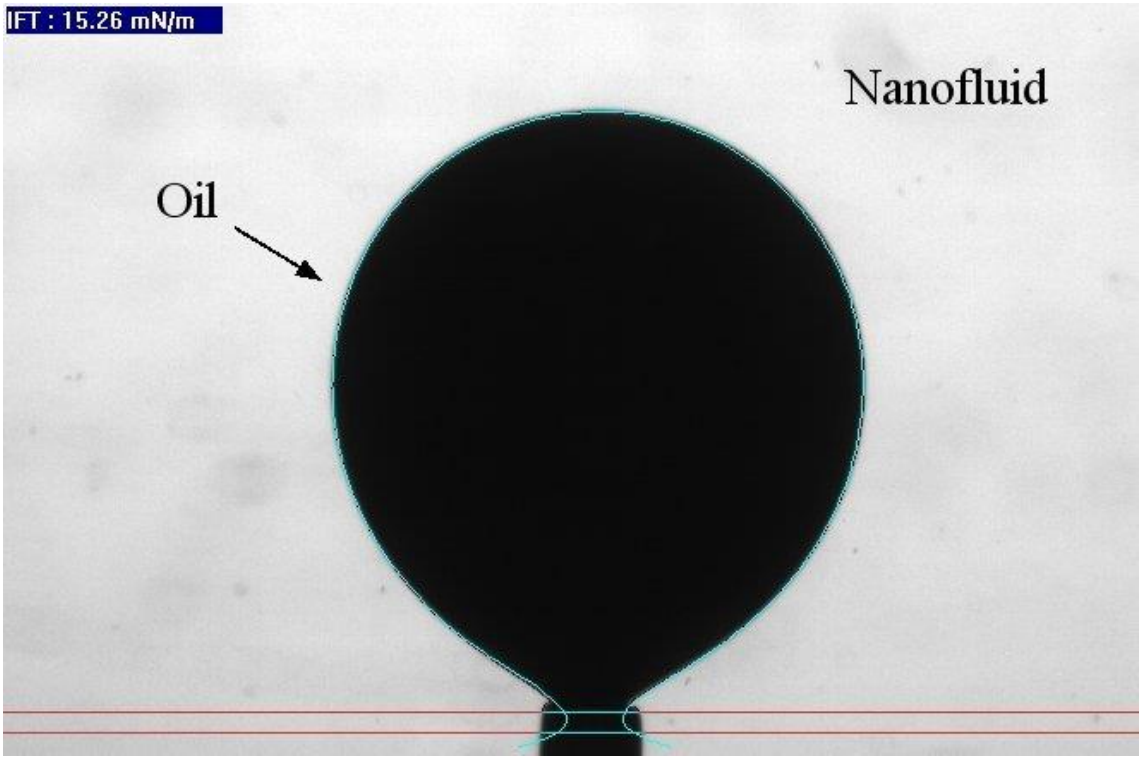

Fig. 4.19 – Oil drop image taken by the goniometer for the nanofluid concentration which was injected into the micromodel (0.1wt.% with biosurfactant) and its measured IFT value.

Finally, wettability conditions were evaluated for the crude oil/PDMS/ nanofluids systems. As desired in EOR applications, the contact angle in the interface between a drop of oil and external fluid/rock must decrease towards a more water-wet condition [161]. When water is the wetting fluid, oil relative permeability is then increased and capillary pressure decreased. As discussed before, these relationships between petrophysical properties positively impact oil recovery. Fig. 4.20 shows contact angle (CA) values for crude oil/PDMS/nanofluids systems. PDMS´s hydrophobicity can be observed in all nanofluid concentrations, since the CA is higher than 90°. By considering error bars, the increase in nanofluid concentration showed no impact in wettability alteration. Generally, wettability changes for PDMS´s microfluidic devices are achieved by the means of surface modification techniques [162]. The stable wetting behavior of PDMS with nanofluid can be understood by the absence of electrical charges on the surface of the polymeric material that would interact with the negatively charged SiO_2 NPs. In fact, most of the literature results of increased oil recovery in nanofluid flooding by wettability alterations were achieved in glass micromodels or core samples. Rostami *et al.* [48] reported a contact angle decrease from ~ 135° to 90° in a glass micromodel after aged with silica nanofluid for 2 hours. They described this

mechanism as the adsorption and formation of a nanotexture coating on the oil-wet surface of glass, altering its wettability state to intermediate wetting, and increasing oil recovery. Since this wettability behavior was not observed in this study, changes in fluid-fluid interactions or interfaces must be focused when studying nanofluid flooding in PDMS micromodels. Additionally, PDMS´s hydrophobicity can be seen in Fig. 4.21.

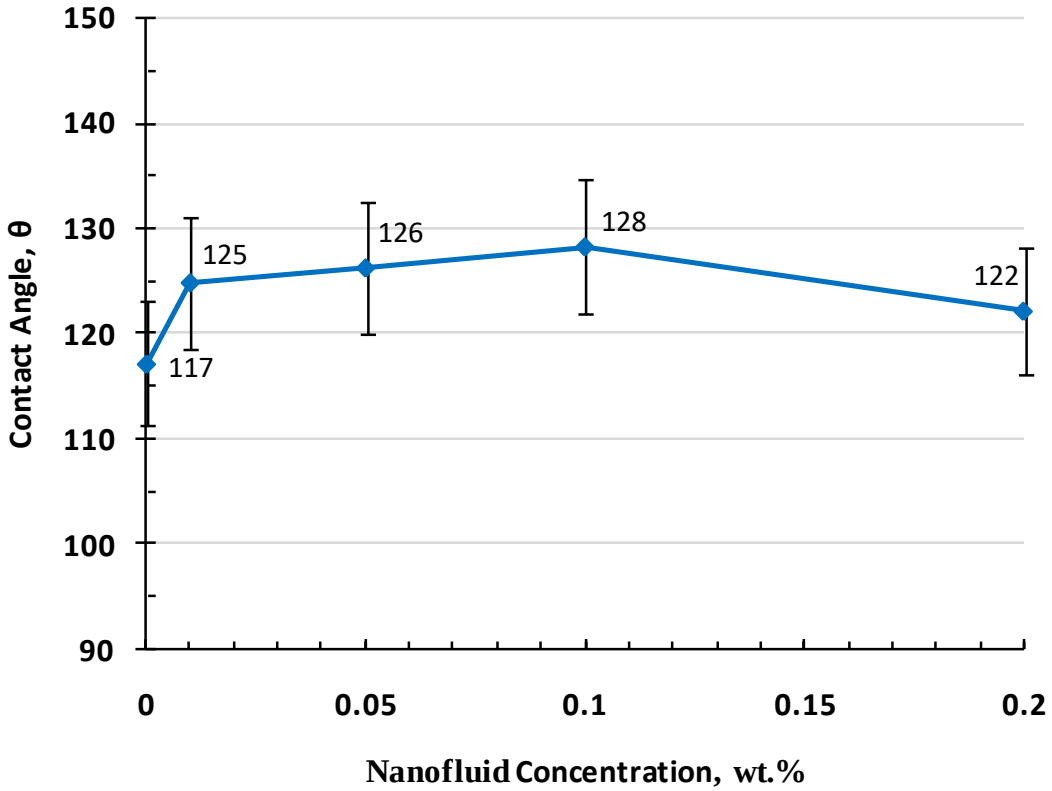

Fig. 4.20 – Contact angle values (CA) for crude oil/PDMS/nanofluids systems. PDMS´s hydrophobicity is being shown for all nanofluid concentrations. Considering error bars, CA values remained stable with increasing concentration. This stable wettability behavior can be understood by the lack of electrical charges in the PDMS´ surface, thus not interacting with the negatively charged silica nanoparticles present in the nanofluid.

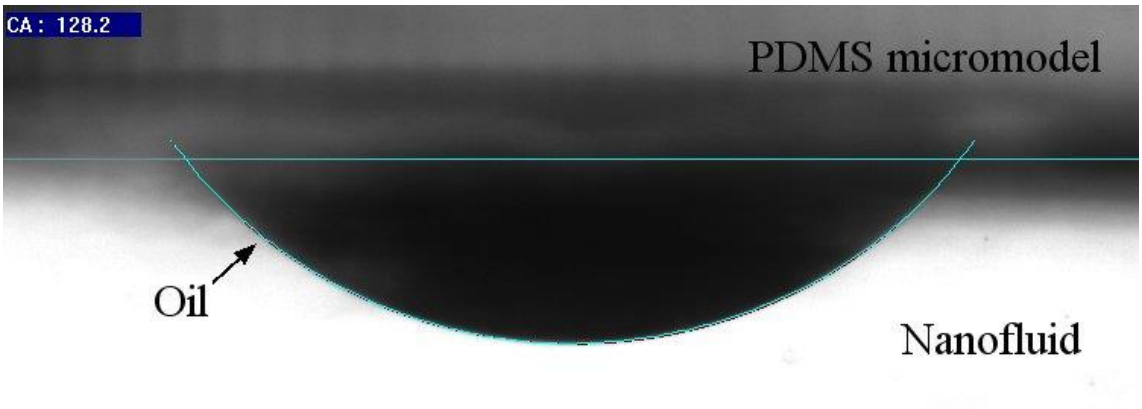

Fig. 4.21 – Oil drop image taken by the goniometer for the 0.1 wt.% nanofluid concentration and its measured CA value.

4.5 EOR experiments

In this work, oil recovery was analyzed in two experiments. The first one consisted of consecutive injection of brine and SiO_2 nanofluids (0.1 wt.% with biosurfactant) to represent secondary and tertiary recovery processes. Another experiment was performed to evaluate the effectiveness of nanofluid flooding as secondary recovery. In the first experiment, four PV of each fluid were injected consecutively with a constant flow rate of 0.01μL/min, which is similar to conventional liquid flow velocities in oil reservoirs. In the second experiment, 8 PV of nanofluid were injected in the same flow rate. Table 4.5 shows the obtained oil recovery factors for brine- and nanofluid- flooding in the tertiary and secondary recovery experiments.

Table 4.5 – Oil recovery factors obtained by brine flooding and nanofluid flooding in the secondary and tertiary recovery experiments.

PV injected	Tertiary recovery experiment		Secondary recovery experiment
	Brine flooding [%]	Nanofluid flooding [%]	Nanofluid flooding [%]
0	0	-	0
1	59	-	74
2	60	-	78
3	62	-	78
4	62	-	79
5	-	64	82
6	-	66	84
7	-	73	84
8	-	74	85

Fig. 4.22 shows obtained results for the secondary and tertiary recovery processes. In tertiary recovery, brine injection displaced approximately 62% of oil. Consecutive brine and silica nanofluid injection recovered approximately 74% of oil; therefore incremental recovery of nanofluid-EOR process was 12%. Fig. 4.23 and Fig. 4.24 show the coupled images during brine- and nanofluid- flooding in the tertiary recovery experiment. In order to observe the additional contribution of the nanofluid to the oil recovery, the images of 6 PV and 7 PV which represented an increase in 7% in the oil recovery were compared (Fig. 4.25). The white regions represented the areas where nanofluid invaded, achieving a 7% increase in the oil recovery. Thus, a considerably difference between brine and nanofluid injection was observed, indicating the benefit of the nanofluid to oil recovery. It is important to emphasize that the obtained oil recovery factors for the EOR experiments in a micromodel were significantly higher than the expected if the same recovery experiments would have been performed in coreflood or at field-scale. This increase in the oil recovery is related to the pore dimensions of the micromodel pore-network and the various geologic processes that were disconsidered during the nano-EOR experiments.

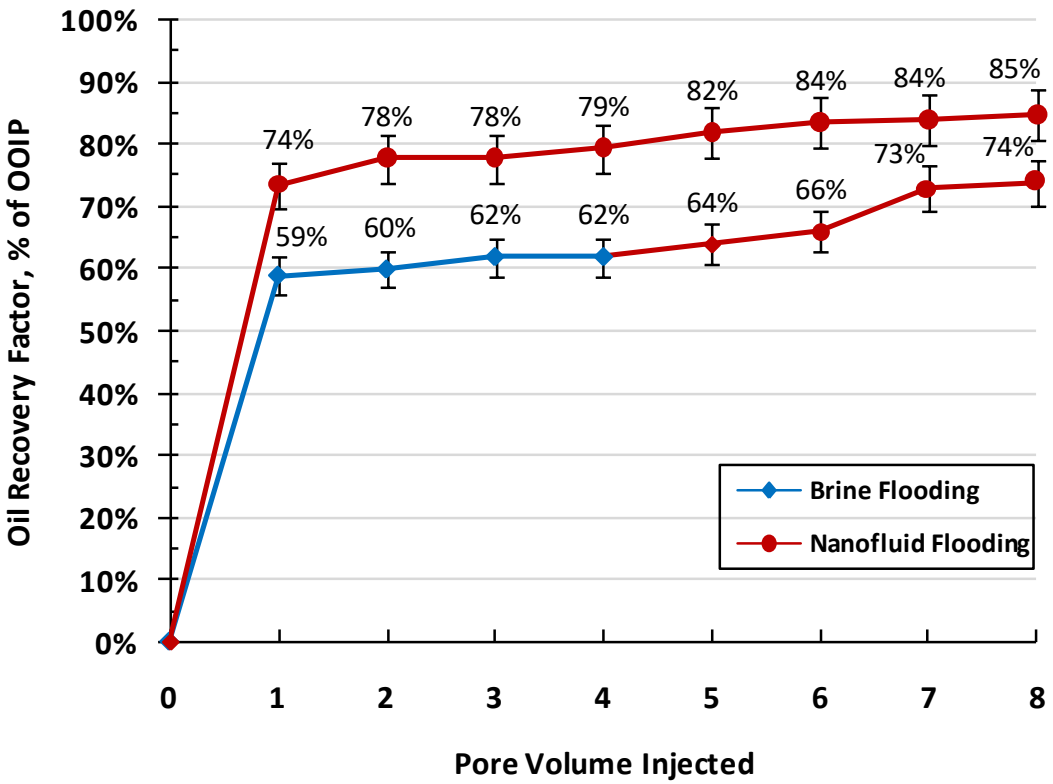

Fig. 4.22 – Oil recovery performances for brine flooding and SiO_2 nanofluid flooding (0.1 wt.% with biosurfactant) as secondary and tertiary recovery experiments in a PDMS micromodel.

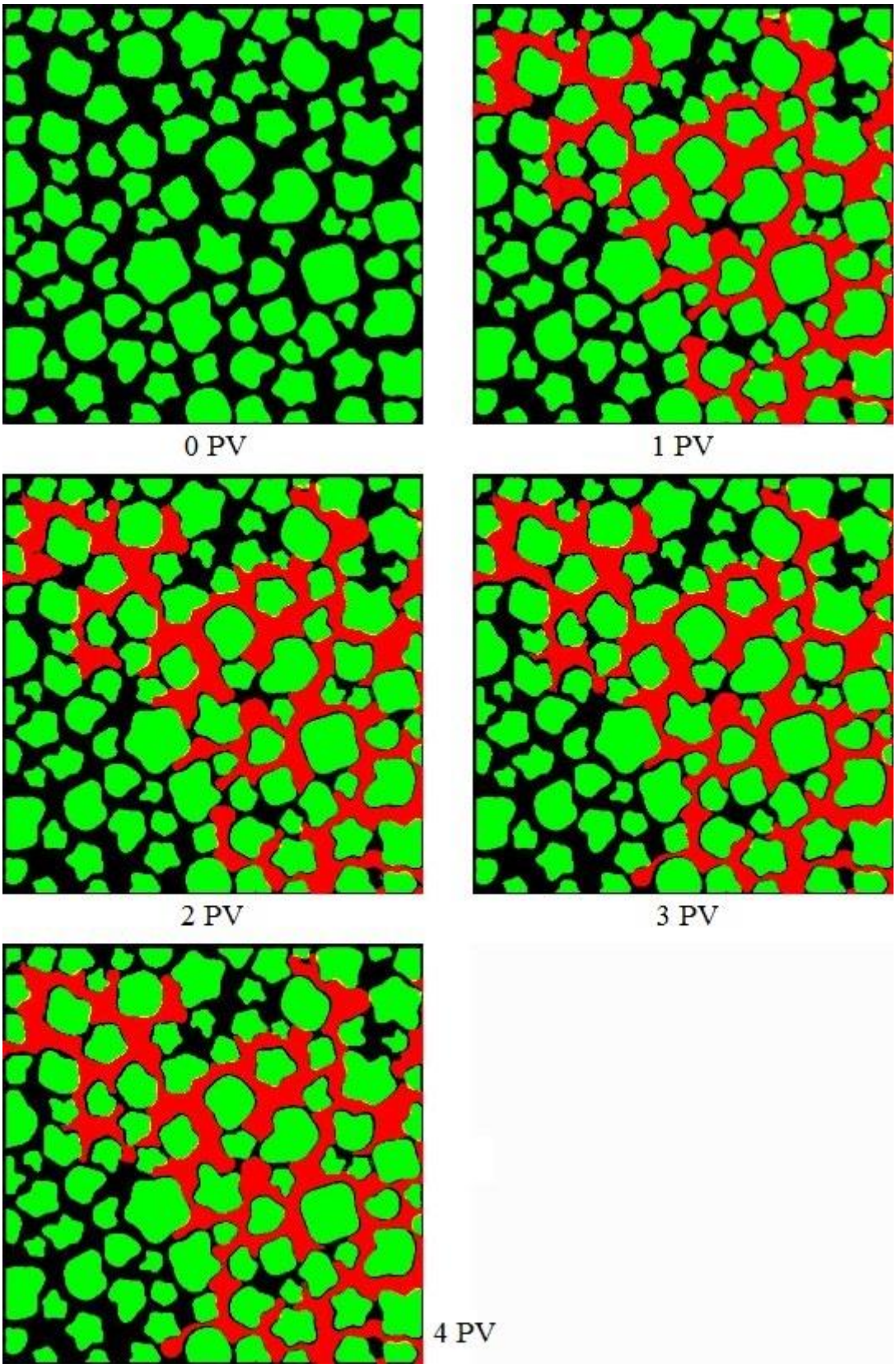

Fig. 4.23 – Coupled images for brine flooding in the first experiment simulating secondary and tertiary recovery processes.

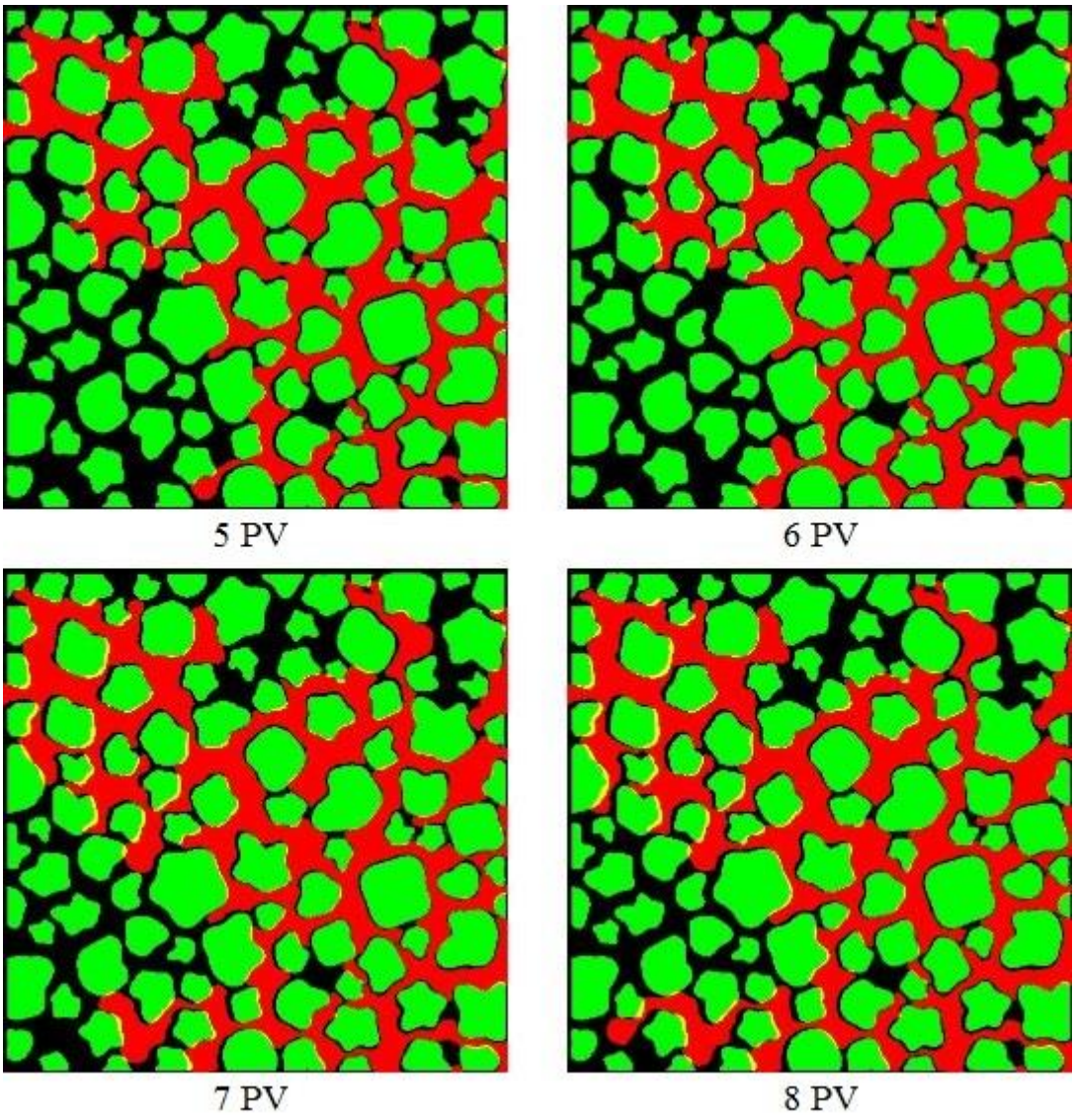

Fig. 4.24 – Coupled images for nanofluid flooding in the first experiment simulating secondary and tertiary recovery processes.

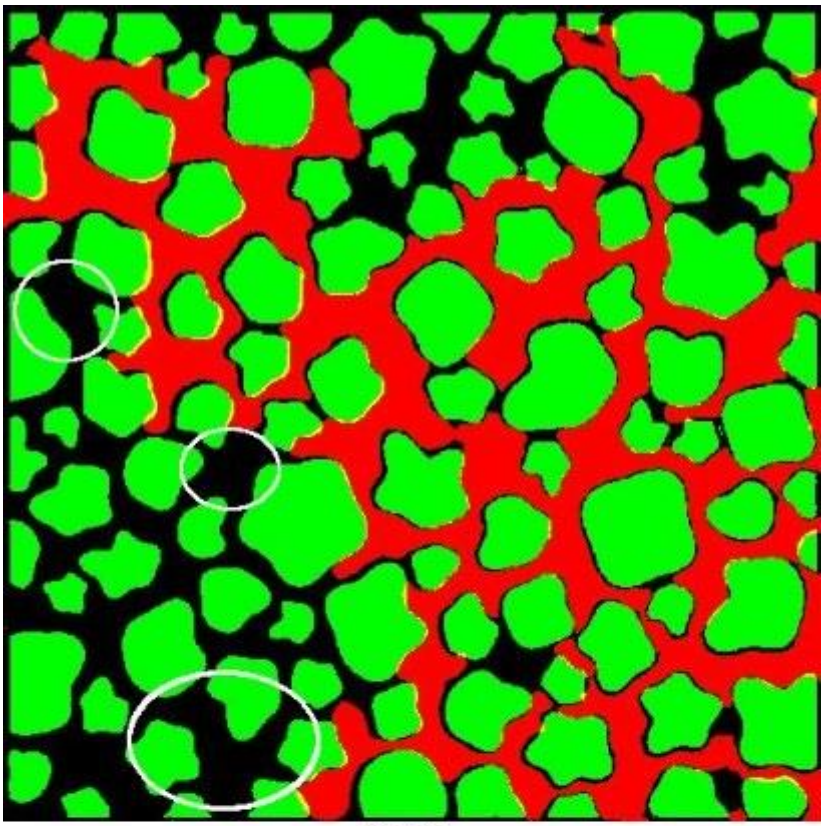

Fig. 4.25 – 6 PV and 7 PV images of tertiary recovery representing the highest increase of oil recovery due to nanofluid flooding (7%). White regions shows the nanofluid invasion.

For secondary recovery, the nanofluid injection displaced 85% of oil, therefore recovering 11% more oil when compared to tertiary recovery. Fig. 4.26 and Fig. 4.27 show coupled images during nanofluid flooding as secondary recovery. By observing Fig. 4.22, it can be seen that after 1 PV injected, nanofluid contribution to oil recovery was almost constant during the experiment. Therefore, the dominant EOR mechanism related to the SiO_2 nanofluid flooding was considered to be IFT reduction (27mN/m to 15mN/m for 0.01 wt.%). No wettability alteration of PDMS has been observed. Li *et al.* [163] conducted similar experiments in a dry-etched silica-based micromodel by injecting SiO_2 nanofluids (0.1 wt.%) to displace dodecane (1.36cP at 25°C). They reported a 25% incremental oil recovery by nanofluid injection at the same flow rate of this work (0.01μL/min), associating the major EOR mechanism to wettability alteration. A significant IFT reduction has also been reported. Finally, it is believed that the difference between obtained oil recoveries is related to the different surface chemistries and interactions between both micromodel materials and injected nanofluids. Additionally, appendix C contains original flow images, computer-stacked images and segmented images of both experiments (Fig. C.1 to Fig. C.11). As previously explained, the stacking imaging process was necessary to account for the presence of entrained air during the tests, occupying pore spaces that were previously occupied by injected oil. In fact, a 5% error was considered in oil recovery obtained data due to air migration and image-processing techniques that were employed to acquire the results.

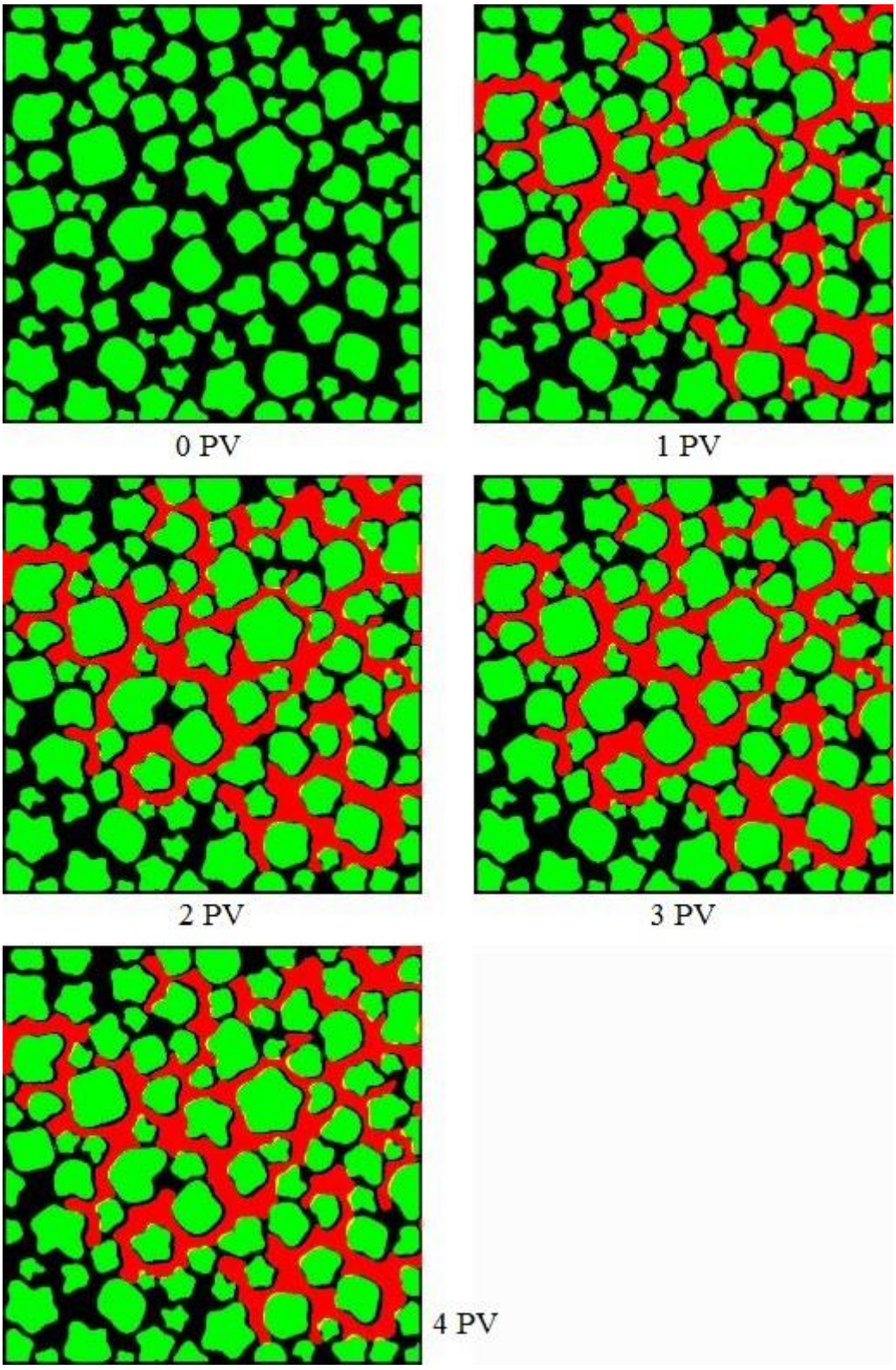

Fig. 4.26 – Coupled images of 4 PV nanofluid injected in the second experiment as a secondary recovery process.

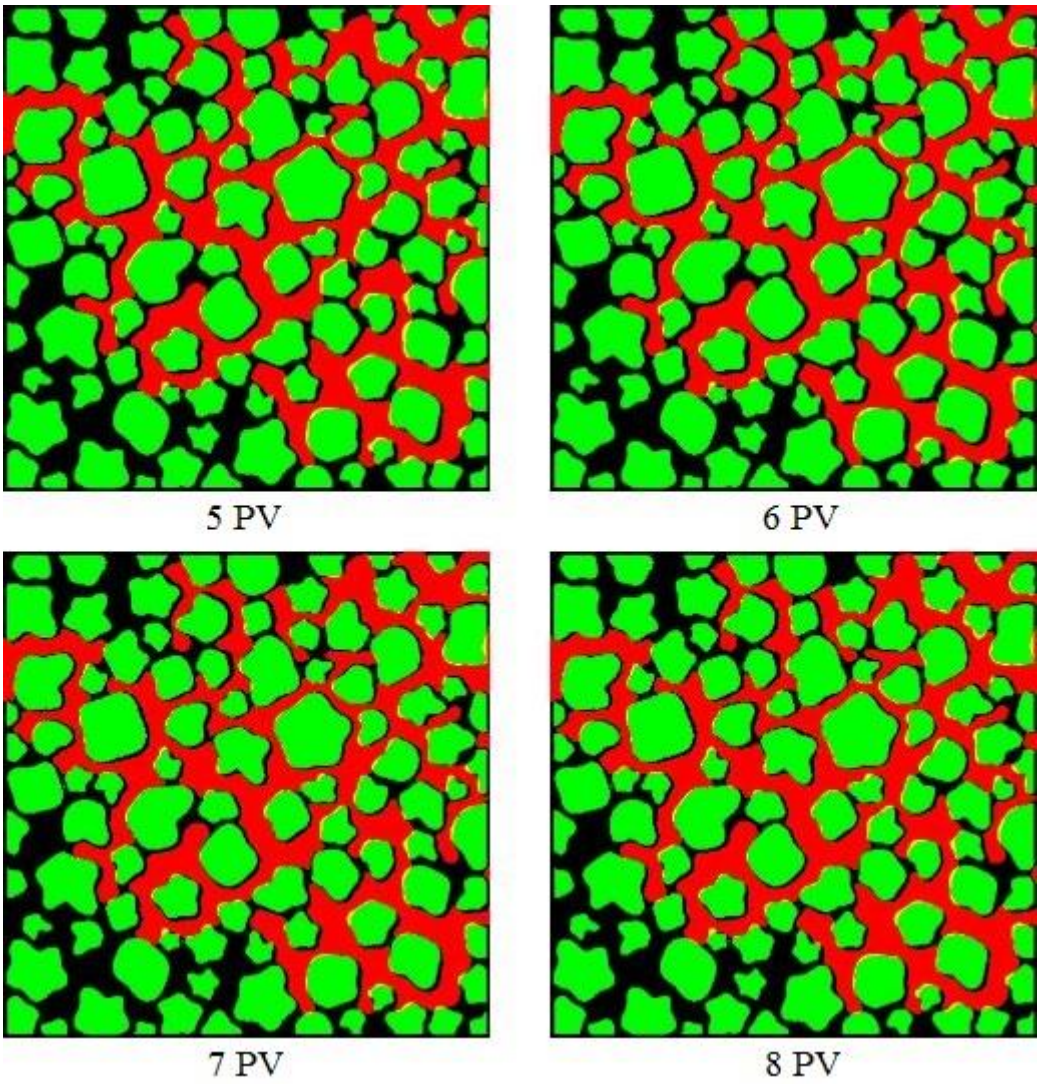

Fig. 4.27 – Coupled images of 8 PV nanofluid injected in the second experiment as a secondary recovery process.

5 CONCLUSION AND FUTURE WORK

In this work, a complete procedure to generate varied grain-sorting porous media and fabricate PDMS micromodels with different designs has been proposed. Moreover, preparation of silica nanofluids in nanofiltered water (NF90) with and without biosurfactant addition has been made. Fluid characterization tests regarding particles-size, zeta potential, interfacial tension and contact angle were performed. Finally, two nanofluid-EOR processes consisting of secondary recovery and tertiary recovery in a PDMS micromodel has also been demonstrated. The following results were discussed:

- The methodology to generate the pore-networks, design the CAD templates and fabricate the micromodels has been demonstrated. The micromodel dimensional characterization showed a high resemblance to the designed micromodel in the CAD template. Thus, the combined processes of micromilling and soft lithography on PDMS are effective to reproduce real-rock based micromodels.
- Average hydrodynamic diameters analyzed by DLS method showed a constant behavior in the particles-size with concentration, being in the order of 200nm. Moreover, zeta potential measurements by PALS method also showed a constant behavior with NP concentration, although the nanofluids might not be confirmed as stable in neutral pH (zeta potential absolute values higher than ±30mV).
- It has not been seen reduction in IFT values for crude oil/nanofluids systems with increasing NP concentration. On the other hand, the addition of biosurfactant significantly reduced IFT from 32mN/m to 13mN/m, although an increase in NP concentration with biosurfactant had no effect on IFT. Moreover, contact angle measurements for crude oil/PDMS/nanofluids systems were performed. PDMS showed no wettability alteration when nanofluid was added or NP concentrations changed. This stable wetting tendency of the polymer is due to the lack of surface charges to interact with negatively charged SiO_2 NPs.
- In the tertiary recovery experiment, consecutive brine and nanofluid flooding recovered 74% of oil. An additional 12% oil recovery was achieved with silica nanofluid-EOR. In the secondary recovery, nanofluid injection displaced 85% of oil. It was observed that nanofluids recovered 11% more oil in secondary recovery when compared to tertiary recovery. The dominant EOR mechanism was associated to IFT reduction, changing from 27mN/m to 15mN/m for 0.1 wt.% SiO_2 NP with biosurfactant.

According to the multidisciplinary approach of this study, several futures works arise to address new solutions to issues here observed. Some other options related to different EOR experiments are also welcomed. The following studies will be suggested:

- Different variations in the petrophysical parameters related to the generated pore-networks. Here, it was discussed aspects related to differences in sorting and porosity. In contrast, differences in permeability are also interesting. Anisotropy variations that occur in real-rocks (for example, shale reservoirs) might be analyzed by performing angular deformation in the generated grains.
- Regarding flow experiments, the calculation of the permeability of the micromodel pore-network is an interesting topic. This could be performed by installing pressure sensors in the inlet/outlet of the micromodel to obtain the differential pressure across the pore-network and adjust this value to a flow equation in porous media for a specific injected fluid and flow regime.
- Studies in various EOR methods may be performed in micromodels. When referring to PDMS micromodels, EOR mechanisms related to fluid/fluid interfaces are of great importance. Viscous polymer flooding, for example, would be easily analyzed in various pore-geometries in PDMS micromodels.
- Flow assurance studies in PDMS micromodels are also a great topic. In this context, several undesirable compounds often precipitate in real reservoirs and hinder production. The physico-chemical process of paraffin or asphaltene deposition may be analyzed, and also their inhibition by injecting chemicals.
- EOR studies in real-reservoir pressure and temperature. The conclusions here reported were considered in ambient conditions. However, there is a great opportunity to evaluate information regarding real-field conditions. High-pressure, high-temperature (HPHT) might also be considered.

6 REFERENCES

[1] YERGIN, D. **The Prize: The Epic Quest for Oil, Money & Power**Free Press, , 2011. Disponível em: <https://books.google.com.br/books?id=WiUTwBTux2oC>

[2] COMPANY, B. P. **BP Statistical Review of World Energy**London, 2018.

[3] ANP. **ANP participa da inauguração de laboratório que visa aumentar produtividade de petróleo**. Disponível em: <http://www.anp.gov.br/noticias/4947-anp-participa-da-inauguracao-de-laboratorio-que-visa-aumentar-produtividade-de-petroleo>. Acesso em: 12 apr. 2018.

[4] AHMED, T. **Reservoir Engineering Handbook**Elsevier Science, , 2010. Disponível em: <https://books.google.com.br/books?id=LXJcG_jwTHAC>

[5] SUN, X. Application of Nanoparticles in Enhanced Oil Recovery: A Critical Review of Recent Progress. **Energies**, v. 10, 11 Mar. 2017.

[6] EL-DIASTY, A. I.; RAGAB, A. M. S. **Applications of Nanotechnology in the Oil & Gas Industry: Latest Trends Worldwide & Future Challenges in EgyptNorth Africa Technical Conference and Exhibition**Cairo, EgyptSociety of Petroleum Engineers, , 2013. Disponível em: <https://doi.org/10.2118/164716-MS>

[7] GUPTA, R. et al. **A Novel, Field-representative Enhanced Oil Recovery Coreflood MethodSPE Improved Oil Recovery Symposium**Tulsa, Oklahoma, USASociety of Petroleum Engineers, , 2014. Disponível em: <https://doi.org/10.2118/169088-MS>

[8] LRAP/COPPE/UFRJ. **LRAP/COPPE/UFRJ**. Disponível em: <http://www.lrap.coppe.ufrj.br/equipamentos/estufas-de-core-flood/>. Acesso em: 6 apr. 2019.

[9] VARHAUG, M.; SMITHSON, T. Getting to the Core of the Matter. n. May, p. 63–64, 2015.

[10] HENDRANINGRAT, L.; LI, S.; TORSÆTER, O. A coreflood investigation of nanofluid enhanced oil recovery. **Journal of Petroleum Science and Engineering**, v. 111, p. 128–138, 2013.

[11] LIFTON, V. Microfluidics: An enabling screening technology for enhanced oil recovery (EOR). **Lab Chip**, v. 16, 18 Apr. 2016.

[12] JACOBS, T. Reservoir-on-a-Chip Technology Opens a New Window Into Oilfield Chemistry. **Journal of Petroleum Technology**, v. 71, p. 25–27, 1 Jan. 2019.

[13] DORYANI, H.; MALAYERI, M. R.; RIAZI, M. Visualization of asphaltene

precipitation and deposition in a uniformly patterned glass micromodel. **Fuel**, v. 182, p. 613–622, 2016.

[14] SINTON, D. Microfluidics and Their Macro Applications for the Oil and Gas Industry. **The Way Ahead**, v. 11, n. 03, p. 8–10, 2015.

[15] GUNDA, N. S. K. et al. Reservoir-on-a-Chip (ROC): A new paradigm in reservoir engineering. **Lab on a chip**, v. 11, p. 3785–3792, 21 Nov. 2011.

[16] CHATENEVER, A.; CALHOUN JR., J. C. Visual Examinations of Fluid Behavior in Porous Media - Part I. **Journal of Petroleum Technology**, v. 4, n. 06, p. 149–156, 1952.

[17] CHUOKE, R. L.; MEURS, P. VAN; POEL, C. VAN DER. **The Instability of Slow, Immiscible, Viscous Liquid-Liquid Displacements in Permeable Media**Society of Petroleum Engineers, , 1959. Disponível em: <https://doi.org/>

[18] KARADIMITRIOU, N. K.; HASSANIZADEH, S. A Review of Micromodels and Their Use in Two-Phase Flow Studies. **Vadose Zone Journal**, v. 11, p. 0, 1 Aug. 2012.

[19] MATTAX, C. C.; KYTE, J. R. Ever see a water flood? **Oil Gas J.**, v. 59, p. 115–128, 1 Jan. 1961.

[20] QUAKE, S. R.; SCHERER, A. From Micro- to Nanofabrication with Soft Materials. **Science**, v. 290, n. 5496, p. 1536 LP – 1540, 24 Nov. 2000.

[21] SENN, T. et al. Replica molding for multilevel micro nanostructure replication. **Journal of Micromechanics and Microengineering**, v. 20, p. 115012, 8 Oct. 2010.

[22] WILSON, M. E. et al. Fabrication of circular microfluidic channels by combining mechanical micromilling and soft lithography. **Lab on a Chip**, v. 11, n. 8, p. 1550–1555, 2011.

[23] COLMAN, J. **Projeto, fabricação e ensaio de dispositivo microfluídico para separação de células sanguíneas baseado no efeito zweifach-fung**. 2017. 176 f. COPPE/UFRJ. 2017.

[24] ABDALLAH, W. et al. Fundamentals of wettability. **Oilfield Review**, v. 19, p. 44–61, 1 Jun. 2007.

[25] HOLSTEIN, E. D.; LAKE, L. W.; ENGINEERS, U. S. A. S. OF P. **Petroleum engineering handbook. Vol.5. Reservoir engineering and petrophysics**SPE, , 2007. Disponível em: <https://books.google.com.br/books?id=B46_wwEACAAJ>

[26] WILLHITE, G. P.; AIME., S. OF P. E. OF. **Waterflooding**: SPE textbook series.Society of Petroleum Engineers, , 1986. Disponível em: <https://books.google.com.br/books?id=AVpQAQAAIAAJ>

[27] PROTHERO, D. R.; SCHWAB, F. **Sedimentary Geology**W. H. Freeman, , 2004. Disponível em: <https://books.google.com.br/books?id=vlG-BGZhZrAC>

[28] SONG, W. et al. Chip-off-the-old-rock: The study of reservoir-relevant geological processes with real-rock micromodels. **Lab Chip**, v. 14, 11 Sep. 2014.

[29] MORROW, N. R. **Interfacial Phenomena in Petroleum Recovery**: Surfactant Science.Taylor & Francis, , 1990. Disponível em: <https://books.google.com.br/books?id=Jz70HZMPGWoC>

[30] OREN, P. E.; BILLIOTTE, J.; PINCZEWSKI, W. V. Mobilization of Waterflood Residual Oil by Gas Injection for Water-Wet Conditions. **SPE Formation Evaluation**, v. 7, n. 01, p. 70–78, 1992.

[31] BORA, R.; MAINI, B. B.; CHAKMA, A. Flow Visualization Studies of Solution Gas Drive Process in Heavy Oil Reservoirs Using a Glass Micromodel. **SPE Reservoir Evaluation & Engineering**, v. 3, n. 03, p. 224–229, 2000.

[32] LAGO, M.; HUERTA, M.; GOMES, R. Visualization Study During Depletion Experiments of Venezuelan Heavy Oils Using Glass Micromodels. **Journal of Canadian Petroleum Technology**, v. 41, n. 01, p. 7, 2002.

[33] ROMERO, C.; ALVAREZ, J. M.; MÜLLER, A. J. **Micromodel Studies of Polymer-Enhanced Foam Flow Through Porous MediaSPE/DOE Improved Oil Recovery Symposium**Tulsa, OklahomaSociety of Petroleum Engineers, , 2002. Disponível em: <https://doi.org/10.2118/75179-MS>

[34] ROBIN, M.; BEHOT, J.; SYGOUNI, V. **CO2 Injection in Porous Media : Observations un Glass Micromodels Under Reservoir ConditionsSPE - DOE Improved Oil Recovery Symposium Proceedings**, 1 Jan. 2012.

[35] MEGHDADI ISFAHANI, A. H.; HEYHAT, M. M. Experimental Study of Nanofluids Flow in a Micromodel as Porous Medium. **International Journal of Nanoscience and Nanotechnology**, v. 9, n. 2, p. 77–84, 1 Jun. 2013.

[36] GHARIBSHAHI, R. et al. **Simulation of Nanofluid Flooding in a Micromodel with Quadratic Pore Shape Using CFD**, 11 Jun. 2014.

[37] LIMA, N. M. DE. **Porescale analysis of oil displacement by polymer solution**. 2016. PUC/RIO. 2016.

[38] CHERAGHIAN, G. Effects of titanium dioxide nanoparticles on the efficiency of surfactant flooding of heavy oil in a glass micromodel. **Petroleum Science and Technology**, v. 34, n. 3, p. 260–267, 1 Feb. 2016.

[39] JUNIOR, J. R. . **Three-dimensional visualization of oil displacement by flexible**

microcapsules suspensions in porous media. 2017. PUC-RIO. 2017.

[40] MEGHDADI ISFAHANI, A. H.; AFRAND, M. Experiment and Lattice Boltzmann numerical study on nanofluids flow in a micromodel as porous medium. **Physica E: Low-dimensional Systems and Nanostructures**, v. 94, p. 15–21, 2017.

[41] DIJKE, M. I. J. VAN et al. **Three-Phase Flow In Wag Processes In Mixed-Wet Porous Media: Pore-Scale Network Simulations And Comparison With Micromodel ExperimentsSPE/DOE Improved Oil Recovery Symposium**Tulsa, OklahomaSociety of Petroleum Engineers, , 2002. Disponível em: <https://doi.org/10.2118/75192-MS>

[42] SOHRABI, M.; DANESH, A.; JAMIOLAHMADY, M. Visualisation of Residual Oil Recovery by Near-miscible Gas and SWAG Injection Using High-pressure Micromodels. **Transport in Porous Media**, v. 74, p. 239–257, 1 Sep. 2008.

[43] HEMATPUR, H. et al. An Experimental Investigation of Surfactant Flooding Efficiency in Low Viscosity Oil Using a Glass Micromodel. **Energy Sources Part A-recovery Utilization and Environmental Effects**, v. 34, p. 1745–1758, 26 Jul. 2012.

[44] HENDRANINGRAT, L. et al. **A Glass Micromodel Experimental Study of Hydrophilic Nanoparticles Retention for EOR ProjectSPE Russian Oil and Gas Exploration and Production Technical Conference and Exhibition**Moscow, RussiaSociety of Petroleum Engineers, , 2012. Disponível em: <https://doi.org/10.2118/159161-MS>

[45] LI, S.; HENDRANINGRAT, L.; TORSAETER, O. **Improved Oil Recovery by Hydrophilic Silica Nanoparticles Suspension: 2-Phase Flow Experimental StudiesInternational Petroleum Technology Conference**Beijing, ChinaInternational Petroleum Technology Conference, , 2013. Disponível em: <https://doi.org/10.2523/IPTC-16707-MS>

[46] LI, S.; TORSÆTER, O. **An Experimental Investigation of EOR Mechanisms for Nanoparticles Fluid in Glass Micromodel**, 8 Sep. 2014.

[47] NGUYEN, P.; FADAEI, H.; SINTON, D. Pore-Scale Assessment of Nanoparticle-Stabilized CO2 Foam for Enhanced Oil Recovery. **Energy & Fuels**, v. 28, p. 6221–6227, 1 Oct. 2014.

[48] ROSTAMI, P. et al. The effect of nanoparticles on wettability alteration for enhanced oil recovery: micromodel experimental studies and CFD simulation. **Petroleum Science**, 2019.

[49] HORNBROOK, J. W.; CASTANIER, L. M.; PETTIT, P. A. **Observation of**

Foam/Oil Interactions in a New, High-Resolution MicromodelSPE Annual Technical Conference and Exhibition Dallas, TexasSociety of Petroleum Engineers, , 1991. Disponível em: <https://doi.org/10.2118/22631-MS>

[50] LIU, Z. et al. **Comparison of Displacement Oil Mechanism of Polymer, ASP and Foam of ASP in Micro Pores and Dead Ends of PoresSPE Asia Pacific Oil and Gas Conference and Exhibition**Melbourne, AustraliaSociety of Petroleum Engineers, , 2002. Disponível em: <https://doi.org/10.2118/77876-MS>

[51] FENG, Q. et al. **A Visual Micro-Model Study: The Mechanism of Water Alternative Gas Displacement in Porous MediaSPE/DOE Symposium on Improved Oil Recovery**Tulsa, OklahomaSociety of Petroleum Engineers, , 2004. Disponível em: <https://doi.org/10.2118/89362-MS>

[52] NOURANI, M. et al. **Laboratory Studies of MEOR in the Micromodel as a Fractured SystemEastern Regional Meeting**Lexington, Kentucky USASociety of Petroleum Engineers, , 2007. Disponível em: <https://doi.org/10.2118/110988-MS>

[53] SOUDMAND-ASLI, A. et al. The in situ microbial enhanced oil recovery in fractured porous media. **Journal of Petroleum Science and Engineering**, v. 58, p. 161–172, 1 Aug. 2007.

[54] SAYEGH, S. G.; FISHER, D. B. **Enhanced Oil Recovery by CO Flooding in Homogeneous and Heterogeneous 2D MicromodelsCanadian International Petroleum Conference**Calgary, AlbertaPetroleum Society of Canada, , 2008. Disponível em: <https://doi.org/10.2118/2008-005>

[55] ARMSTRONG, R.; WILDENSCHILD, D. **Designer-Wet Micromodels for Studying Potential Changes in Wettability during Microbial Enhanced Oil RecoveryAGU Fall Meeting Abstracts**, 1 Dec. 2010.

[56] DOORWAR, S.; MOHANTY, K. K. **Viscous Fingering during Non-Thermal Heavy Oil RecoverySPE Annual Technical Conference and Exhibition**Denver, Colorado, USASociety of Petroleum Engineers, , 2011. Disponível em: <https://doi.org/10.2118/146841-MS>

[57] DONG, M.; LIU, Q.; LI, A. Displacement mechanisms of enhanced heavy oil recovery by alkaline flooding in a micromodel. **Particuology**, v. 10, 1 Jun. 2012.

[58] EMADI, A.; SOHRABI, M. **Visual Investigation of Oil Recovery by LowSalinity Water Injection: Formation of Water Micro-Dispersions and WettabilityAlterationSPE Annual Technical Conference and Exhibition**New Orleans, Louisiana, USASociety of Petroleum Engineers, , 2013. Disponível em:

<https://doi.org/10.2118/166435-MS>

[59] AMANI, H. Study of enhanced oil recovery by rhamnolipids in a homogeneous 2D micromodel. **Journal of Petroleum Science and Engineering**, v. 128, p. 212–219, 2015.

[60] MOHAJERI, M.; HEMMATI, M.; SHEKARABI, A. An experimental study on using a nanosurfactant in an EOR process of heavy oil in a fractured micromodel. **Journal of Petroleum Science and Engineering**, v. 126, p. 162–173, 1 Feb. 2015.

[61] SOHRABI, M. et al. **A Thorough Investigation of Mechanisms of Enhanced Oil Recovery by Carbonated Water InjectionSPE Annual Technical Conference and Exhibition**Houston, Texas, USASociety of Petroleum Engineers, , 2015. Disponível em: <https://doi.org/10.2118/175159-MS>

[62] AMIRIAN, T.; HAGHIGHI, M.; MOSTAGHIMI, P. Pore Scale Visualization of Low Salinity Water Flooding as an Enhanced Oil Recovery Method. **Energy & Fuels**, v. 31, 31 Oct. 2017.

[63] FREDRIKSEN, S. B. et al. Wettability Effects on Osmosis as an Oil-Mobilization Mechanism During Low-Salinity Waterflooding. **Petrophysics**, v. 58, n. 01, p. 28–35, 2017.

[64] LI, S. et al. **Silica Nanoparticles Suspension for Enhanced Oil Recovery: Stability Behavior and Flow VisualizationSPE Europec featured at 80th EAGE Conference and Exhibition**Copenhagen, DenmarkSociety of Petroleum Engineers, , 2018. Disponível em: <https://doi.org/10.2118/190802-MS>

[65] BARKHORDARI, V.; JAFARI, A. Experimental Investigation of the Base Fluid Miscibility Condition on the Oil Recovery Using Nanofluids Flooding. **Journal of Water and Environmental Nanotechnology**, v. 3, n. 1, p. 12–21, 1 Jan. 2018.

[66] MOHAJERI, M.; REZA RASAEI, M.; HEKMATZADEH, M. Experimental study on using SiO2 nanoparticles along with surfactant in an EOR process in micromodel. **Petroleum Research**, v. 4, n. 1, p. 59–70, 2019.

[67] BARTELS, W.-B. et al. Fast X-Ray Micro-CT Study of the Impact of Brine Salinity on the Pore-Scale Fluid Distribution During Waterflooding. **Petrophysics**, v. 58, n. 01, p. 36–47, 2017.

[68] BARTELS, W.-B. et al. Oil Configuration Under High-Salinity and Low-Salinity Conditions at Pore Scale: A Parametric Investigation by Use of a Single-Channel Micromodel. **SPE Journal**, v. 22, n. 05, p. 1362–1373, 2017.

[69] ALKHATIB, A.; ALSHEHRI, A.; HAN, M. **Generating a three-dimensional**

micromodel of a porous rock sample, 2018.

[70] SEMWOGERERE; BBIJA, D.; WEEKS, E. R. **Confocal Microscopy**, 2005.

[71] CHEN, J.-D.; WILKINSON, D. Pore-Scale Viscous Fingering in Porous Media. **Physical Review Letters**, v. 55, n. 18, p. 1892–1895, 28 Oct. 1985.

[72] CORAPCIOGLU, Y. M.; CHOWDHURY, S.; ROOSEVELT, S. E. Micromodel visualization and quantification of solute transport in porous media. **Water Resources Research**, v. 33, n. 11, p. 2547–2558, 1 Nov. 1997.

[73] CHERAGHIAN, G.; HENDRANINGRAT, L. A review on applications of nanotechnology in the enhanced oil recovery part A: effects of nanoparticles on interfacial tension. **Nano Letters**, v. 6, 22 Jan. 2016.

[74] ZALLAGHI, M. et al. An Experimental Investigation of Nanoparticles Assisted Surfactant Flooding for Improving Oil Recovery in a Micromodel System. **Journal of Petroleum & Environmental Biotechnology**, v. 09, 7 Feb. 2018.

[75] D. TSAKIROGLOU, C.; AVRAAM, D. G. Fabrication of a new class of porous media models for visualization studies of multiphase flow process. **Journal of Materials Science**, v. 37, p. 353–363, 15 Jan. 2002.

[76] J. PYRAK-NOLTE, L.; G. W. COOK, N.; NOLTE, D. Fluid percolation through single fracture. **Geophysical Research Letters - GEOPHYS RES LETT**, v. 15, 1 Oct. 1988.

[77] D. NOLTE, D.; J. PYRAK-NOLTE, L.; G. W. COOK, N. **The Fractal Geometry of Flow Paths in Natural Fractures in Rock and the Approach to Percolation**, 1 Jan. 1989.

[78] D. NOLTE, D.; PYRAK-NOLTE, L. J. Stratified continuum percolation: Scaling geometry of hierarchical cascades. **Physical review. A**, v. 44, p. 6320–6333, 1 Dec. 1991.

[79] CHENG, J.-T. et al. Linking pressure and saturation through interfacial areas in porous media. **Physics Research Publications**, v. 31, 28 Apr. 2004.

[80] SANDNES, B. et al. Labyrinth Patterns in Confined Granular-Fluid Systems. **Physical review letters**, v. 99, p. 38001, 1 Aug. 2007.

[81] ZHANG, Q.; RAOOF, A.; HASSANIZADEH, S. Pore-Scale Study of Flow Rate on Colloid Attachment and Remobilization in a Saturated Micromodel. **Journal of Environment Quality**, v. 44, p. 1376, 1 Sep. 2015.

[82] KESTEN, H. **Percolation theory for mathematicians**: Progress in probability and statistics.Birkhäuser, , 1982. Disponível em:

<https://books.google.com.br/books?id=NqzvAAAAMAAJ>

[83] HELBA, A. A. et al. Percolation Theory of Two-Phase Relative Permeability. **SPE Reservoir Engineering**, v. 7, n. 01, p. 123–132, 1992.

[84] HU, X. et al. **Physics of Petroleum Reservoirs**, 1 Jan. 2017.

[85] PARK, D. et al. **Design and Fabrication of Rock-Based MicromodelASME International Mechanical Engineering Congress and Exposition, Proceedings (IMECE)**, 9 Nov. 2012.

[86] GEORGIADIS, A. et al. Pore-Scale Micro-CT Imaging: Cluster Size Distribution During Drainage and Imbibition. **Energy Procedia**, v. 23, p. 521–526, 2012.

[87] BOGGS, S. **Petrology of sedimentary rocks, second editionPetrology of Sedimentary Rocks, Second Edition**, 1 Jan. 2009.

[88] R.L., F.; W.C., W. Brazos River bar [Texas]; a study in the significance of grain size parameters. **Journal of Sedimentary Research**, v. 27, n. 3, p. 3–26, 1957.

[89] C BEARD, D.; K WEYL, P. Influence of Texture on Porosity and Permeability of Unconsolidated Sand. **AAPG Bulletin**, v. 57, p. 349–369, 1 Feb. 1973.

[90] ROCCA, V. et al. Current and Future Nanotech Applications in the Oil Industry. **American Journal of Applied Sciences**, v. 9, p. 784–793, 1 Jan. 2012.

[91] ZAMAN, M. S.; ISLAM, M. R.; MOKHATAB, S. Nanotechnology Prospects in the Petroleum Industry. **Petroleum Science and Technology**, v. 30, n. 10, p. 1053–1058, 30 Mar. 2012.

[92] YANG, J. et al. Advances of Nanotechnologies in Oil and Gas Industries. **Energy, Exploration & Exploitation**, v. 33, p. 639–657, 1 Oct. 2015.

[93] OGOLO, N. A.; OLAFUYI, O. A.; ONYEKONWU, M. O. **Enhanced Oil Recovery Using NanoparticlesSPE Saudi Arabia Section Technical Symposium and Exhibition**Al-Khobar, Saudi ArabiaSociety of Petroleum Engineers, , 2012. Disponível em: <https://doi.org/10.2118/160847-MS>

[94] MAHDI, R. et al. Review of convection heat transfer and fluid flow in porous media with nanofluid. **Renewable and Sustainable Energy Reviews**, v. 41, p. 715–734, 31 Jan. 2015.

[95] NEGIN, C.; SAEEDI, A.; XIE, Q. Application of nanotechnology for enhancing oil recovery – A review. **Petroleum**, v. 2, 1 Nov. 2016.

[96] CHERAGHIAN, G.; HENDRANINGRAT, L. A review on applications of nanotechnology in the enhanced oil recovery part B: Effects of nanoparticles on flooding. **Nano Letters**, v. 6, 9 Nov. 2015.

[97] DANESHAZARIAN, R. et al. Nanofluid flow and heat transfer in porous media: A review of the latest developments. **International Journal of Heat and Mass Transfer**, v. 107, 8 Dec. 2016.

[98] CHANG, H. L. et al. Advances in Polymer Flooding and Alkaline/Surfactant/Polymer Processes as Developed and Applied in the People's Republic of China. **Journal of Petroleum Technology**, v. 58, n. 02, p. 84–89, 2006.

[99] AHMADI, Y. et al. Comprehensive Water–Alternating-Gas (WAG) injection study to evaluate the most effective method based on heavy oil recovery and asphaltene precipitation tests. **Journal of Petroleum Science and Engineering**, v. 133, 16 May 2015.

[100] ALOMAIR, O. A.; MATAR, K. M.; ALSAEED, Y. H. **Nanofluids Application for Heavy Oil RecoverySPE Asia Pacific Oil & Gas Conference and Exhibition**Adelaide, AustraliaSociety of Petroleum Engineers, , 2014. Disponível em: <https://doi.org/10.2118/171539-MS>

[101] HU, L.; CHEN, M. Preparation of ultrafine powder: The frontiers of chemical engineering. **Materials Chemistry and Physics**, v. 43, p. 212–219, 1 Mar. 1996.

[102] MANDAL, A. et al. **Characterization of Surfactant Stabilized Nanoemulsion and Its Use in Enhanced Oil RecoverySPE International Oilfield Nanotechnology Conference and Exhibition**Noordwijk, The NetherlandsSociety of Petroleum Engineers, , 2012. Disponível em: <https://doi.org/10.2118/155406-MS>

[103] HASHEMI, R.; NASSAR, N.; PEREIRA-ALMAO, P. Nanoparticle technology for heavy oil in-situ upgrading and recovery enhancement: Opportunities and challenges. **Applied Energy**, v. 133, p. 374–387, 18 Jul. 2014.

[104] LEE, S. P. et al. Measuring Thermal Conductivity of Fluids Containing Oxide Nanoparticles. **Journal of Heat Transfer**, v. 121, 1 May 1999.

[105] DEVENDIRAN, D. K.; AMIRTHAM, V. A. A review on preparation, characterization, properties and applications of nanofluids. **Renewable and Sustainable Energy Reviews**, v. 60, p. 21–40, 2016.

[106] ROBINS, M.; FILLERY-TRAVIS, A. Colloidal dispersions. Edited by W. B. Russel, D. A. Saville & W. R. Schowalter, Cambridge University Press, Cambridge, UK, 1989, xvii + 506 pp., price: £60.00. ISBN 0 521 34188 4. **Journal of Chemical Technology & Biotechnology**, v. 54, n. 2, p. 201–202, 1 Jan. 1992.

[107] WEN, D.; DING, Y. Experimental investigation into the pool boiling heat transfer of aqueous based γ-alumina nanofluids. **Journal of Nanoparticle Research**, v. 7, n. 2,

p. 265–274, 2005.

[108] YU, H. et al. Optimizing sonication parameters for dispersion of single-walled carbon nanotubes. **Chemical Physics**, v. 408, p. 11–16, 2012.

[109] RUAN, B.; M JACOBI, A. Ultrasonication effects on thermal and rheological properties of carbon nanotube suspensions. **Nanoscale research letters**, v. 7, p. 127, 14 Feb. 2012.

[110] M. MCELFRESH, P.; OLGUIN, C.; ECTOR, D. **The Application of Nanoparticle Dispersions To Remove Paraffin and Polymer Filter Cake Damage**, 1 Jan. 2012.

[111] AVEYARD, R.; BINKS, B.; H CLINT, J. Emulsions Stabilised Solely by Colloidal Particles. **Advances in Colloid and Interface Science**, v. 100, p. 503–546, 1 Feb. 2003.

[112] HENDRANINGRAT, L.; LI, S.; TORSÆTER, O. **Effect of Some Parameters Influencing Enhanced Oil Recovery Process using Silica Nanoparticles: An Experimental Investigation**, 16 Sep. 2013.

[113] EL-DIASTY, A. **The Potential of Nanoparticles to Improve Oil Recovery in Bahariya Formation, Egypt: An Experimental Study**, 1 Aug. 2015.

[114] SKAUGE, T.; SPILDO, K.; SKAUGE, A. **Nano-sized Particles For EORSPE Improved Oil Recovery Symposium**Tulsa, Oklahoma, USASociety of Petroleum Engineers, , 2010. Disponível em: <https://doi.org/10.2118/129933-MS>

[115] HASHEMI, R.; NASSAR, N.; PEREIRA-ALMAO, P. Enhanced Heavy Oil Recovery by in Situ Prepared Ultradispersed Multimetallic Nanoparticles: A Study of Hot Fluid Flooding for Athabasca Bitumen Recovery. **Energy & Fuels**, v. 27, p. 2194−2201, 18 Apr. 2013.

[116] BETHEL, F. T.; CALHOUN, J. C. Capillary Desaturation in Unconsolidated Beads. **Journal of Petroleum Technology**, v. 5, n. 08, p. 197–202, 1953.

[117] OWENS, W. W.; ARCHER, D. L. The Effect of Rock Wettability on Oil-Water Relative Permeability Relationships. **Journal of Petroleum Technology**, v. 23, n. 07, p. 873–878, 1971.

[118] GIRALDO, J. et al. Wettability Alteration of Sandstone Cores by Alumina-Based Nanofluids. **Energy & Fuels**, v. 27, p. 3659–3665, 27 Jun. 2013.

[119] HENDRANINGRAT, L.; TORSÆTER, O. **Understanding Fluid-Fluid and Fluid-Rock Interactions in the Presence of Hydrophilic Nanoparticles at Various ConditionsSPE Asia Pacific Oil & Gas Conference and Exhibition**Adelaide,

AustraliaSociety of Petroleum Engineers, , 2014. Disponível em: <https://doi.org/10.2118/171407-MS>

[120] ROUSTAEI, A.; BAGHERZADEH, H. Experimental investigation of SiO2 nanoparticles on enhanced oil recovery of carbonate reservoirs. **Journal of Petroleum Exploration and Production Technology**, v. 5, 1 Mar. 2014.

[121] HENDRANINGRAT, L.; TORSÆTER, O. Metal oxide-based nanoparticles: revealing their potential to enhance oil recovery in different wettability systems. **Applied Nanoscience**, v. 5, n. 2, p. 181–199, 2015.

[122] KARIMI, A. et al. Wettability Alteration in Carbonates using Zirconium Oxide Nanofluids: EOR Implications. **Energy & Fuels**, v. 26, p. 1028–1036, 18 Jan. 2012.

[123] LAKE, L. W.; (U.S.), S. OF P. E. **Petroleum Engineering Handbook**Society of Petroleum Engineers, , 2006. Disponível em: <https://books.google.com.br/books?id=wS2XAAAACAAJ>

[124] ABU TARBOUSH, B.; HUSEIN, M. Adsorption of asphaltenes from heavy oil onto in situ prepared NiO nanoparticles. **Journal of colloid and interface science**, v. 378, p. 64–69, 19 Apr. 2012.

[125] KAZEMZADEH, Y. et al. Behavior of Asphaltene Adsorption onto the Metal Oxide Nanoparticle Surface and Its Effect on Heavy Oil Recovery. **Industrial & Engineering Chemistry Research**, v. 54, p. 233–239, 18 Dec. 2014.

[126] NASSAR, N.; HASSAN, A.; PEREIRA-ALMAO, P. Thermogravimetric studies on catalytic effect of metal oxide nanoparticles on asphaltene pyrolysis under inert conditions. **Journal of Thermal Analysis and Calorimetry**, v. 110, p. 1327–1332, 1 Dec. 2012.

[127] CHRISTIANSEN, R. L. **Two-phase Flow Through Porous Media: Theory, Art and Reality of Relative Permeability and Capillary Pressure**R.L. Christiansen, , 2001. Disponível em: <https://books.google.com.br/books?id=d4kOHQAACAAJ>

[128] AYATOLLAHI, S.; ZERAFAT, M. M. **Nanotechnology-Assisted EOR Techniques: New Solutions to Old ChallengesSPE International Oilfield Nanotechnology Conference and Exhibition**Noordwijk, The NetherlandsSociety of Petroleum Engineers, , 2012. Disponível em: <https://doi.org/10.2118/157094-MS>

[129] TERRY, R. E.; ROGERS, J. B.; CRAFT, B. C. **Applied Petroleum Reservoir Engineering**Prentice Hall, , 2015. Disponível em: <https://books.google.com.br/books?id=rNwRBAAAQBAJ>

[130] GREEN, D. W.; WILLHITE, G. P. **Enhanced Oil Recovery**: SPE textbook

series.Henry L. Doherty Memorial Fund of AIME, Society of Petroleum Engineers, , 1998. Disponível em: <https://books.google.com.br/books?id=0cUWAAAACAAJ>

[131] SHAH, R. D. **Application of Nanoparticle Saturated Injectant Gases for EOR of Heavy OilsSPE Annual Technical Conference and Exhibition**New Orleans, LouisianaSociety of Petroleum Engineers, , 2009. Disponível em: <https://doi.org/10.2118/129539-STU>

[132] SHEKHAWAT, D. S. et al. **Magnetic Recovery-Injecting Newly Designed Magnetic Fracturing Fluid with Applied Magnetic Field for EORSPE Asia Pacific Hydraulic Fracturing Conference**Beijing, ChinaSociety of Petroleum Engineers, , 2016. Disponível em: <https://doi.org/10.2118/181853-MS>

[133] WU, W.; HE, Q.; JIANG, C. Magnetic Iron Oxide Nanoparticles: Synthesis and Surface Functionalization Strategies. **Nanoscale research letters**, v. 3, p. 397–415, 1 Nov. 2008.

[134] KOTHARI, N. et al. **Application Of Ferrofluids For Enhanced Surfactant Flooding In IORSPE EUROPEC/EAGE Annual Conference and Exhibition**Barcelona, SpainSociety of Petroleum Engineers, , 2010. Disponível em: <https://doi.org/10.2118/131272-MS>

[135] AL-JABARI, M.; NASSAR, N.; HUSEIN, M. **Removal of asphaltenes from heavy oil by nickel nano and micro particle adsorbents**, 1 Sep. 2008.

[136] PATIL, G. E. et al. Preparation and characterization of SnO2 nanoparticles by hydrothermal route. **International Nano Letters**, v. 2, n. 1, p. 17, 2012.

[137] EHTESABI, H.; AHADIAN, M.; TAGHIKHANI, V. **Investigation of Diffusion and Deposition of TiO2 Nanoparticles in Sandstone Rocks for EOR Application**, 16 Jun. 2014.

[138] MOHD ZAID, H.; AHMAD, S.; YAHYA, N. The Effect of Zinc Oxide and Aluminum Oxide Nanoparticles on Interfacial Tension and Viscosity of Nanofluids for Enhanced Oil Recovery. **Advanced Materials Research**, v. 1024, p. 56–59, 1 Aug. 2014.

[139] YU, J. et al. **Transport Study of Nanoparticles for Oilfield ApplicationSPE International Conference on Oilfield Scale**Aberdeen, UKSociety of Petroleum Engineers, , 2010. Disponível em: <https://doi.org/10.2118/131158-MS>

[140] KANJ, M. Y.; RASHID, M. H.; GIANNELIS, E. **Industry First Field Trial of Reservoir NanoagentsSPE Middle East Oil and Gas Show and Conference**Manama, BahrainSociety of Petroleum Engineers, , 2011. Disponível em:

<https://doi.org/10.2118/142592-MS>

[141] RAAJIMAKERS, B. **Solute transport in porous media; An experimental pore-scale study using physical micromodels**. 2018. 32 f. Utrecht University, the Netherlands. 2018.

[142] CORPORATION, M. M. **CNC Mini-Mill**. Disponível em: <https://www.minitech.com/mini-mill4---features.html>.

[143] SELLIN, N.; CAMPOS, J. S. DE C. Surface composition analysis of PP films treated by corona discharge. **Materials Research**, v. 6, p. 163–166, 2003.

[144] LIN, W.-C.; MOHD RAZALI, N. A. Temporary Wettability Tuning of PCL/PDMS Micro Pattern Using the Plasma Treatments. **Materials (Basel, Switzerland)**, v. 12, n. 4, p. 644, 20 Feb. 2019.

[145] EDDINGTON, D.; PUCCINELLI, J.; J. BEEBE, D. Thermal Aging and Reduced Hydrophobic Recovery of Polydimethylsiloxane. **Sensors and Actuators B**, v. 114, p. 170–172, 1 Mar. 2006.

[146] NICOLINI, J. V.; FERRAZ, H.; BORGES, C. Effect of seawater ionic composition modified by nanofiltration on enhanced oil recovery in Berea sandstone. **Fuel**, v. 203, p. 222–232, 1 Sep. 2017.

[147] PITT, F. **Desenvolvimento de metodologia para polimerização do poliglicerolad ípico a partir do glicerol residual oriundo da produção de biodiesel**. 2010. Universidade Regional de Blumenau. 2010.

[148] ROTENBERG, Y.; BORUVKA, L.; NEUMANN, A. W. Determination of surface tension and contact angle from the shapes of axisymmetric fluid interfaces. **Journal of Colloid and Interface Science**, v. 93, n. 1, p. 169–183, 1983.

[149] HASSENKAM, T. et al. **Observation of the Low Salinity Effect by Atomic Force Adhesion Mapping on Reservoir SandstonesSPE Improved Oil Recovery Symposium**Tulsa, Oklahoma, USASociety of Petroleum Engineers, , 2012. Disponível em: <https://doi.org/10.2118/154037-MS>

[150] BUTT, H. J.; GRAF, K.; KAPPL, M. **Physics and Chemistry of Interfaces**Wiley, , 2006. Disponível em: <https://books.google.com.br/books?id=zODc90UDk4sC>

[151] LIN, Y.-J. et al. Characterizing Asphaltene Deposition in the Presence of Chemical Dispersants in Porous Media Micromodels. **Energy & Fuels**, v. 31, 19 Oct. 2017.

[152] MONTEMAGNO, C.; G. GRAY, W. Photoluminescent Volumetric Imaging: A

Technique for the Exploration of Multiphase Flow and Transport in Porous Media. **Geophysical Research Letters - GEOPHYS RES LETT**, v. 22, p. 425–428, 15 Feb. 1995.

[153] KEANE, R.; ADRIAN, R. Theory of cross-correlation analysis of PIV images. **Applied Scientific Research**, v. 49, p. 191–215, 7 Jan. 1992.

[154] W. GRATE, J. et al. A note on the visualization of wetting film structures and a nonwetting immiscible fluid in a pore network micromodel using a solvatochromic dye. **Water Resources Research - WATER RESOUR RES**, v. 46, 1 Nov. 2010.

[155] ISLAM, M. R.; KHAN, M. I. **The Petroleum Engineering Handbook: Sustainable Operations**Elsevier Science, , 2008. Disponível em: <https://books.google.com.br/books?id=ONy-AQAACAAJ>

[156] VERWEY, E. J. W. Theory of the Stability of Lyophobic Colloids. **The Journal of Physical and Colloid Chemistry**, v. 51, n. 3, p. 631–636, 1 Mar. 1947.

[157] ANTONIO ALVES JÚNIOR, J.; BALDO, J. The Behavior of Zeta Potential of Silica Suspensions. **New Journal of Glass and Ceramics**, v. 04, p. 29–37, 1 Jan. 2014.

[158] ROUSTAEI, A.; SAFFARZADEH, S.; MOHAMMADI, M. An evaluation of modified silica nanoparticles' efficiency in enhancing oil recovery of light and intermediate oil reservoirs. **Egyptian Journal of Petroleum**, v. 22, 1 Dec. 2013.

[159] BARATI, N.; ZARGARTALEBI, M.; KHARRAT, R. Influences of Hydrophilic and Hydrophobic silica Nanoparticles on anionic surfactant Properties: Interfacial and adsorption behaviors. **Journal of Petroleum Science and Engineering**, v. 119, 1 Jul. 2014.

[160] ESHRAGHI S, E. et al. Investigating Effect of SiO2 Nanoparticle and Sodium-Dodecyl-Sulfate Surfactant on Surface Properties: Wettability Alteration and IFT Reduction. **Journal of Petroleum & Environmental Biotechnology**, v. 08, 1 Jan. 2017.

[161] SADATSHOJAEI, E. et al. Effects of low-salinity water coupled with silica nanoparticles on wettability alteration of dolomite at reservoir temperature. **Petroleum Science and Technology**, v. 34, p. 1345–1351, 2 Aug. 2016.

[162] ZHOU, J.; ELLIS, A.; VOELCKER, N. Recent Developments in PDMS Surface Modification for Microfluidic Devices. **Electrophoresis**, v. 31, p. 2–16, 1 Jan. 2010.

[163] LI, R. et al. Experimental Investigation of Silica-based Nanofluid Enhanced Oil Recovery: The Effect of Wettability Alteration. **Energy & Fuels**, v. 31, 2 Dec. 2016.

A. Micromodel characterization

In order to characterize the manufactured micromodels, additional 2D and 3D microscope images have been captured for the selected regions described in the Results and Discussion section. For example, Fig. A.1 and Fig. A.2 show the 2D microscope and CAD designed images for the upper right corner of the micromodel pore-network, Fig. A.3 and Fig. A.4 show the 2D microscope and CAD designed images for the bottom left corner; while Fig. A.5 and Fig. A.6 show the 2D microscope and CAD designed images for the bottom right corner. It can be seen that a slightly difference appears when comparing the 2D to CAD images of these regions. However, this difference might be due to the differences in size of the line draw from the microscope to the line in the CAD image. Additional 3D images of these three regions are also being shown (Fig. A.7, Fig. A.8 and Fig. A.9). It can be observed that the height of the fabricated micromodel is almost equal to the height of the designed CAD template.

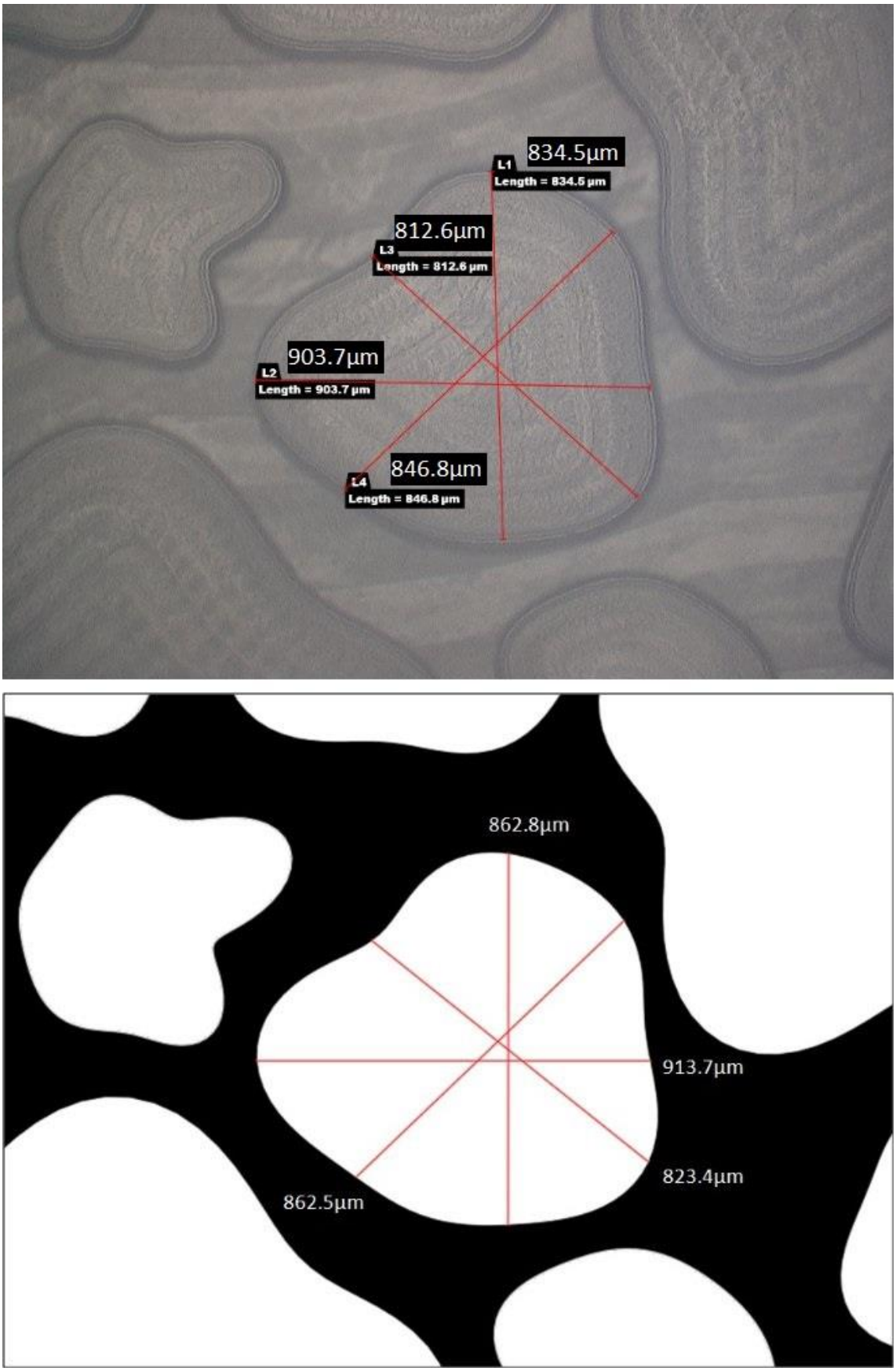

Fig. A.1 – Micromodel microscope image and CAD image of the selected region in the upper right corner showing the inner dimensions of the grain.

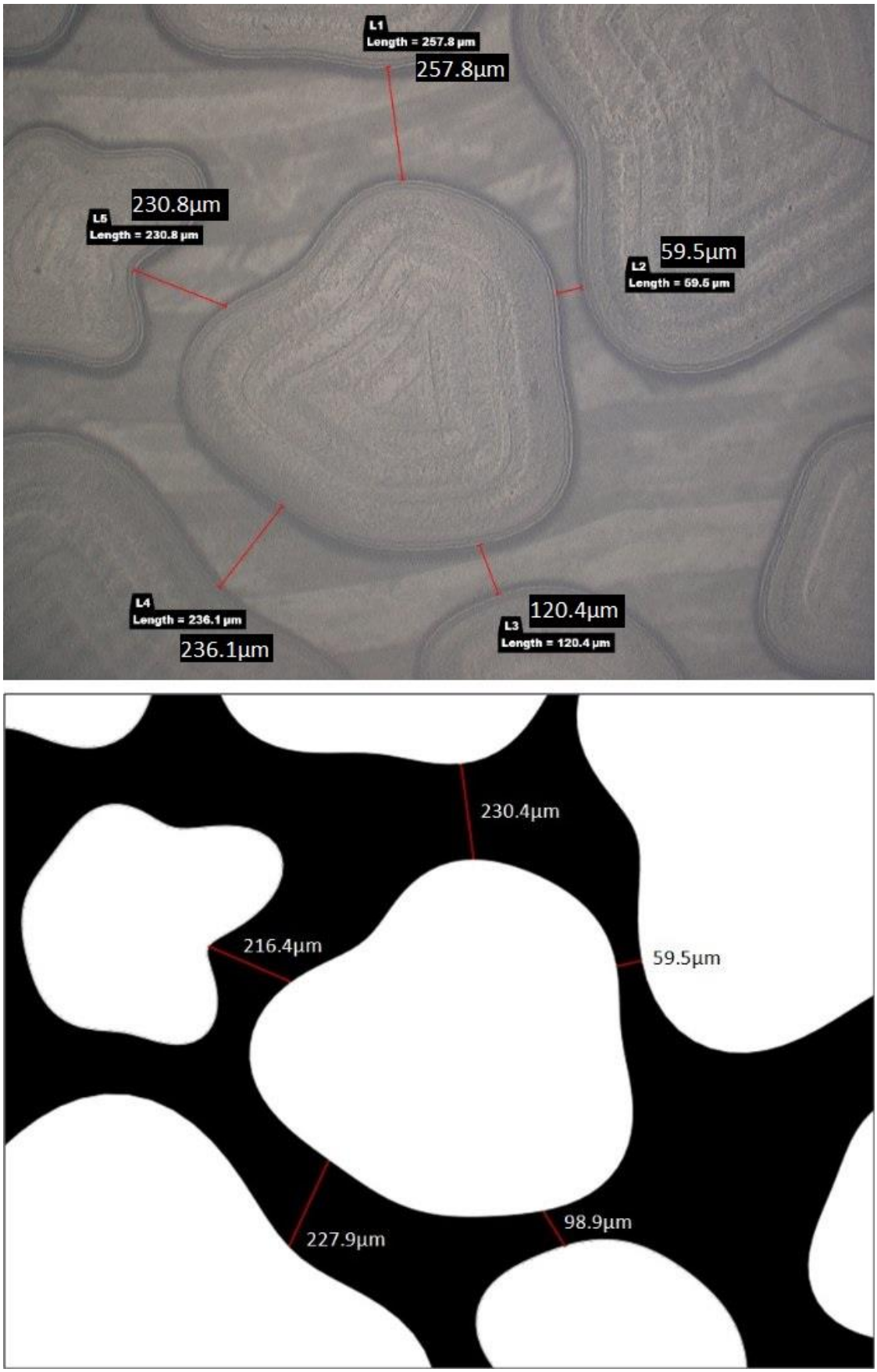

Fig. A.2 – Micromodel microscope image and CAD image of the selected region in the upper right corner showing the inner dimensions of the grain.

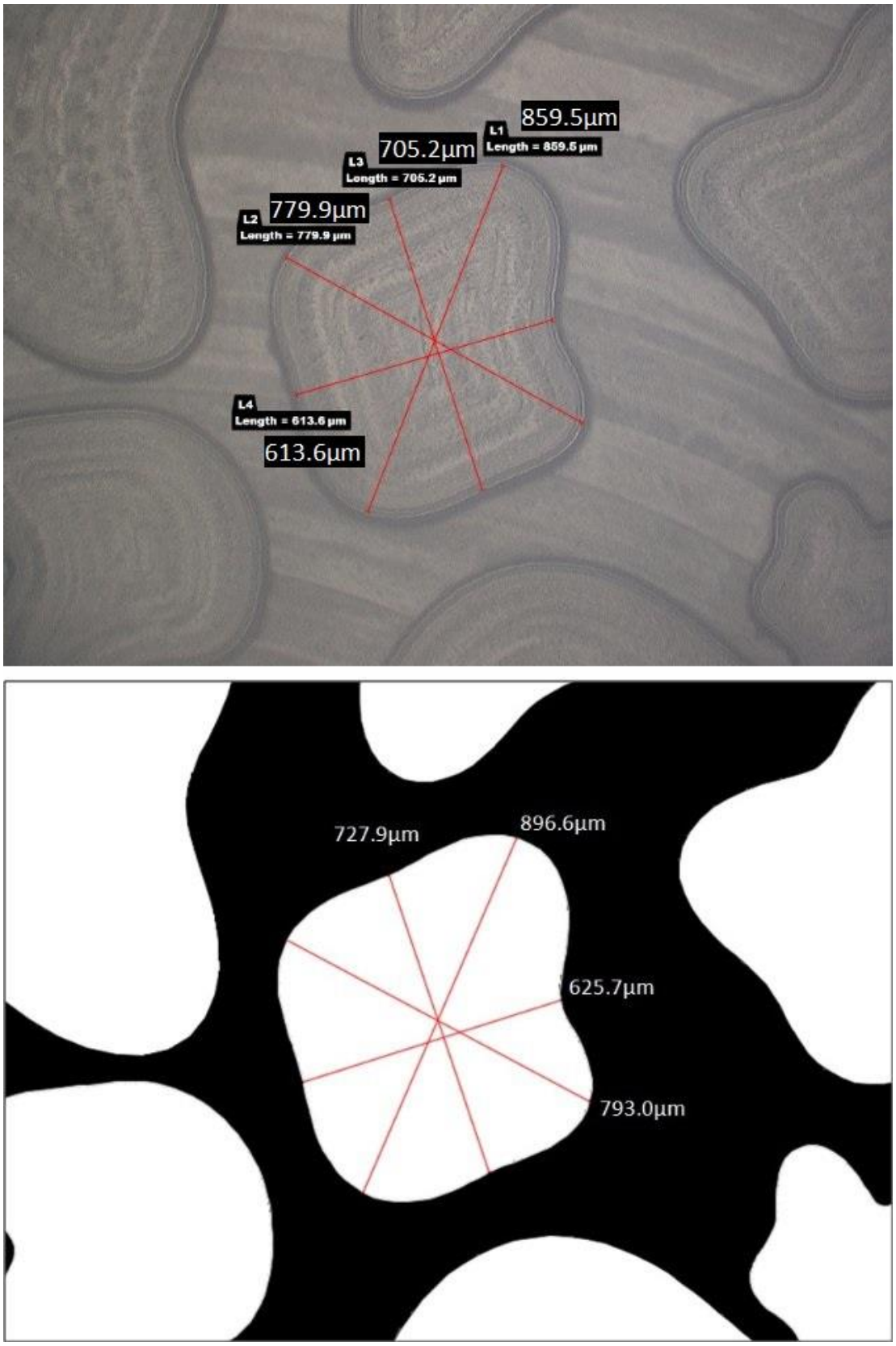

Fig. A.3 – Micromodel microscope image and CAD image of the selected region in the bottom left corner showing the inner dimensions of the grain.

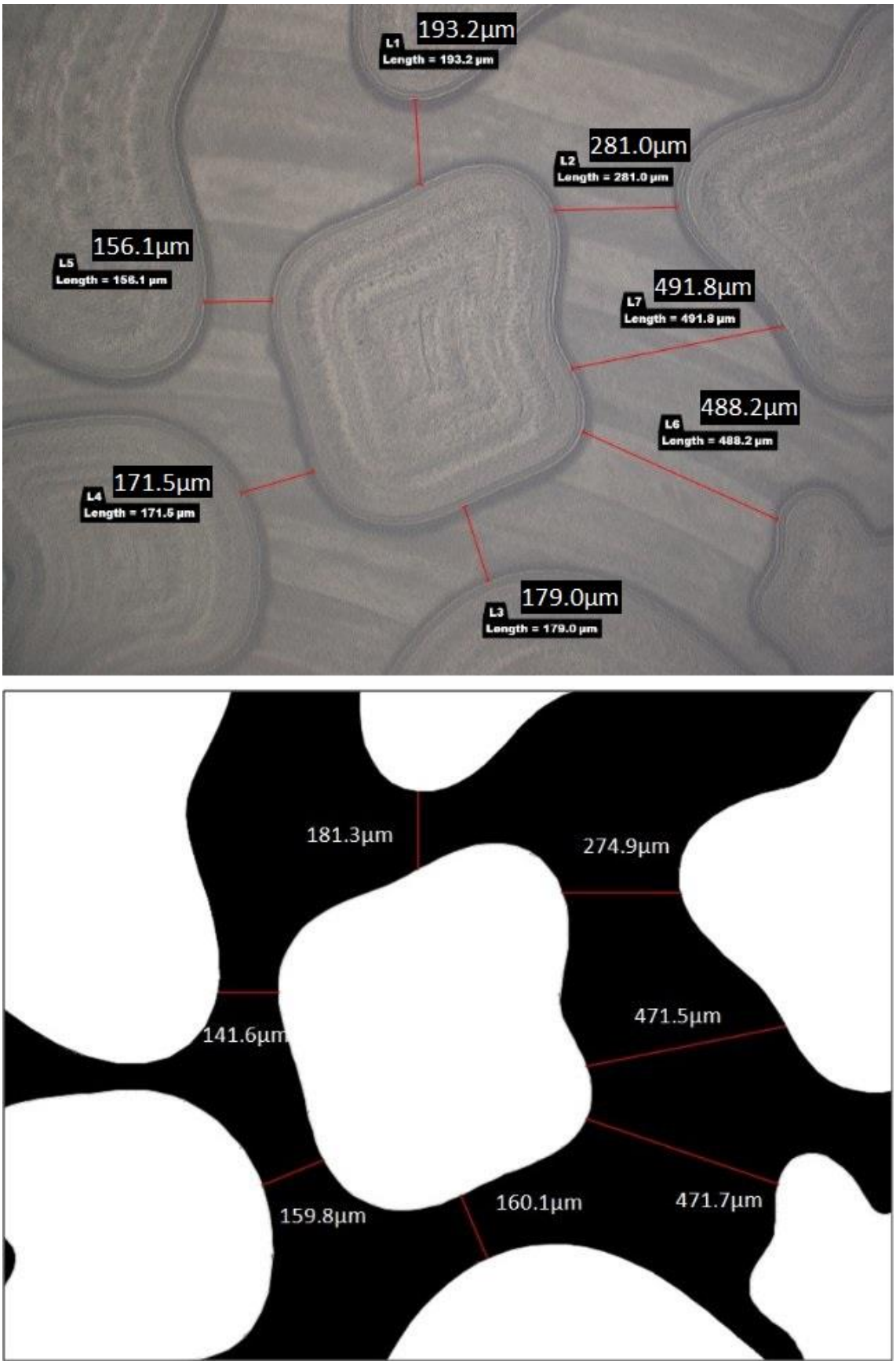

Fig. A.4 – Micromodel microscope image and CAD image of the selected region in the bottom left corner showing the pore dimensions between adjacent grains.

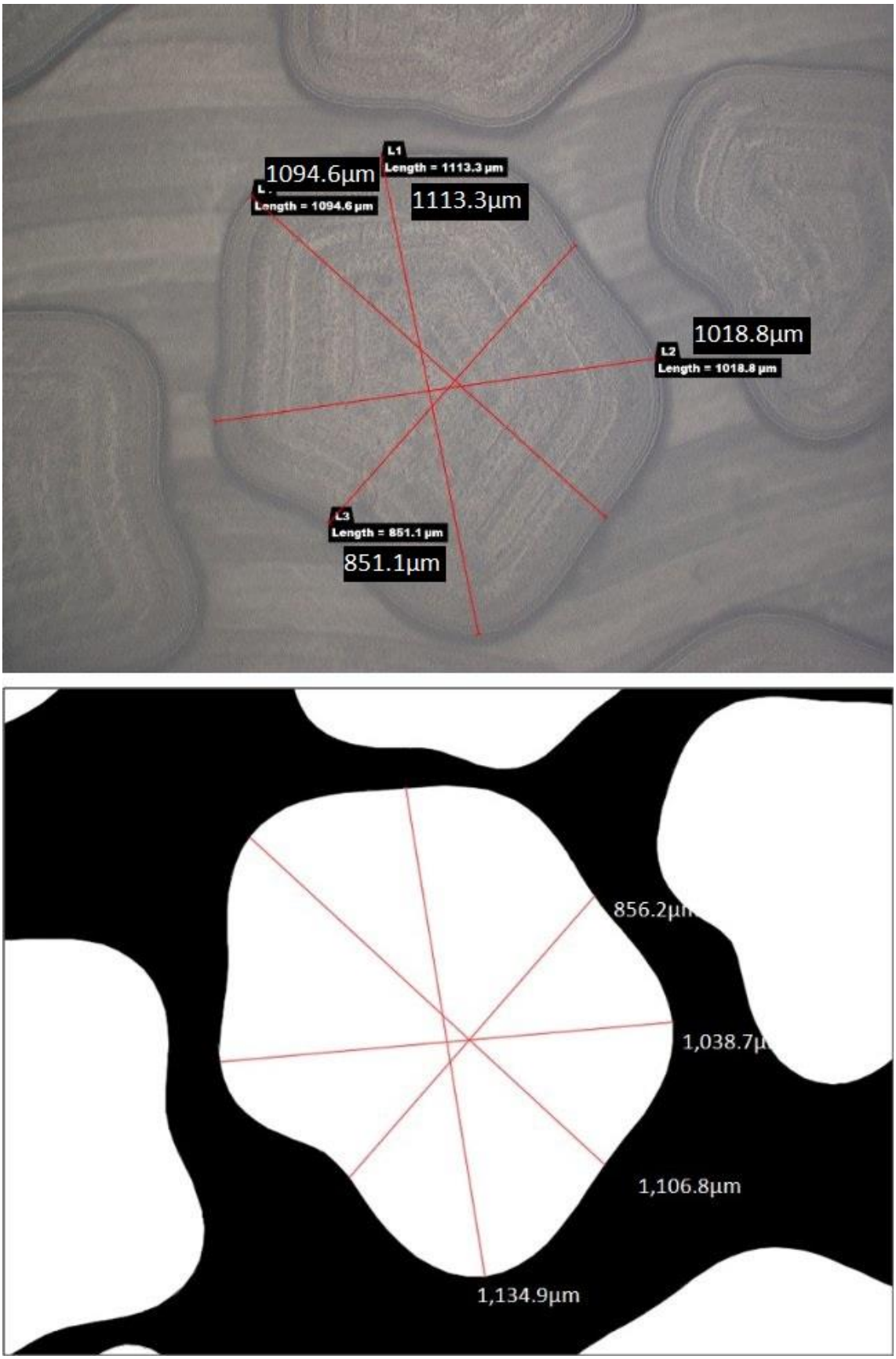

Fig. A.5 – Micromodel microscope image and CAD image of the selected region in the bottom right corner showing the inner dimensions of the grain.

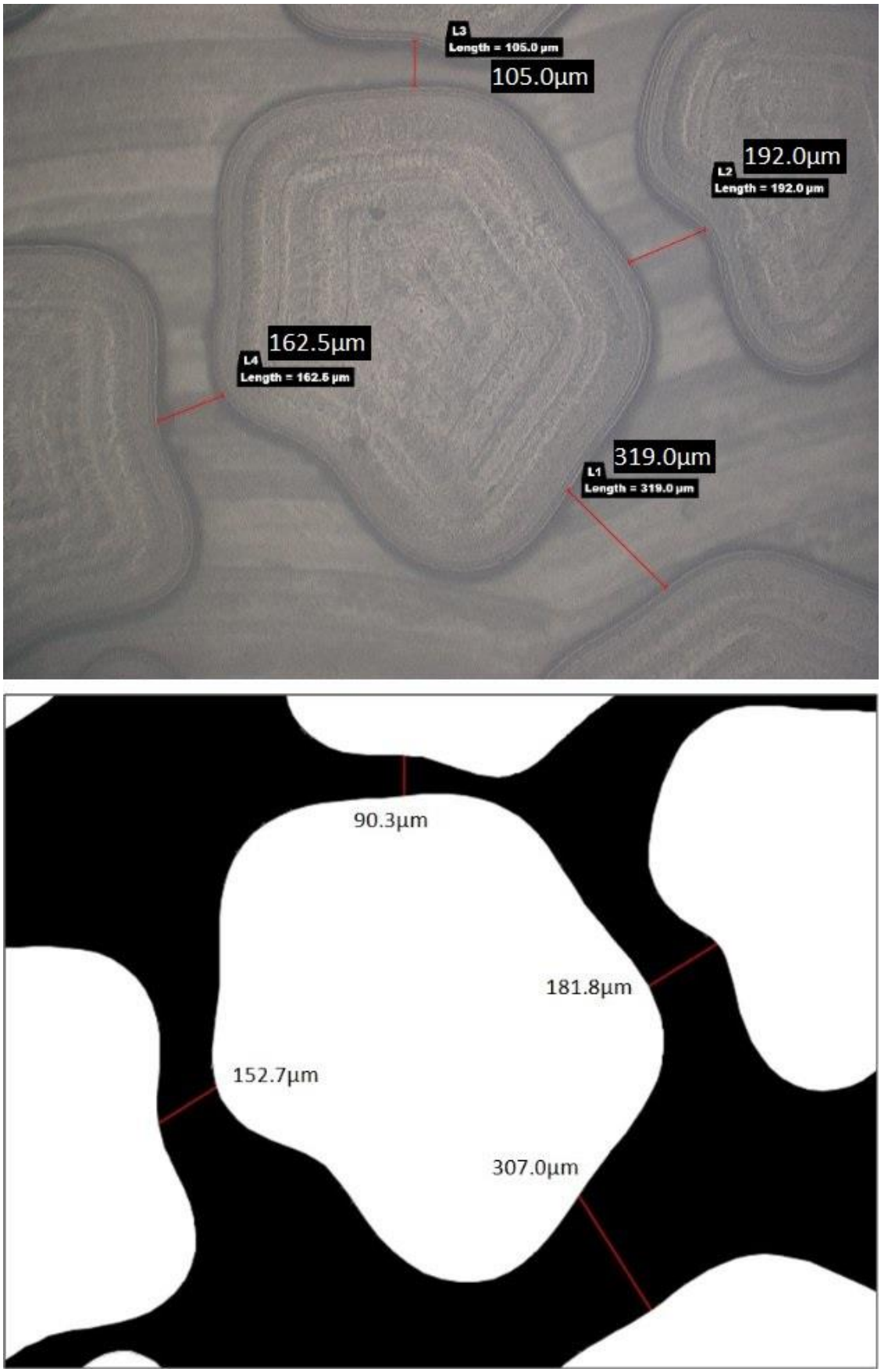

Fig. A.6 – Micromodel microscope image and CAD image of the selected region in the bottom right corner showing the pore dimensions between adjacent grains.

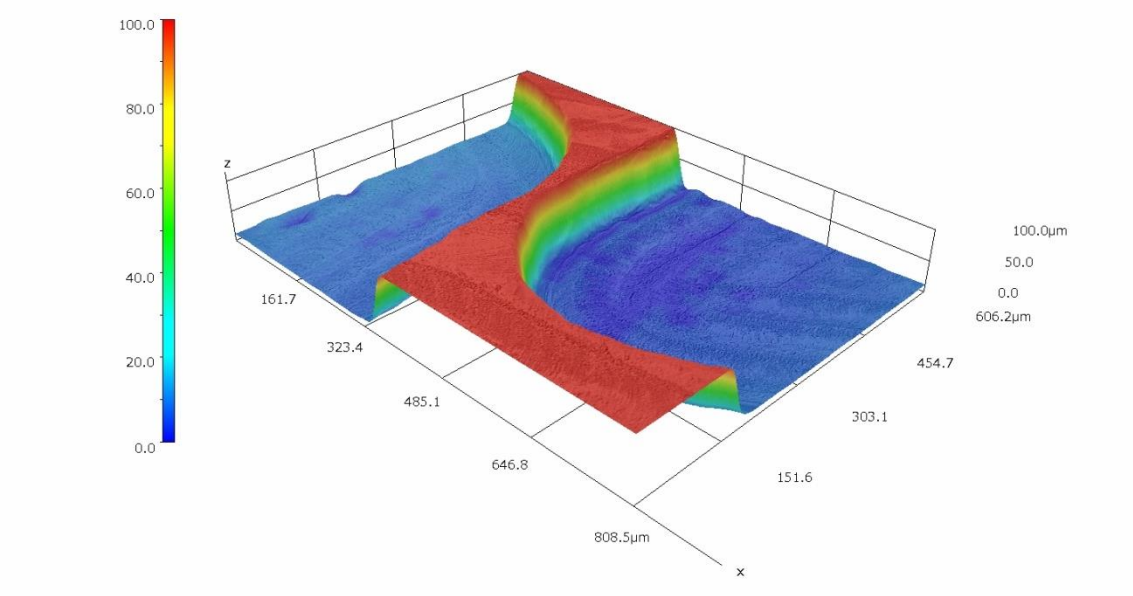

Fig. A.7 – Micromodel 3D microscope image of the selected region in the upper right corner. Two adjacent grains are being represented in blue, while the pore space is represented in red. The scale bar is in micrometers. The image shows that the fabricated height of the micromodel (100µm) in this region is equal to the designed height (100µm).

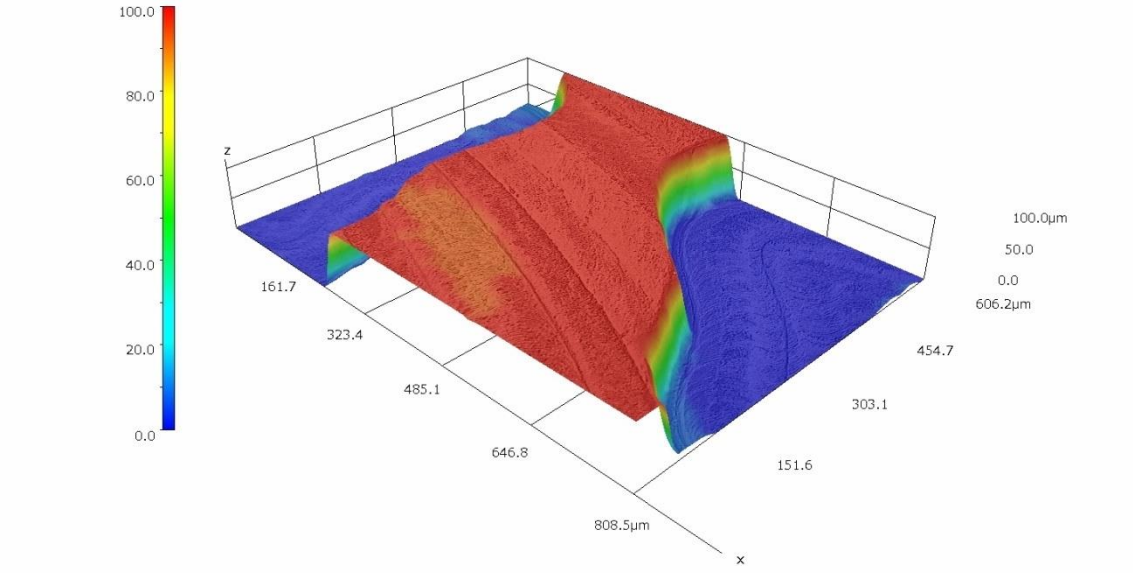

Fig. A.8 – Micromodel 3D microscope image of the selected region in the bottom left corner. Two adjacent grains are being represented in blue, while the pore space is represented in red. The scale bar is in micrometers. The image shows that the fabricated height of the micromodel (100µm) in this region is equal to the designed height (100µm).

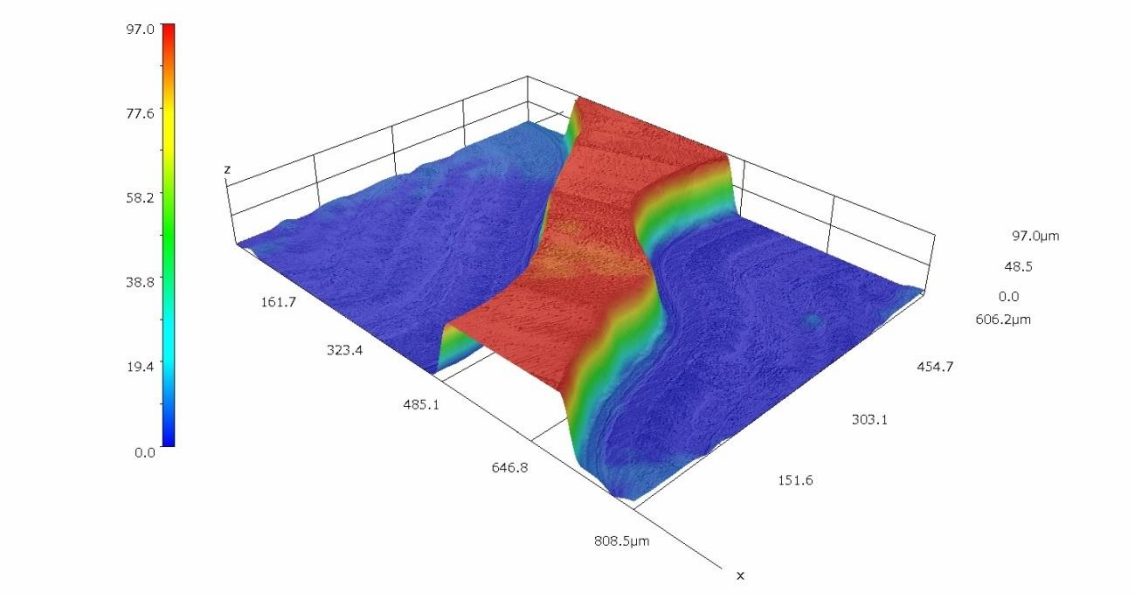

Fig. A.9 – Micromodel 3D microscope image of the selected region in the bottom right corner. Two adjacent grains are being represented in blue, while the pore space is represented in red. The scale bar is in micrometers. The image shows that the fabricated height of the micromodel (97µm) in this region is almost equal to the designed height (100µm).

B. Interfacial and surface measurements

Interfacial tension (IFT) images obtained by the goniometer instrument are being here represented. Fig. B.1 refers to the IFT images for the SiO_2 NPs/oil systems without biosurfactant addition, while Fig. B.2 refers to the same systems including biosurfactant. Differences in the shape of the oil drops within a system may not be observed, although a slight difference between the shape of the oil drops without and with surfactant addition in the NPs can be observed. With biosurfactant (Fig. C.2), the oil drops are slightly more flattened when compared to Fig. B.1. This behavior is an indication of reduction in the interfacial tension between the fluid phases. Moreover, Fig. B.3 shows contact angle measurements for the oil/nanofluids/PDMS systems. By observing these images, it is not possible to identify a significant difference in the wetting tendency of PDMS with nanofluid concentration.

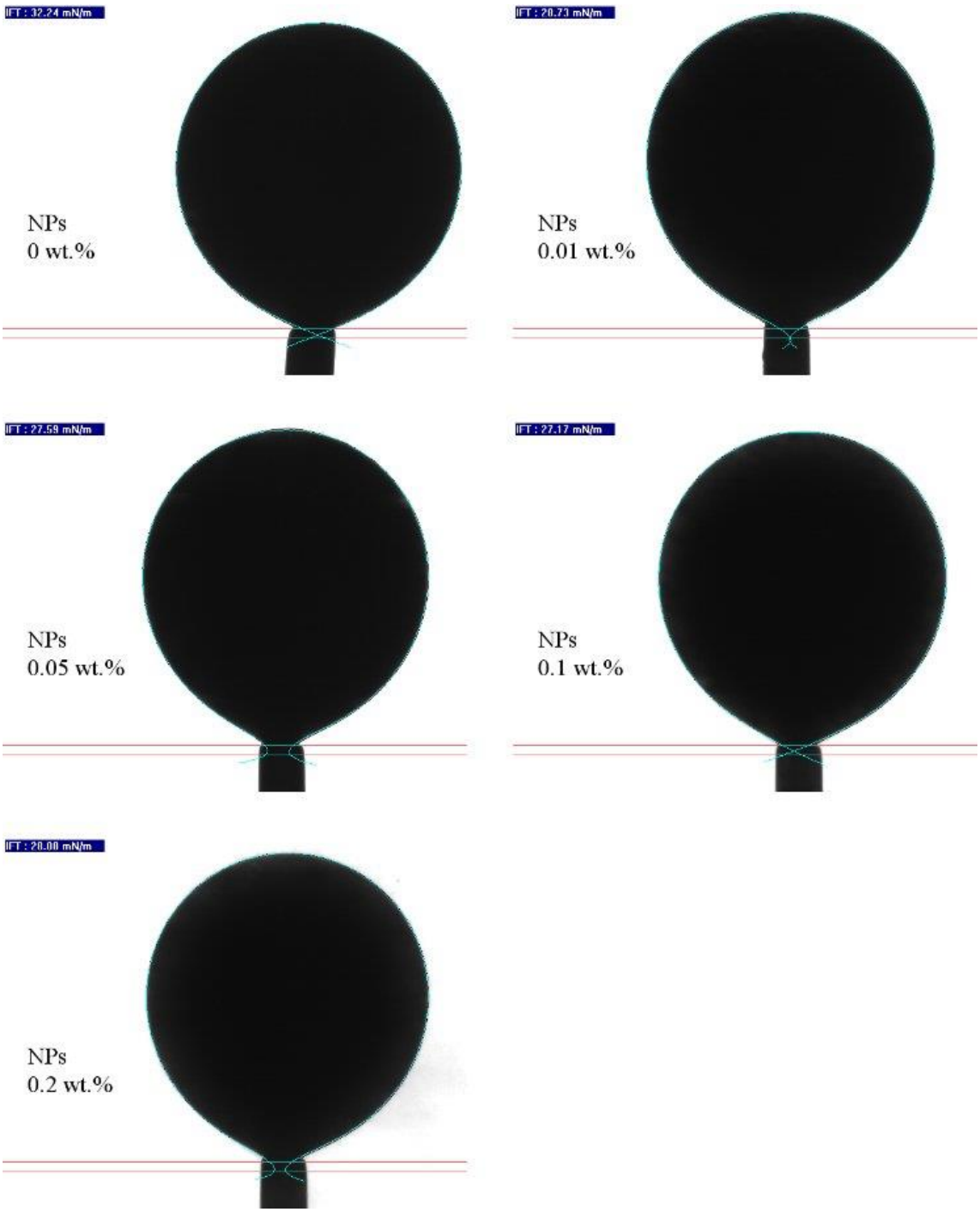

Fig. B.1 – Drop images between crude oil/nanofluids and their associated IFT values obtained from goniometer measurements.

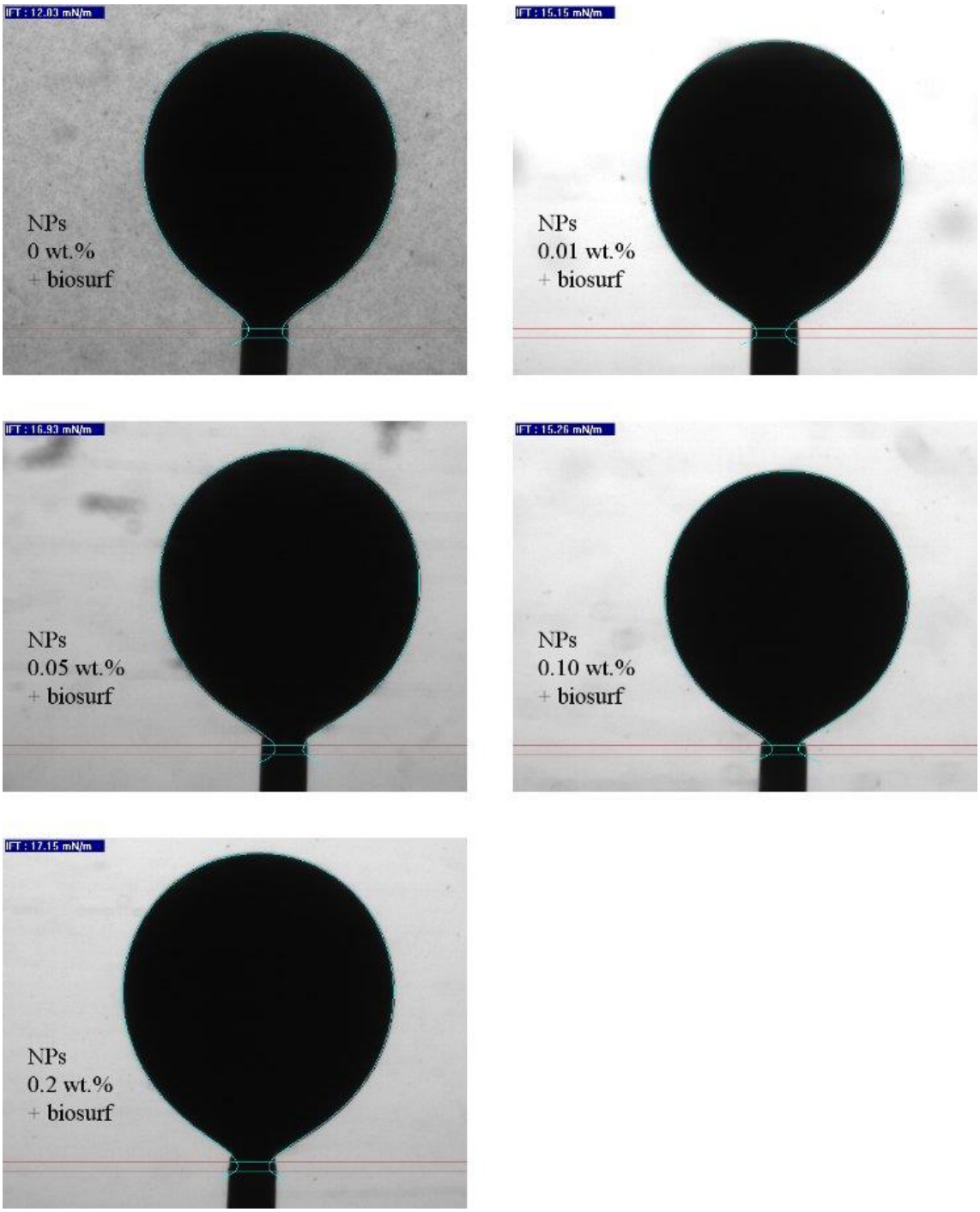

Fig. B.2 – Drop images between crude oil/nanofluids with biosurfactant and their associated IFT values obtained from goniometer measurements.

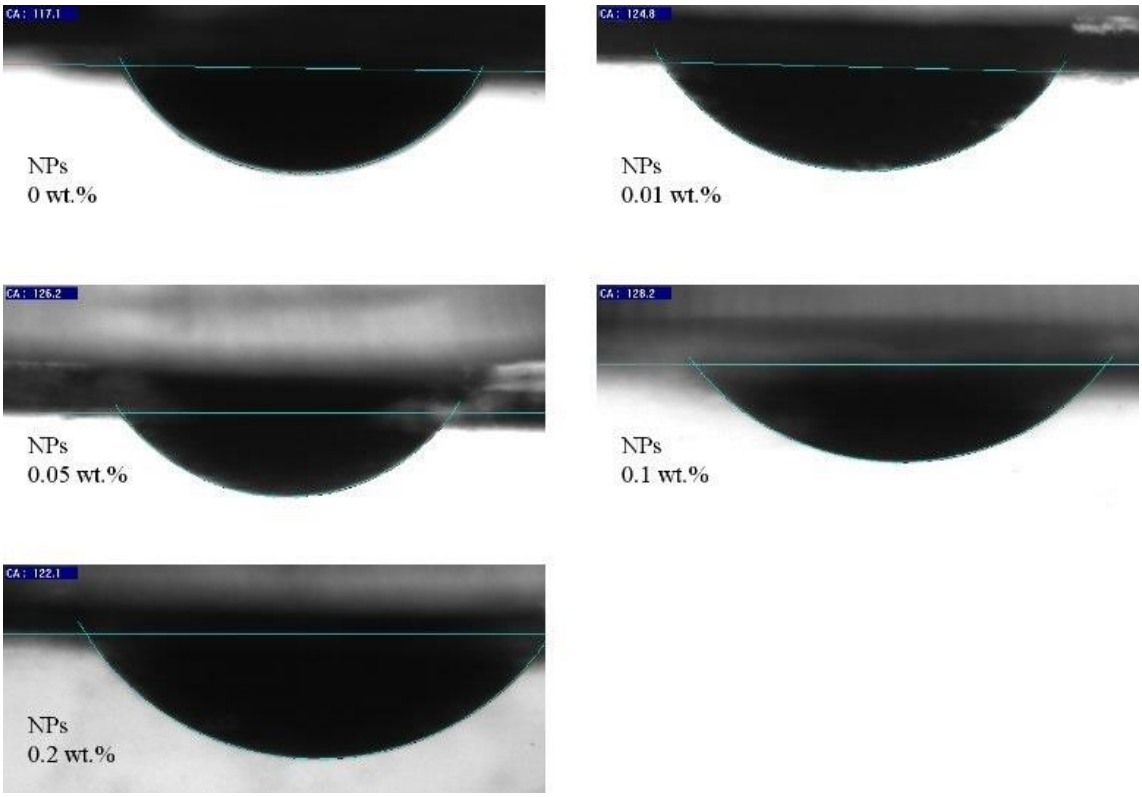

Fig. B.3 – Drop images for crude oil/PDMS/nanofluid systems and their associated CA values obtained from goniometer measurements.

C. Flow images

Flow images have been captured after each PV injected during the secondary and tertiary recovery experiments. Regarding the tertiary recovery experiment, Fig. C.1 and Fig. C.2 contain the flow images for brine flooding and nanofluid flooding, respectively. Fig. C.3 and Fig. C.4 contain the flow images for the secondary recovery experiment. Stacked images related to tertiary recovery (Fig. C.5 and Fig. C.6) and secondary recovery (Fig. C.7) are also being shown. Finally, the segmented images for the both experiments are being represented in Fig. C.8 to Fig. C.11.

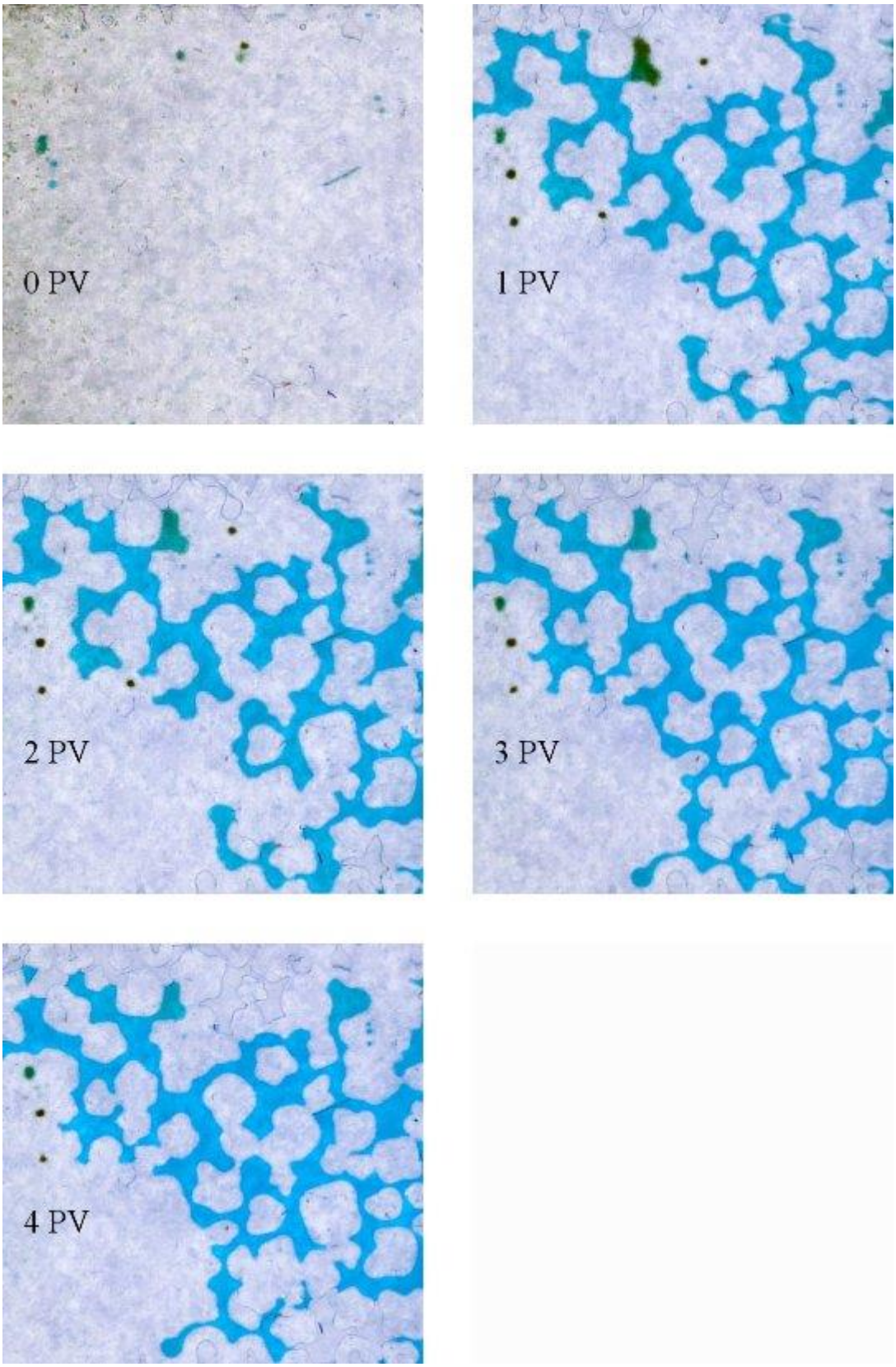

Fig. C.1 – Flow images for brine flooding in the tertiary recovery experiment.

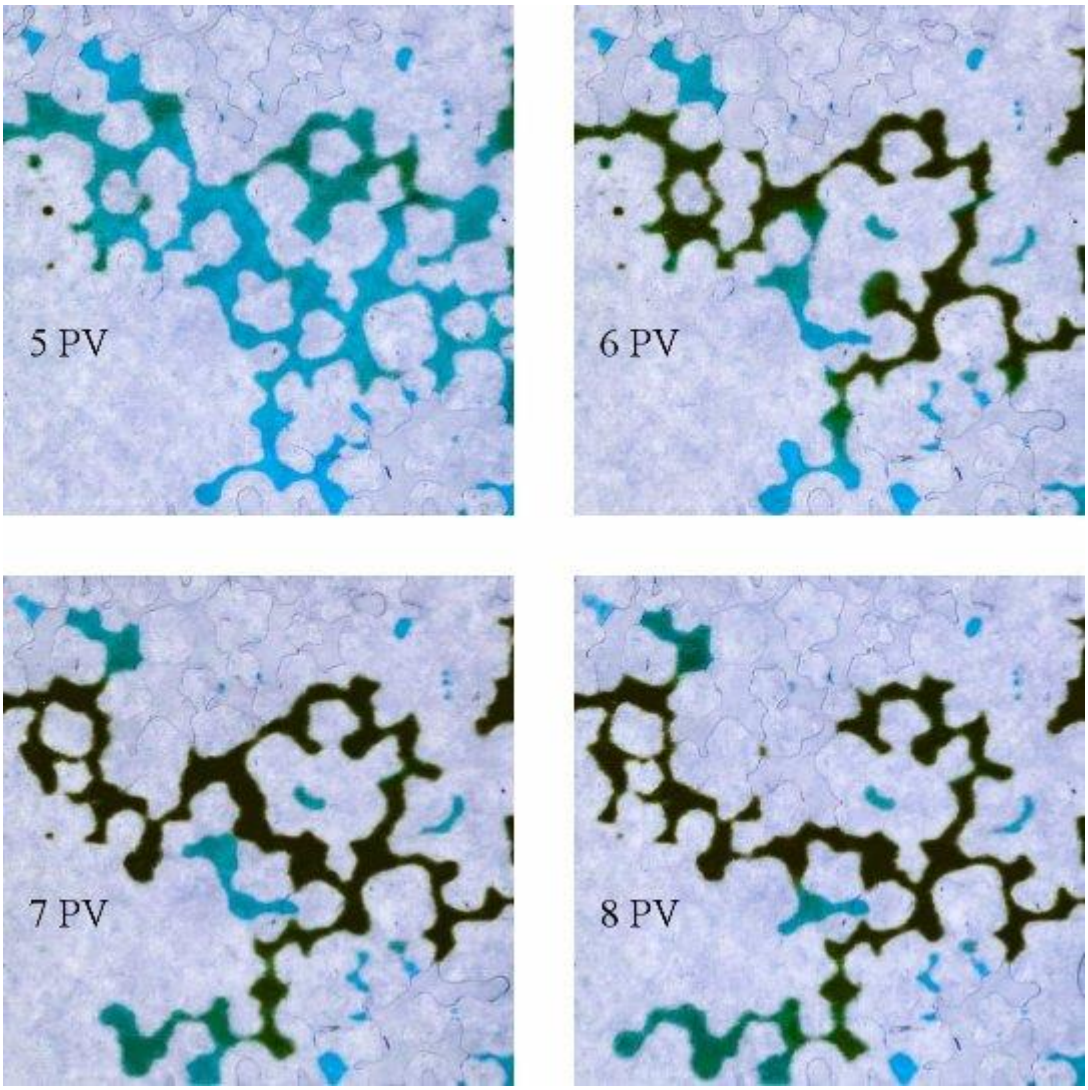

Fig. C.2 – Flow images for nanofluid flooding in the tertiary recovery experiment.

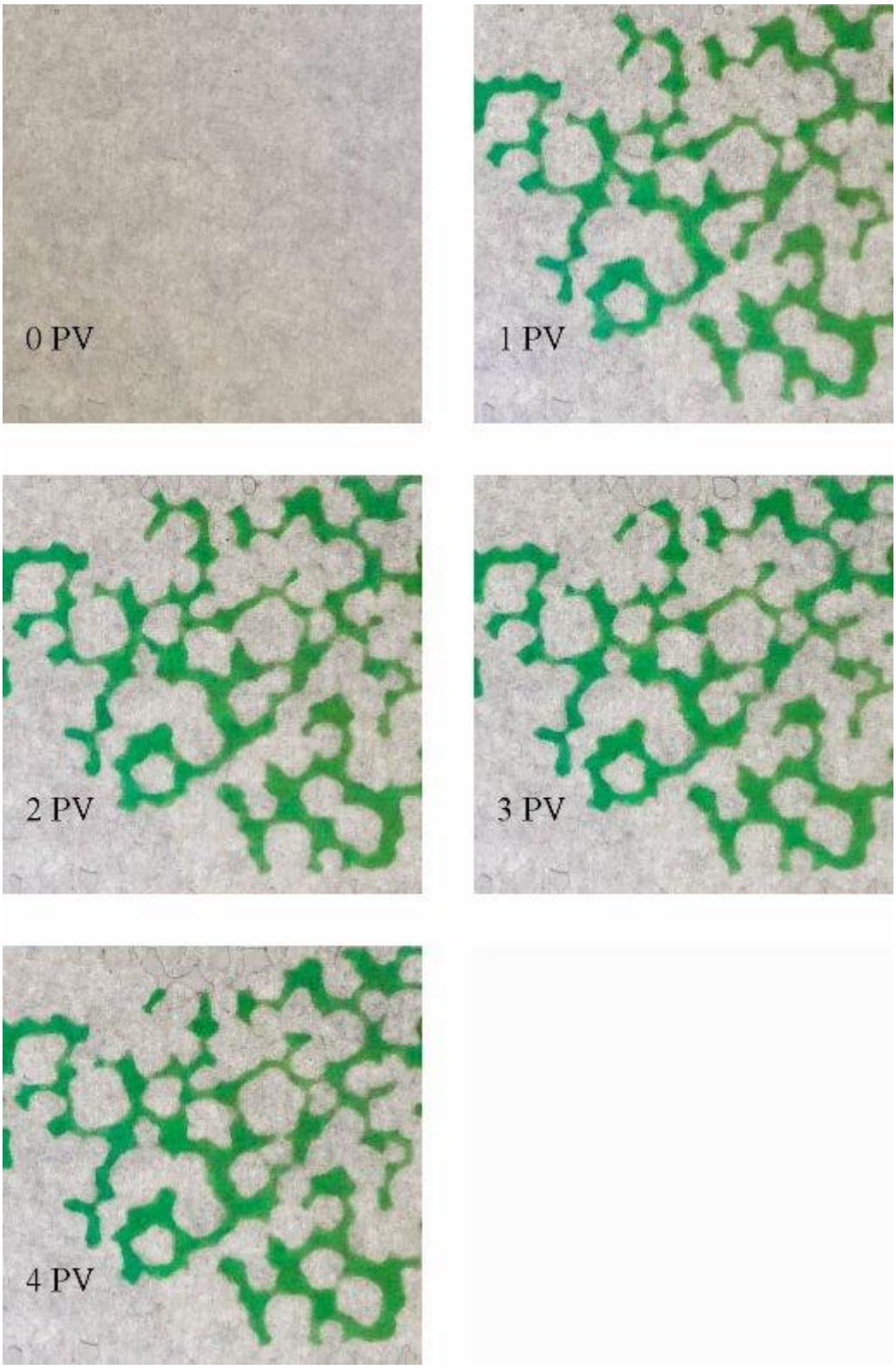

Fig. C.3 – Flow images for 4 PV injection in the secondary recovery experiment.

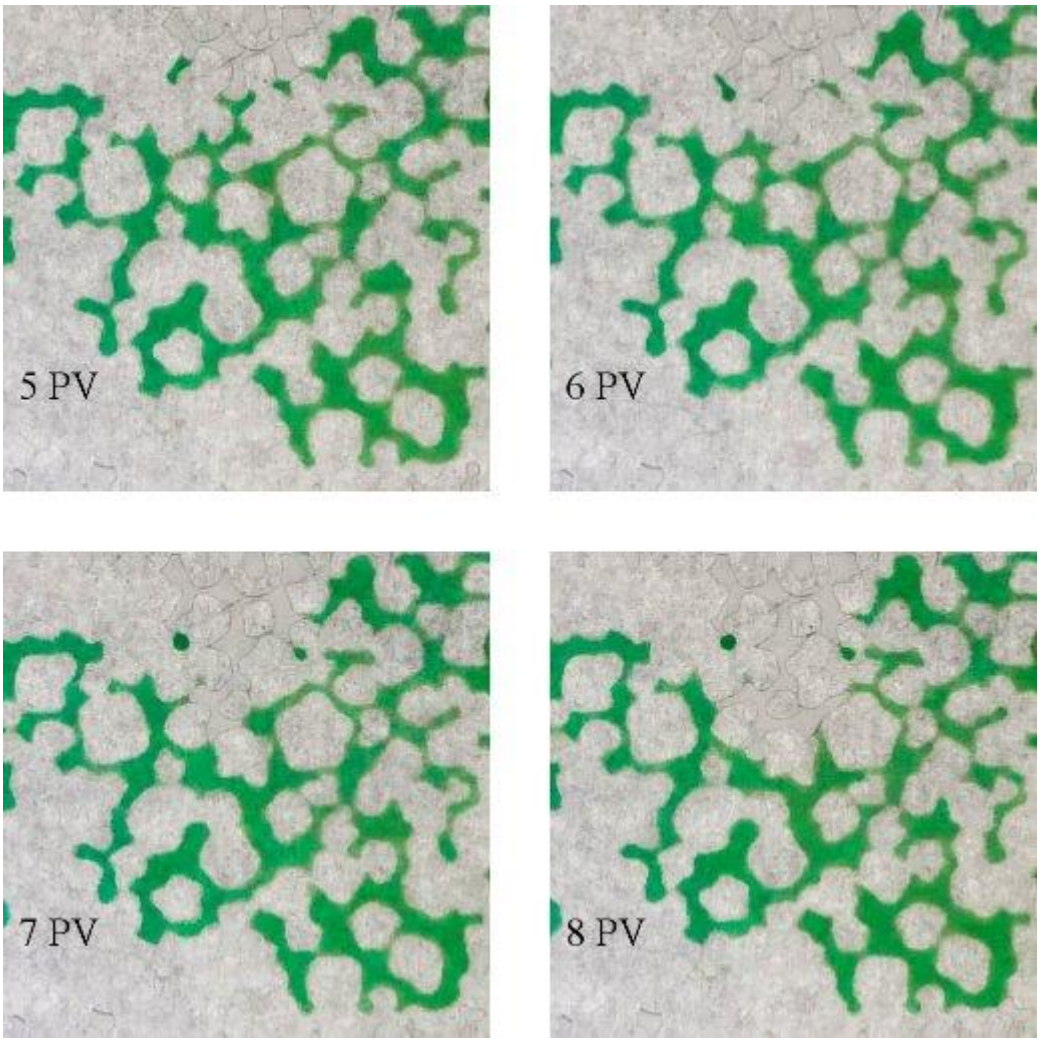

Fig. C.4 – Flow images for 8 PV injection in the secondary recovery experiment.

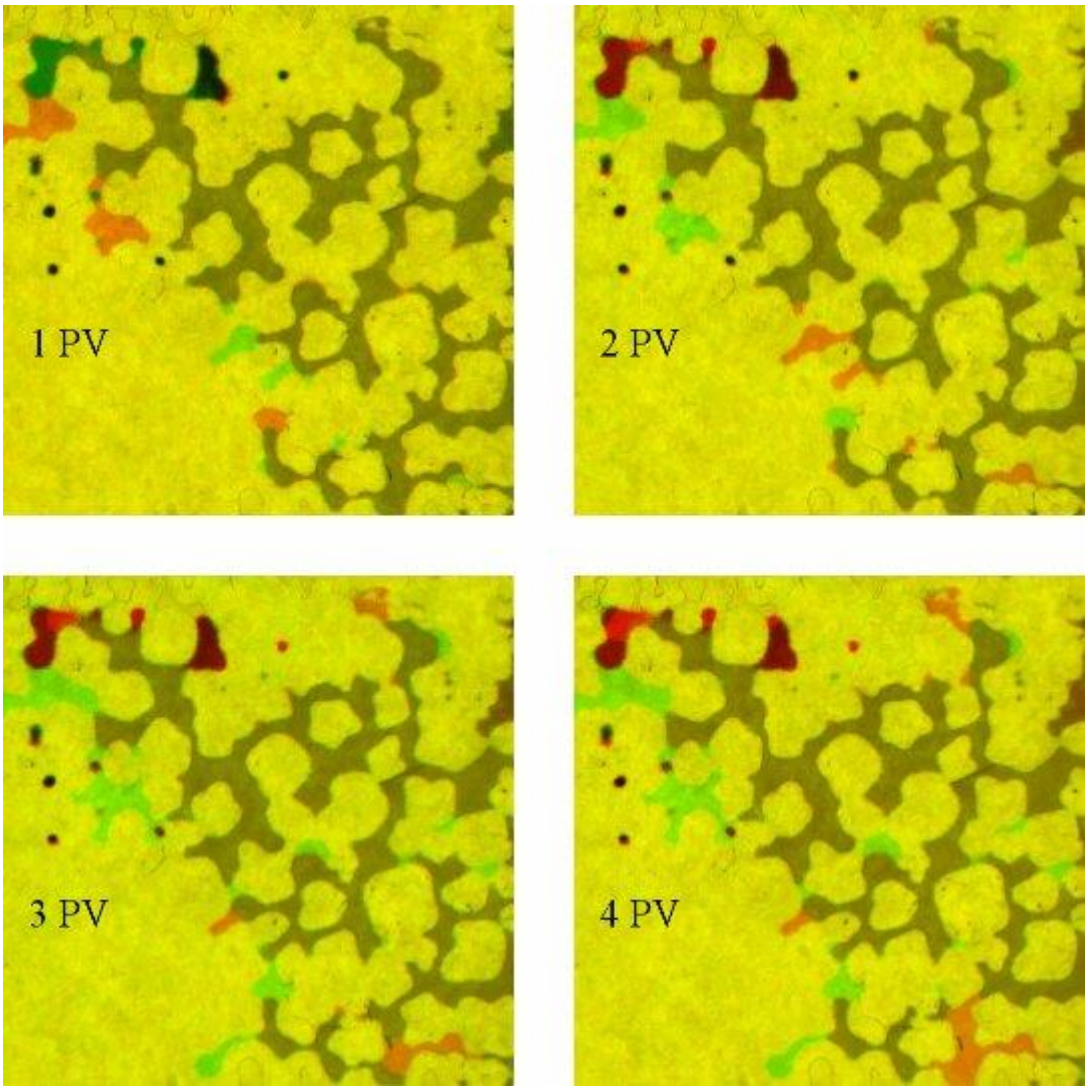

Fig. C.5 – Stacked flow images for brine flooding in the tertiary recovery experiment.

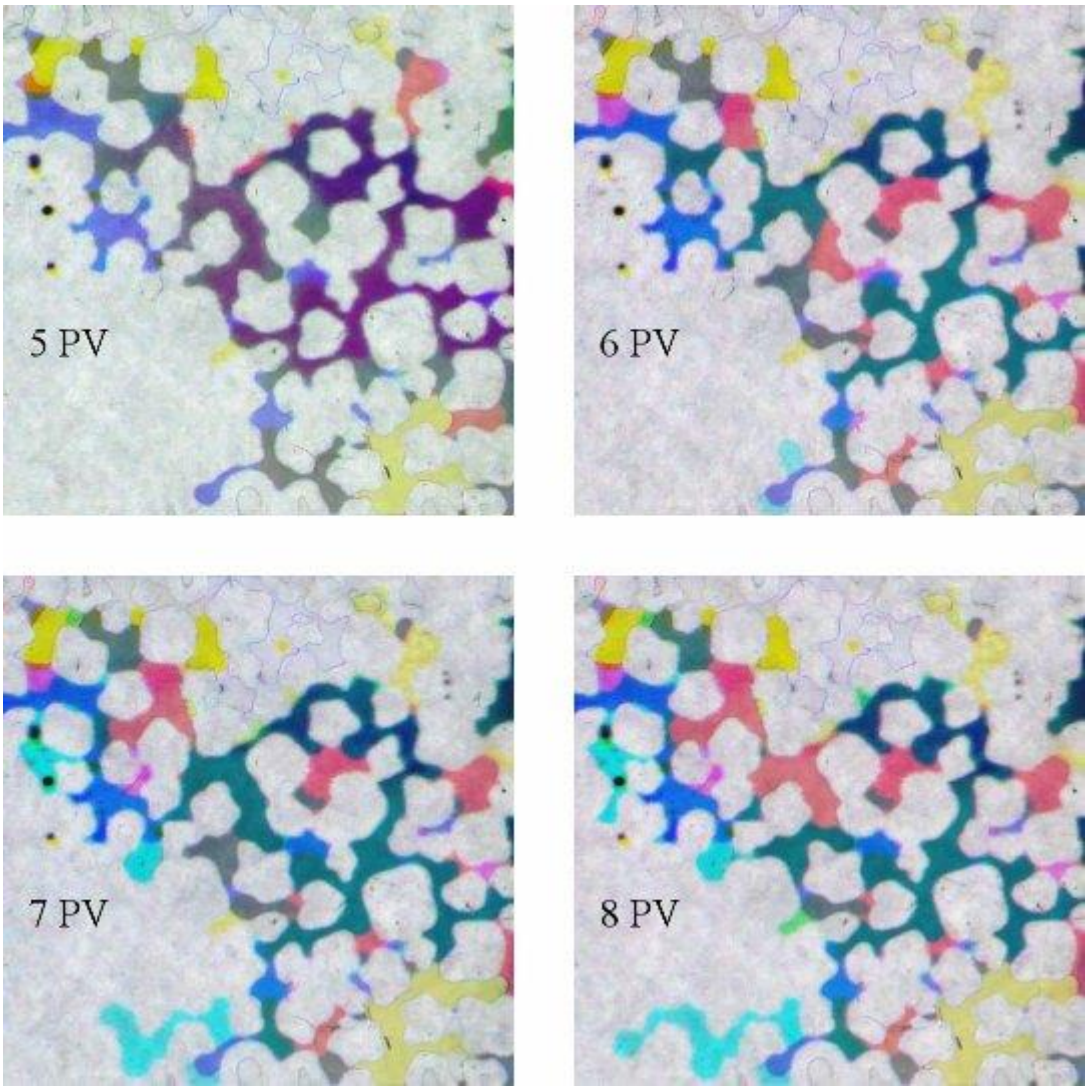

Fig. C.6 – Stacked flow images for nanofluid flooding in the tertiary recovery experiment.

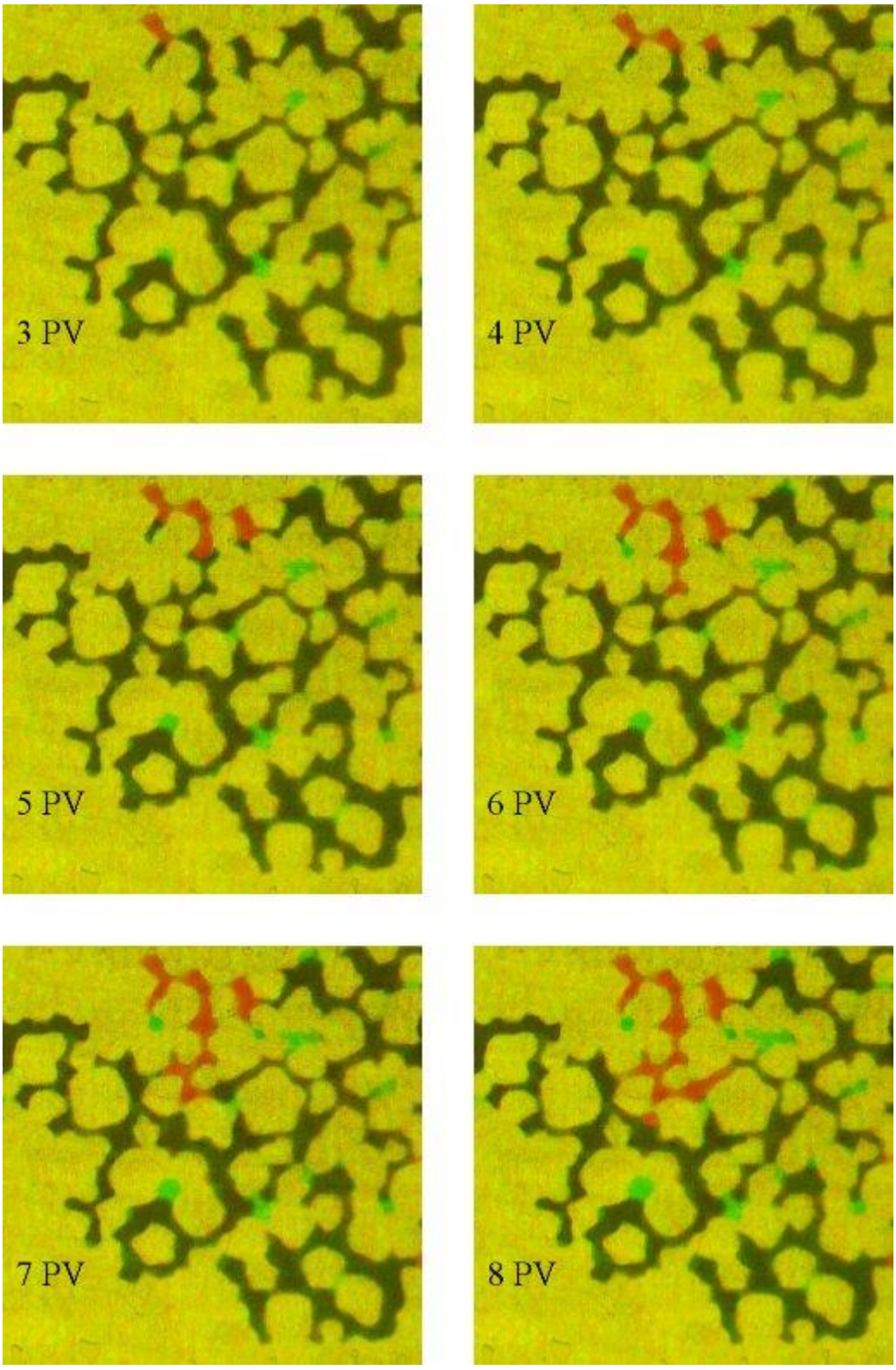

Fig. C.7 – Stacked flow images for 8 PV injection in the secondary recovery experiment.

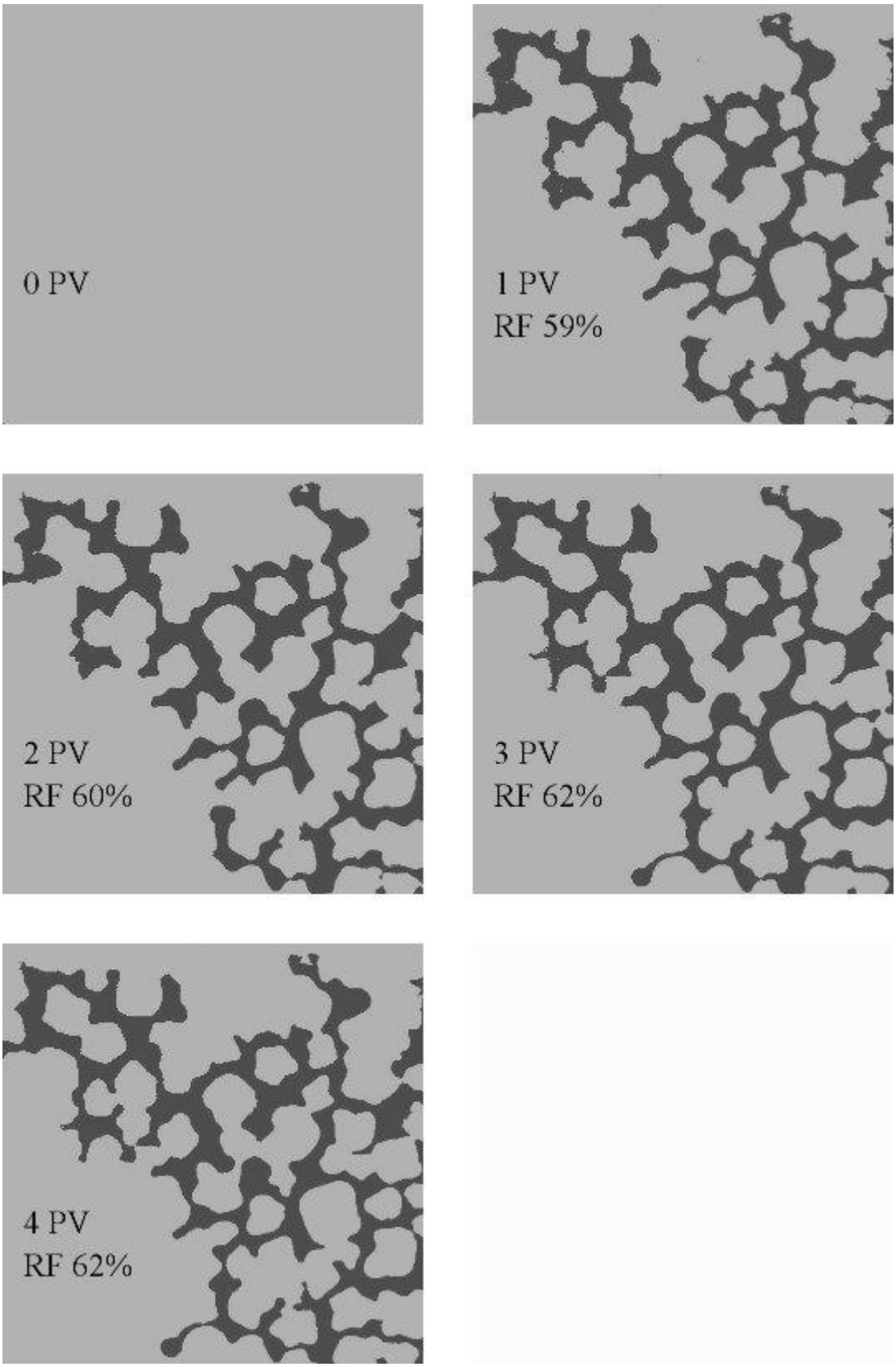

Fig. C.8 – Resulting segmented images for brine flooding in the tertiary recovery experiment and their associated recovery factors (RF).

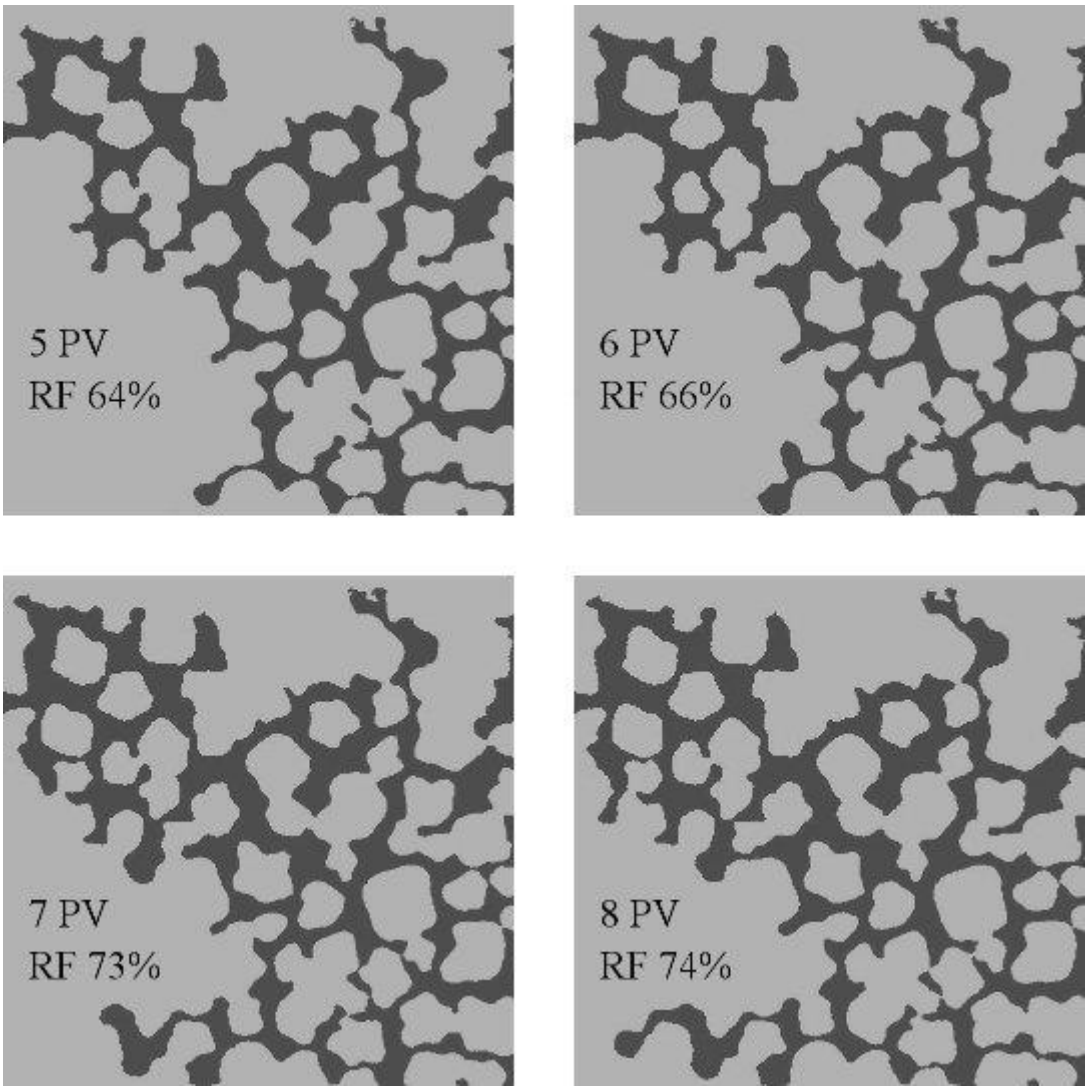

Fig. C.9 – Resulting segmented images for nanofluid flooding in the tertiary recovery experiment and their associated recovery factors (RF).

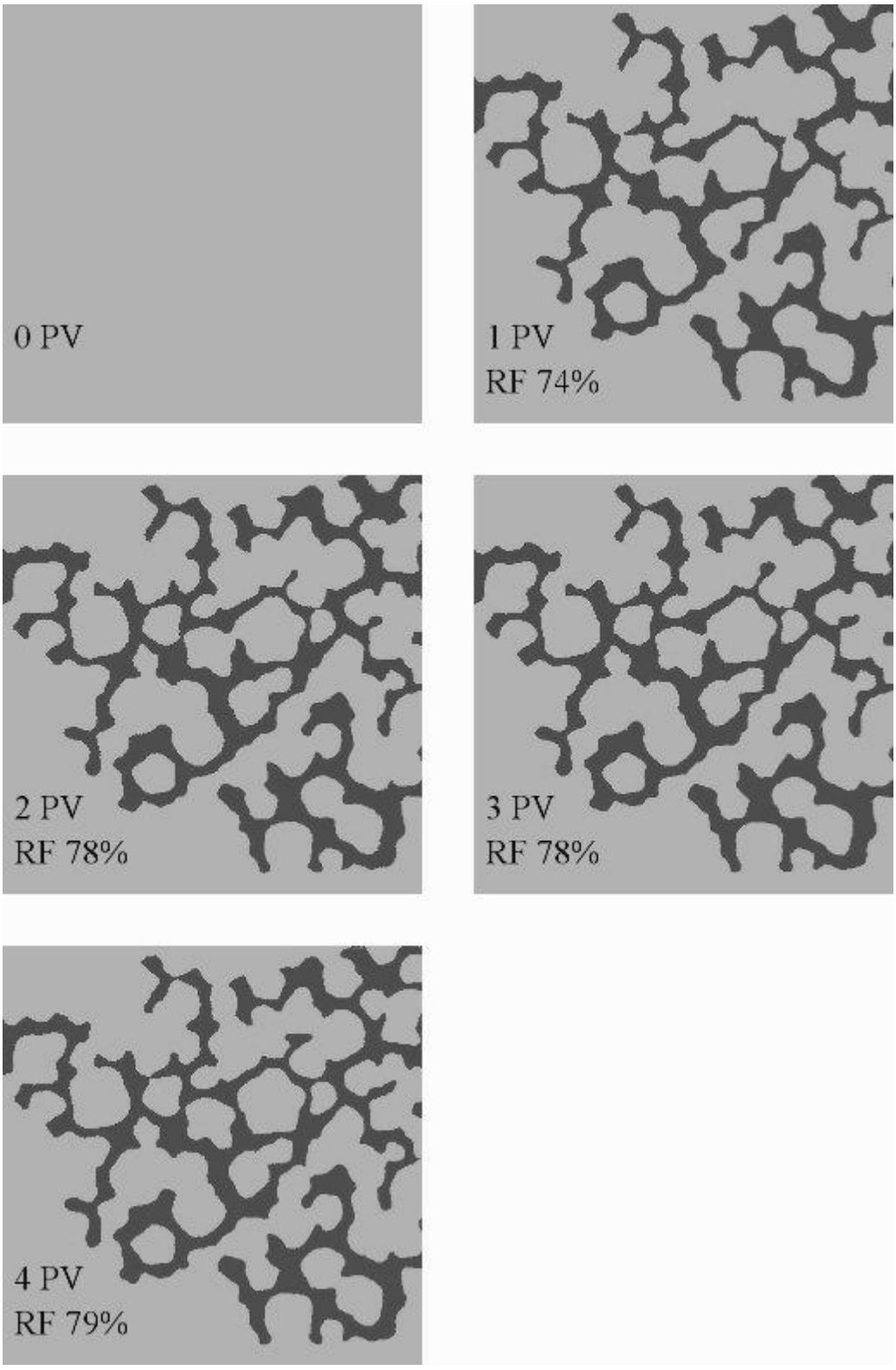

Fig. C.10 – Resulting segmented images for 4 PV injection in the secondary recovery experiment and their associated recovery factors (RF).

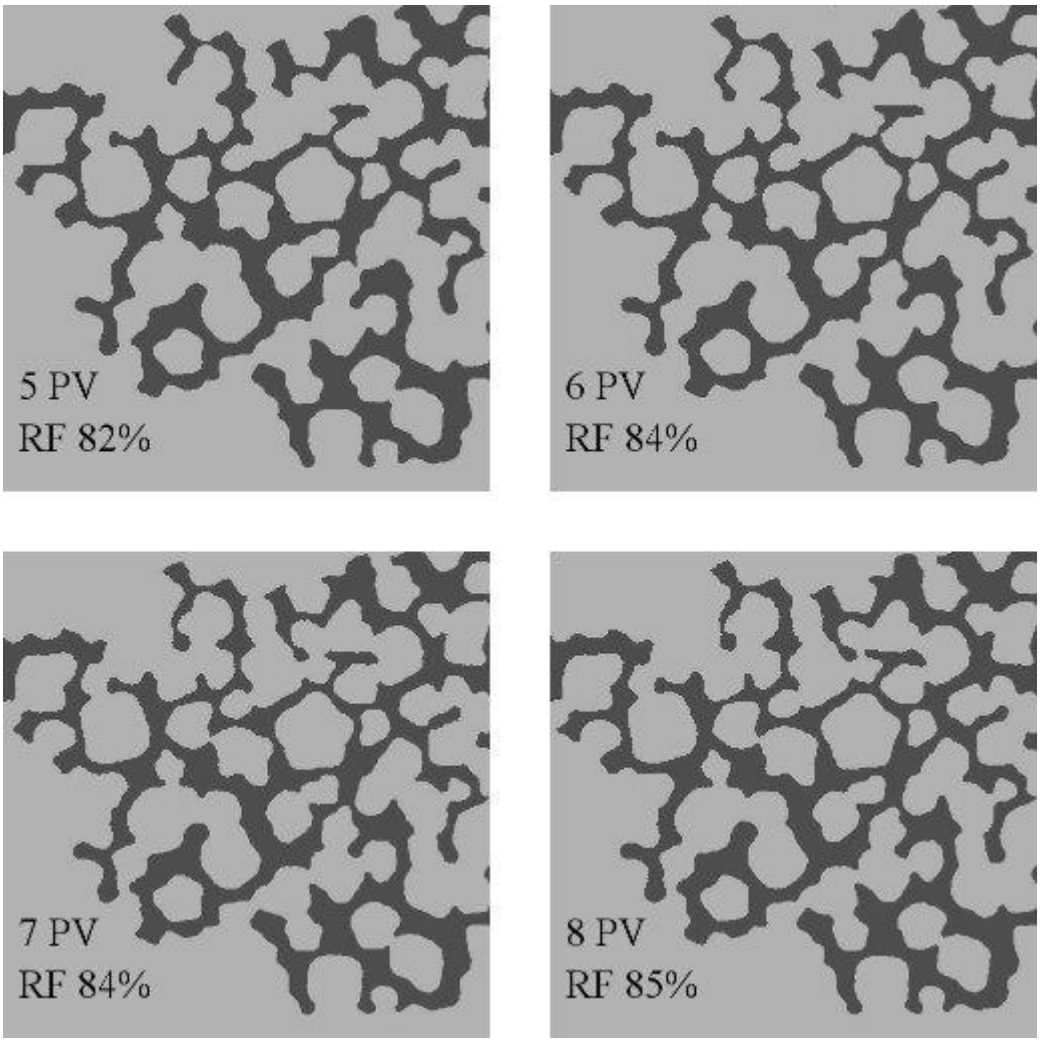

Fig. C.11 – Resulting segmented images for 8 PV injection in the secondary recovery experiment and their associated recovery factors (RF).